UNIVERSITAT POLITÈCNICA DE VALÈNCIA

DOCTORAL PROGRAM
TECHNOLOGIES FOR HEALTH AND WELL-BEING

CONTRIBUTION TO THE IMPROVEMENT OF ELECTRICAL THERAPIES AND TO THE COMPREHENSION OF ELECTROPHYSIOLOGICAL MECHANISMS IN HEART FAILURE AND ACUTE ISCHEMIA USING COMPUTATIONAL SIMULATION

DOCTORAL THESIS

Author:
Edison Fernando Carpio Garay

Supervisors:
Dra. Beatriz Trénor Gomis
Dr. José María Ferrero De Loma-Osorio

Valencia, Spain
December, 2020

Supervisors: Dra. Beatriz Trénor Gomis
Universitat Politècnica de València

Dr. José María Ferrero De Loma-Osorio
Universitat Politècnica de València

External Evaluators: Dr. Jesús Carro Fernández
Universidad San Jorge

Dra. Violeta Monasterio Bazán
Universidad San Jorge

Dr. Carlos Sánchez Tapia
Centro Universitario de la Defensa de Zaragoza

Reading Committee: Dr. Blas Echebarria Domínguez
Universitat Politècnica de Catalunya

Dra. Irene Del Canto Serrano
Universitat Politècnica de València

Dr. Carlos Sánchez Tapia
Centro Universitario de la Defensa de Zaragoza

This doctoral thesis was carried out in the Centro de *Investigación e Innovación en Bioingeniería* (Ci2B) from the Universitat Politècnica de Vàlencia, Valencia, Spain.

Ci2B Centro de Investigación e Innovación en Bioingeniería
Universitat Politècnica de València

Funding information:

During the completion of this doctoral thesis, author Edison Fernando Carpio Garay was financially supported by the *Secretaría de Educación Superior, Ciencia, Tecnología e Innovación (SENESCYT) of the Republic of Ecuador* through the doctoral fellowship number CZ06-000002-2017.

ACKNOWLEDGEMENTS

The culmination of this doctoral thesis has involved extensive and hard work. Thanks to God for being my fundamental support throughout this journey, and thanks to all the people who have contributed, in one way or another, to the development of this work.

I would like to express my sincere and infinite gratitude to my supervisors, Dra. Beatriz Trénor and Dr. José María Ferrero, for their extraordinary dedication, guidance and supervision throughout the course of this thesis. Special thanks to Beatriz for her remarkable agility with my work and for her help in the administrative aspects of my scholarship.

I also want to deeply thank to Dr. Rafael Sebastian, Dr. José Félix Rodríguez, Dr. Juan Francisco Gomez, Dr. Alejandro López and Dra. María Teresa Mora who with their innumerable contributions have greatly supported the advancement of this thesis.

To the University of Cuenca (Ecuador) all my gratitude for the respective permission and support to be able to obtain my PhD and thus continue improving myself in my personal and professional life.

Also, sincere thanks to my friends who gave me their help and messages of encouragement during the difficult moments of this stage as a PhD student.

Finally, the greatest gratitude to my daughters Melissa and Tiffany, my mother Mariana and my siblings Wilson, Diana and Juan for their unconditional love and support. To Carina and Amy for patiently accompanying me in this stage of studies. I couldn't have made it without you.

ABSTRACT

A better understanding of the mechanisms underlying ventricular arrhythmias, as well as an improvement of the associated electrical and pharmacological therapies, are a key factor to prevent sudden cardiac death in patients with structural and electrical heart diseases.

An important cardiomyopathy that can lead to life-threatening ventricular arrhythmias is heart failure (HF). Patients with HF also often suffer from left bundle branch block (LBBB), which worsens their condition. Currently, the most effective treatment to these patients is cardiac resynchronization therapy (CRT). However, many patients are non-responders, so further studies are needed to improve this treatment.

A second cardiac pathology that also produces lethal arrhythmias is myocardial ischemia. Substantial experimental evidence has shown that electrophysiological alterations in the ventricular myocardium constitute a substrate for the generation of arrhythmias during the acute phase of ischemia. These alterations are induced by the three main ischemic components: hyperkalemia, hypoxia and acidosis. However, the influence of each component in the mechanisms of arrhythmia initiation and maintenance is still not completely understood.

In the first section of this doctoral thesis, we focus on the optimization of CRT during its application in a heart suffering from HF and LBBB. For this purpose, we modified the O'Hara action potential (AP) model to simulate a realistic conduction velocity both in healthy and pathological conditions. In addition, a His-Purkinje system (HPS) was generated and incorporated into a 3D human biventricular/torso model to simulate realistic LBBB. A set of computational simulations were performed for different CRT configurations to determine the optimal pacing leads location and delay values leading to the shortest QRS duration. Subsequently, results were compared with other

optimization criteria. The main findings of this study showed the need of better or complementary optimization criteria, such as an index based on the time to reach the 90% of the QRS area suggested in this work, to reach the best ventricular electrical synchrony during the CRT application. In addition, our results also show that the upper septum close to the outflow tract is an alternative site for the right ventricle (RV) stimulation, which avoids the perforation problems of the RV apical wall during the typical CRT procedure. Finally, protocols of left ventricle endocardial pacing should be considered to obtain better CRT results.

In the second section of this thesis, we investigated the effects of the three main components of ischemia on the vulnerability to reentry, as well as the role of the HPS and its mechanisms of action in the generation and maintenance of ventricular arrhythmias. In order to achieve our goal, we first modified the ventricular AP model to realistically simulate the major alterations caused by acute myocardial ischemia. Simulations were performed in a 3D human biventricular model, embedded in a virtual torso, which includes a realistic geometry of the central and border ischemic zones, as well as a detailed HPS. Four scenarios of ischemic severity corresponding to different minutes after coronary artery occlusion were simulated to evaluate the effects of the evolution of ischemia over time. Then, the individual influence of hyperkalemia, hypoxia and acidosis in the width of the vulnerable window (VW) for reentry was assessed during seven scenarios of acute ischemia. Finally, this last set of ischemic simulations was repeated using the anatomical model without the HPS to evaluate the effect of the latter in the VW. Results show that a moderate ischemic condition is the worst scenario for reentry generation. Hypoxia is the ischemic component with the most significant effect on the width of the VW. Furthermore, the retrograde current flow from the myocardium to the HPS in the ischemic region, conduction blocks in discrete sections of the HPS, and the degree of hyperkalemia affecting the Purkinje cells, are suggested as HPS mechanisms that could favor the triggering of ventricular arrhythmias.

RESUMEN

Una mejor comprensión de los mecanismos subyacentes a las arritmias ventriculares, así como una mejora de las terapias eléctricas y farmacológicas asociadas, son un factor clave para prevenir la muerte súbita cardíaca en pacientes con cardiopatías estructurales y eléctricas.

Una miocardiopatía importante que puede provocar arritmias ventriculares potencialmente mortales es la insuficiencia cardíaca (HF). Los pacientes con HF a menudo sufren también de bloqueo de rama izquierda (LBBB) que deteriora su condición. Actualmente, el tratamiento más eficaz para estos pacientes es la terapia de resincronización cardíaca (CRT). Sin embargo, no se alcanza una respuesta positiva en todos los casos, por lo que es necesario un mayor estudio para mejorar este tratamiento.

Una segunda patología cardíaca que también produce arritmias letales es la isquemia miocárdica. Evidencia experimental ha demostrado que las alteraciones electrofisiológicas en el miocardio ventricular constituyen un sustrato para la generación de arritmias durante la fase aguda de isquemia. Estas alteraciones son inducidas por los tres componentes isquémicos principales: hiperkalemia, hipoxia y acidosis. Sin embargo, la influencia de cada componente en los mecanismos de inicio y mantenimiento de las arritmias no se comprende aún con claridad.

Una primera parte de esta tesis doctoral, se centra en la optimización de la CRT durante su aplicación en un corazón que padece HF y LBBB. Para esto, se modificó el modelo de potencial de acción (AP) de O'Hara para simular una velocidad de conducción realista tanto en condiciones sanas como patológicas. Además, se estimó e incorporó un sistema de His-Purkinje (HPS) dentro de un modelo biventricular/torso humano 3D para simular un LBBB realista. A continuación, se desarrolló un

conjunto de simulaciones computacionales para diferentes configuraciones de la CRT a fin de determinar la posición y el instante de estimulación óptimo que conducen a la duración más corta del QRS. Posteriormente, los resultados se compararon con otros criterios de optimización. Los principales hallazgos de este estudio mostraron la necesidad de definir criterios de optimización mejores o complementarios, como un índice basado en el tiempo hasta alcanzar el 90% del área del QRS sugerido en este trabajo, para alcanzar la mejor sincronía eléctrica ventricular durante la aplicación de la CRT. Además, nuestros resultados también muestran que el septo superior cercano al tracto de salida es un sitio alternativo para la estimulación del ventrículo derecho, lo cual evita los problemas de perforación de la pared apical durante el procedimiento típico de la CRT. Por último, para obtener mejores resultados de la CRT se deben considerar protocolos de estimulación endocárdica en el ventrículo izquierdo.

En la segunda parte de esta tesis se investigó los efectos de los tres componentes principales de la isquemia sobre la vulnerabilidad a una reentrada, así como el papel del HPS y sus mecanismos de acción en la generación y mantenimiento de arritmias ventriculares. Para lograr este objetivo, en primer lugar, se modificó el modelo AP ventricular para simular de forma realista las principales alteraciones provocadas por la isquemia miocárdica aguda. Las simulaciones se realizaron en un modelo biventricular humano 3D, acoplado en un torso virtual, que incluye una geometría realista de las zonas isquémicas central y de borde, así como un HPS detallado. Se simularon cuatro escenarios de severidad isquémica correspondientes a diferentes minutos de oclusión de la arteria coronaria para evaluar los efectos de la evolución de la isquemia en el tiempo. Luego, se evaluó la influencia individual de la hiperkalemia, hipoxia y acidosis en el ancho de la ventana vulnerable (VW) a reentradas durante siete escenarios de isquemia aguda. Finalmente, se repitió este último conjunto de simulaciones isquémicas utilizando el modelo anatómico sin el HPS para evaluar el efecto de este último en la VW. Los resultados muestran que una condición isquémica moderada es el peor escenario para la generación de una reentrada. La

hipoxia es el componente isquémico con el efecto más significativo en el ancho de la VW. Además, el flujo de corriente retrógrado desde el miocardio hacia el HPS en la región isquémica, los bloqueos de conducción en secciones discretas del HPS y el grado de hiperkalemia que afecta a las células de Purkinje, son sugeridos como mecanismos que podrían favorecer la aparición de arritmias ventriculares.

RESUM

Una millor comprensió dels mecanismes subjacents a les arrítmies ventriculars, així com una millora de les teràpies elèctriques i farmacològiques associades, són un factor clau per a previndre la mort sobtada cardíaca en pacients amb cardiopaties estructurals i elèctriques.

Una miocardiopatia important que pot provocar arrítmies ventriculars potencialment mortals és la insuficiència cardíaca (HF). Els pacients amb HF sovint pateixen també de bloqueig de branca esquerra (LBBB) que deteriora la seua condició. Actualment, el tractament més eficaç per a aquests pacients és la teràpia de resincronització cardíaca (CRT). No obstant això, no s'aconsegueix una resposta positiva en tots els casos, per la qual cosa és necessari un major estudi per a millorar aquest tractament.

Una segona patologia cardíaca que també produeix arrítmies letals és la isquèmia miocàrdica. Evidència experimental ha demostrat que les alteracions electrofisiològiques en el miocardi ventricular constitueixen un substrat per a la generació d'arrítmies durant la fase aguda d'isquèmia. Aquestes alteracions són induïdes pels tres components isquèmics principals: hiperkalèmia, hipòxia i acidosi. No obstant això, la influència de cada component en els mecanismes d'inici i manteniment de les arrítmies no es comprén encara amb claredat.

Una primera part d'aquesta tesi doctoral, se centra en l'optimització de la CRT durant la seua aplicació en un cor que pateix HF i LBBB. Per a això, es va modificar el model de potencial d'acció (AP) de O'Hara per a simular una velocitat de conducció realista tant en condicions sanes com patològiques. A més, es va estimar i es va incorporar un sistema de His-Purkinje (HPS) dins d'un model biventricular/tors humà 3D per a simular un LBBB realista. A continuació, es va desenvolupar un conjunt de simulacions computacionals per a diferents

configuracions de la CRT a fi de determinar la posició i l'instant d'estimulació òptim que condueixen a la duració més curta del QRS. Posteriorment, els resultats es van comparar amb altres criteris d'optimització. Les principals troballes d'aquest estudi van mostrar la necessitat de definir millors o complementaris criteris d'optimització, com un índex basat en el temps fins a aconseguir el 90% de l'àrea del QRS suggerida en aquest treball, per a aconseguir la millor sincronia elèctrica ventricular durant l'aplicació de la CRT. A més, els nostres resultats també mostren que el septe superior pròxim al tracte d'eixida és un lloc alternatiu per a l'estimulació del ventricle dret, la cual cosa evita els problemes de perforació de la paret apical durant el procediment típic de la CRT. Finalment, per a obtindre millors resultats de la CRT s'han de considerar protocols d'estimulació endocárdica en el ventricle esquerre.

En la segona part d'aquesta tesi es va investigar els efectes dels tres components principals de la isquèmia sobre la vulnerabilitat a una reentrada, així com el paper del HPS i els seus mecanismes d'acció en la generació i manteniment d'arrítmies ventriculars. Per a aconseguir aquest objectiu, en primer lloc es va modificar el model AP ventricular per a simular de manera realista les principals alteracions provocades per la isquèmia miocàrdica aguda. Les simulacions es van realitzar en un model biventricular humà 3D, acoblat en un tors virtual, que inclou una geometria realista de les zones isquèmiques central i de vora, així com un HPS detallat. Es van simular quatre escenaris de severitat isquèmica corresponents a diferents minuts d'oclusió de l'artèria coronària per a avaluar els efectes de l'evolució de la isquèmia en el temps. Després, es va avaluar la influència individual de la hiperkalèmia, hipòxia i acidosi en l'ample de la finestra vulnerable (VW) a reentradas durant set escenaris d'isquèmia aguda. Finalment, es va repetir aquest últim conjunt de simulacions isquèmiques utilitzant el model anatòmic sense el HPS per a avaluar l'efecte d'aquest últim en la VW. Els resultats mostren que una condició isquèmica moderada és el pitjor escenari per a la generació d'una reentrada. La hipòxia és el component isquèmic amb l'efecte més significatiu en l'ample de la VW.

A més, el flux de corrent retrògrad des del miocardi cap al HPS a la regió isquèmica, els bloquejos de conducció en seccions discretes del HPS i el grau d'hiperkalèmia que afecta les cèl·lules de Purkinje, són suggerits com a mecanismes que podrien afavorir l'aparició d'arrítmies ventriculars.

CONTENTS

LIST OF FIGURES

LIST OF TABLES

ACRONYMS

3D	Three-dimensional
$[ADP]_i$	Intracellular concentration of Adenosine Di-Phosphate
AHA	American Heart Association
AP	Action potential
APD	Action potential duration
$[ATP]_i$	Intracellular concentration of Adenosine Tri-Phosphate
AVD	Atrioventricular delay
AVN	Atrioventricular node
BCL	Basic cycle length
BiV	Biventricular
BSPM	Body surface potential maps
BZ	Border zone
CCS	Cardiac conduction system
CI	Coupling interval
CRT	Cardiac resynchronization therapy
CV	Conduction velocity
Cx43	Connexin 43
DAD	Delayed after depolarization
EAD	Early after depolarization
ECG	Electrocardiogram
ERP	Effective refractory period
HF	Heart failure
HPS	His-Purkinje system
ICZ	Ischemic central zone
LA	Left atrium
LAD	Left anterior descending artery
LBBB	Left bundle branch block
LPC	Lysophosphatidylcholine
LV	Left ventricle
LVEF	Left ventricle ejection fraction
NZ	Normal zone

pH_i	Intracellular pH
pH_o	Extracellular pH
PMJ	Purkinje-Myocardial junction
PRR	Post-repolarization refractoriness
PS	Purkinje system
QRSa	QRS area
QRSd	QRS duration
RA	Right atrium
RBBB	Right bundle branch block
RCA	Right coronary artery
RMP	Resting membrane potential
RV	Right ventricle
SAN	Sinoatrial node
t_{90}	Time to 90% of the ventricular activation
t_{90}QRSa	Time to reach the 90% of the QRS area
TAT	Total activation time
VF	Ventricular fibrillation
V_m	Membrane potential
VT	Ventricular tachycardia
VVD	Interventricular delay
VW	Vulnerable window
φ_e	Extracellular potential
σ_L	Longitudinal conductivity
σ_T	Transversal conductivity

CHAPTER 1

Introduction

1.1 Motivation

Cardiovascular diseases are the first cause of mortality in Europe and worldwide, with around 3.9 million [1] and 17.9 million [2] of all deaths each year, respectively. One of the major causes of these deaths is the development of complex ventricular arrhythmias, which often lead to cardiac arrest. Ventricular fibrillation (VF) is the most common lethal arrhythmia observed in clinical practice, with an incidence at the time of cardiac arrest of 60 – 70% [3], [4]. VF consists on a chaotic disorganized electrical activation of the ventricles that, without immediate treatment, leads to death within minutes.

Among the most common causes for the generation of VF and ventricular tachycardia (VT) are structural and electrical heart diseases, such as heart failure (HF) and acute myocardial ischemia [5], [6]. HF represents a chronic and progressive condition in which the heart muscle suffers anatomical and functional remodeling that alters the electrophysiological properties of the myocardium. The prolongation of the action potential duration (APD), alterations in calcium handling, and a reduction in the protein responsible for the coupling between cardiac cells called connexin 43 (Cx43), are the main hallmark characteristics of HF [7], [8]. As a consequence of these changes,

disorders in the action potential (AP) propagation may occur, which prevent the heart for pumping blood normally, reducing the ejection fraction (percentage of blood expelled during a heartbeat) of the left ventricle (LV) [9]. In addition, arrhythmias might be initiated in the ventricular tissue by triggering mechanisms such as early after depolarizations (EADs) and delayed after depolarizations (DADs) [7]. In Europe, over 15 million people are affected by HF [10] and approximately one third of them additionally suffer from left bundle branch block (LBBB) which worsens their conditions [11].

HF patients who suffer LBBB present a delay in the LV activation that leads to an interventricular dyssynchrony [12]. Similarly, an early activation of the interventricular septum with respect to the LV free wall produces a LV intraventricular dyssynchrony [13]. The combined effect of these two electrical disorders causes an uncoordinated contraction of the ventricles, reducing the efficiency of the heart to pump blood. In HF patients, this issue can make things worse. Indeed, in several studies, LBBB has been associated with increased 1-year mortality rate [14], [15]. In order to improve the quality of life of patients with HF, therapies with drugs and electrical stimulation are used. However, many patients are non-responders to these.

Currently, cardiac resynchronization therapy (CRT) is the most effective treatment to restore the electrical activity of the heart in patients with HF and HF+LBBB [16], [17]. Typical CRT consist of a synchronized stimulation in the apex of the right ventricle (RV) and the lateral wall of the left ventricle (LV). CRT inclusion criteria are strictly established based on several dyssynchrony markers, such as the morphology of the QRS complex and LV ejection fraction [18]. Despite this, only two-third of CRT patients positively respond to treatment [19], [20] and in some cases, implantation issues, such as perforation of the RV apex, have been observed [21]–[23]. For these reason, it is of vital importance to improve CRT planning in terms of the sites and instants of stimulation, or even to define new biomarkers as a complement to the current optimization methods.

Another pathology which sometimes leads to HF in the long term, and also produces malignant ventricular arrhythmias is myocardial ischemia. In its acute phase, i.e. in the first 0 – 30 minutes after coronary artery occlusion [24], ischemic cells suffer a series of electrophysiological changes caused mainly by three ischemic components: hypoxia (reduction of oxygen supply), acidosis (reduction of pH) and hyperkalemia (increment of extracellular potassium) [25], [26]. These changes increase the heterogeneity of repolarization and refractoriness between normal and ischemic tissue, predisposing the myocardium to the generation of life-threatening arrhythmias, such as VT and VF [27]. Acute ischemia is an extremely complex process and the relative contribution of each ischemic component to arrhythmogenesis is still not completely established, furthermore its study by purely experimental means is difficult (or impossible) to carry out, especially in humans. This situation, together with the controversial role of the His-Purkinje system (HPS) in the onset and maintenance of ventricular arrhythmias [28]–[30], increases the need for further investigation and the use of novel tools, such as mathematical models and computational simulations that allow the understanding of the complex mechanisms of ischemia-induced arrhythmias.

Mathematical models which allow the simulation of the electrical activity of the heart, as well as its pathologies and associated therapies, have proved to be a powerful and complementary tool to animal and clinical experimentation. Based on data from human and different animal species, these models allow the simulation of the APs of cardiac cells, ionic currents, concentration dynamics, and the AP propagation through the cardiac tissue, realistically reproducing the heart electrical activity [31]. Previous studies using mathematical models have improved our understanding of the mechanisms underlying ventricular arrhythmias [32]–[35]. Nowadays, there are models that describe the electrical processes at the cellular level with a great degree of electrophysiological detail, such as the ten Tusscher et al. [36], O'Hara et al. [37] and Tomek et al. [38] models. The O'Hara et al. [37] model

was the most recent human AP model when this doctoral thesis began, and therefore one of the most comprehensive tools for the study of cardiac pathologies and their therapies in a non-invasive way.

1.2 Objectives

The main objective of the present doctoral thesis is to study the mechanisms underlying ventricular arrhythmias and their response to electrical therapies in a three-dimensional realistic anatomical model of the human ventricles under (a) HF with LBBB, and (b) acute myocardial ischemia conditions using computer simulations. This major goal was divided into the following specific objectives:

- To improve the most recent human ventricular AP models to more realistically simulate the electrical behavior of the heart suffering from HF with LBBB and acute myocardial ischemia based on extensive literature review.

- To improve the 3D anatomical models of the human ventricles by incorporating a His-Purkinje system that allows obtaining a realistic ECG morphology in the precordial leads in healthy and pathological conditions.

- To analyze the optimal pacing leads location and atrioventricular delay (AVD) and interventricular delay (VVD) during CRT procedure in a tissue with HF and LBBB, based on the shortest QRS duration criterion. Subsequently, the results are to be compared with other optimization criteria.

- To investigate the effects of hyperkalemia, hypoxia and acidosis, as well as the role of the His-Purkinje system, in the vulnerability to reentry during different ischemic severity scenarios.

1.3 Structure of the thesis

This doctoral thesis is divided into six chapters, which are described below:

Chapter 1 describes the main reasons that motivate the conception, design and development of this research study, as well as the objectives and the structure of the present doctoral thesis.

Chapter 2 presents a brief description of the fundamental concepts about the heart, the cardiac pathologies of HF, LBBB and acute myocardial ischemia, and the treatment with CRT. These concepts are the base of the development and understanding of the present work.

Chapter 3 focuses on improving CRT by optimizing pacing leads location, AVD and VVD delays. For this purpose, a non-invasive criterion based on the shortest QRS duration is used. Subsequently, the results are compared with other optimization methods to determine the efficacy of each method, as well as to define possible new biomarkers that can be used as a complementary tool for CRT optimization.

Chapter 4 aims at investigating the effect of each main component of acute ischemia (hyperkalemia, hypoxia and acidosis) on the vulnerable window to reentry during different scenarios of ischemic severity. Furthermore, the role of the His-Purkinje system in the generation and maintenance of reentry is analyzed.

Chapter 5 presents a concise general discussion between the main findings obtained in this work and the related literature.

Chapter 6 summarizes the major conclusions derived from the present doctoral thesis, linking these with the initial objectives raised. Finally, some guidelines for future works are provided.

CHAPTER 2

State of the art

2.1 Cardiac anatomy

2.1.1 Structure of the heart

The heart is the muscular organ responsible for pumping blood into the cardiovascular system, supplying oxygen and substrates to the whole organism. It is located in the middle of the chest, between the lungs, and behind the breastbone. Its inferior wall leans on the diaphragm and it is covered by a membrane called pericardium.

The heart consists of four cavities, two upper called atria separated by the interatrial septum, and two lower called ventricles separated by the interventricular septum (Figure 2.1). The atria are connected to the ventricles by the atrioventricular valves. The tricuspid valve is located between right atrium (RA) and right ventricle (RV), while the mitral valve is located between the left atrium (LA) and the left ventricle (LV). These valves regulate the blood flow from the atria to the ventricles. On the other hand, the ventricles are connected to the aorta (left) and to the pulmonary (right) arteries by the aorta and pulmonary valves, respectively. Both valves allow blood flow in a single direction (out of the heart).

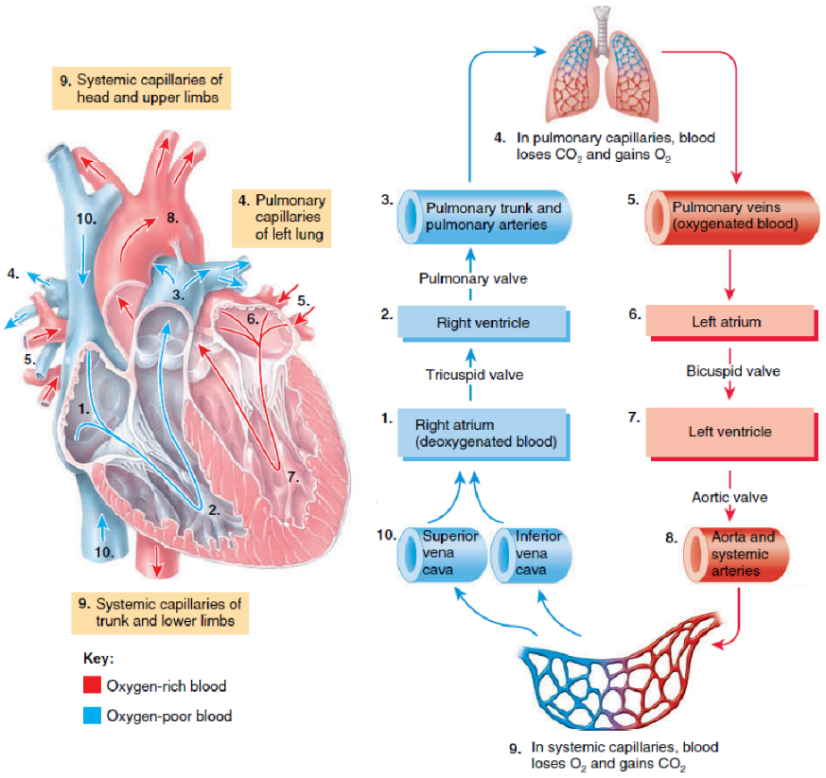

Figure 2.1 Anatomical structure of the heart (left panel), and blood flow through the heart and the circulatory system (right panel). The blue arrows indicate the direction of oxygen-poor blood flow coming from the different organs to lungs. The red arrows show the direction of oxygen-rich blood flow coming from the lungs to be distributed to the rest of the body [39].

The wall of the heart or myocardium is composed by three different layers of cardiac cells (cardiomyocytes or myocytes). The epicardium is the external layer, the midmyocardium is the middle layer and the endocardium is the internal layer. In the endocardial layer of the ventricles there are small papillary muscles connecting the ventricular wall with the tricuspid and mitral valves through the chordae tendineae. These papillary muscles serve to prevent retrograde blood flow from the ventricles to the atria (Figure 2.2). Furthermore, there is a second type of muscle structures called endocardial trabeculations or trabeculae carneae, which are projected from the inner surface of the ventricles forming a network that crosses the heart chamber.

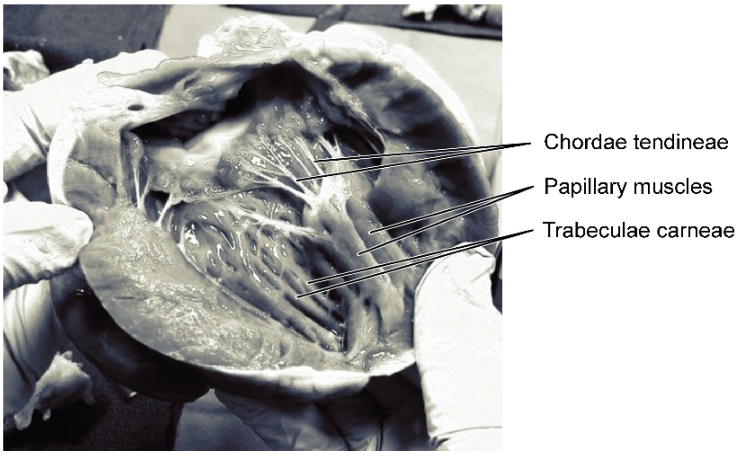

Figure 2.2 Longitudinal cross-section of the heart showing the chordae tendineae and papillary muscles [40]**.**

2.1.2 Cardiac conduction system

A synchronized contraction of the cardiac muscle allows the heart to pump the necessary blood into the circulatory system. This contraction is the response to an electrical impulse generated and propagated through a set of specific myocytes which constitute the cardiac conduction system (CCS).

Under physiological conditions, the primary pacemaker of the heart is the sinus node or sinoatrial node (SAN). This node consists of cardiac cells capable of generating rhythmic electrical impulses autonomously. The SAN is located in the RA wall close to the upper cave vein [41] and determines the normal heart rate (sinus rhythm) [42]. The rest of structures composing the CCS are the atrioventricular node (AVN), the bundle of His, the left and right bundle branches and the Purkinje network [43], [44] (Figure 2.3). These structures transmit the electrical impulses generated in the SAN to the ventricular tissue in a synchronized way.

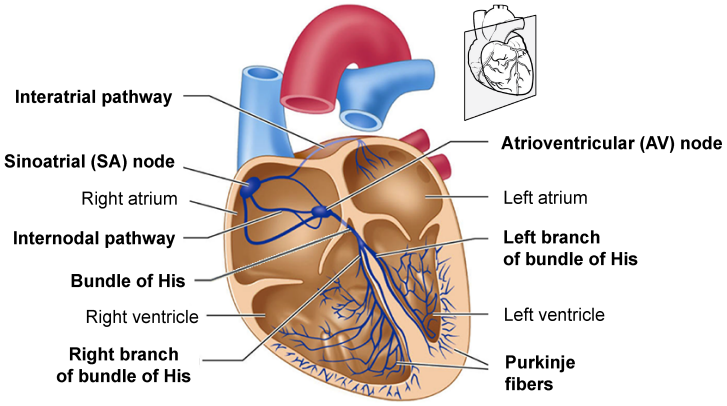

Figure 2.3 Coronal cross-section of the heart exhibiting the cardiac conduction system. Modified from [45].

When a stimulus is generated by the SAN, it propagates through the internodal pathways to the AVN, or also known as the secondary pacemaker of the heart. Due to the fact that the atria and ventricles are electrically insulated, the AVN serves as an electrical interconnection point between the two cardiac chambers. In addition, in the AVN conduction velocity (CV) is reduced to ensure that the atria contract before the ventricles, so that the blood flow is optimal in the ventricular direction. Afterwards, the electrical stimulus is propagated through the bundle of His, which is split into the left and right branches located in the interventricular septum. Finally, the cardiac impulse reaches the Purkinje network which transmits it to the endocardium through the Purkinje-myocardial junctions (PMJs). As the His-Purkinje system (HPS) is electrically isolated, except in the PMJs, the simultaneous stimulation of several cardiomyocytes through PMJs allows the generation of different wavefronts spreading throughout the ventricular myocardium. Under physiological conditions, these wavefronts allow a synchronized electrical activation of the ventricles, which in turn leads to a coordinated ventricular contraction and an efficient blood pumping by the heart.

The HPS is composed of a specific type of cardiomyocytes called Purkinje cells. Such cardiomyocytes allow a fast electrical conduction

of the electrical impulse. CV through HPS varies in the interval of 2 to 3 m/s [46], [47]. This CV is significantly faster than the CV in the ventricular muscle which ranges between 0.5 and 0.7m/s [48].

2.2 Cardiac electrophysiology

2.2.1 The action potential

Cardiomyocytes, like other excitable cells, have a potential difference between the intracellular and the extracellular media (membrane potential) which can be measured by inserting a microelectrode through the cell membrane. Under resting conditions, this difference is called resting membrane potential (RMP) and its value is comprised between –80mV and –90mV for a healthy ventricular cell [49]. When a cardiomyocyte is paced with an electrical impulse, the membrane potential (V_m) changes over time. This variation is known as action potential (AP) and it is characterized by a rapid rise (depolarization) followed by a subsequent return to the RMP (repolarization). However, the features of the AP vary according to the kind of cardiac cell, differing mainly in the morphology and duration (APD) of the AP (Figure 2.4). These variations are the result of the distinct ion channels present in each cell, so that different areas can be defined in the cardiac tissue.

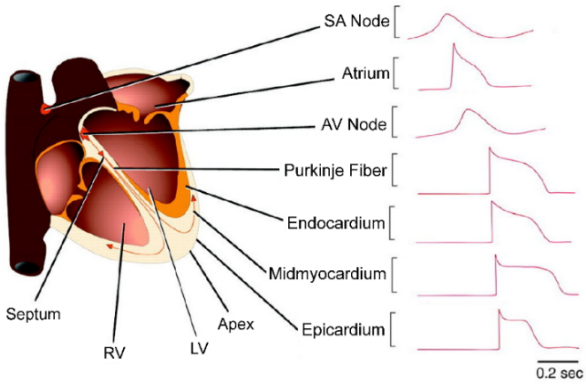

Figure 2.4 Action potential waveforms recorded in different regions of the heart. Modified from [50].

An AP is generated due to the exchange of ions, mainly sodium (Na^+), potassium (K^+), calcium (Ca^{2+}) and chlorine (Cl^-) between the intracellular and the extracellular media. This exchange is done through the cell membrane which has three structures allowing the active and passive movement of ions between the two media: ion channels, pumps and exchangers (Figure 2.5). This ion movement is the result of two causes. First, the variation between the ion concentrations inside and outside the cell produces a diffusion gradient and second, the electric field generated by the positively and negatively charged ions of each medium which produces an electrical force that allows the movement of ions through the membrane.

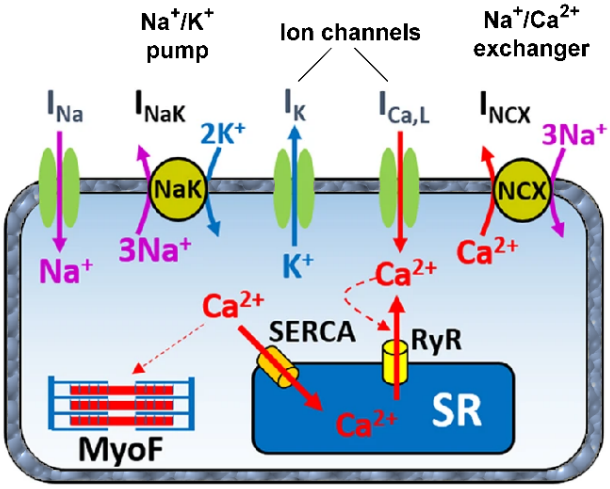

Figure 2.5 Schematic diagram of a myocyte showing the main membrane structures (ion channels, pumps and exchangers) used for ion exchange [51].

The morphology of an AP is characterized by five different phases: phases 0, 1, 2, 3 and 4. Figure 2.6 shows the AP phases of a ventricular cardiomyocyte, which are detailed below, as well as the ion current responsible for each phase.

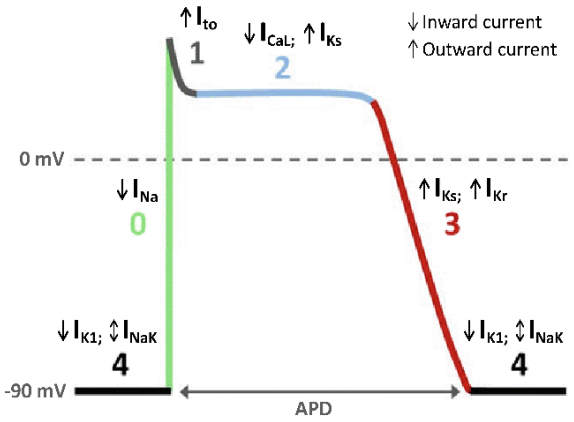

Figure 2.6 Phases of the action potential (AP) for a ventricular cell, showing the main ion currents responsible for each phase. Phase 0: upstroke (green), phase 1: early repolarization (gray), phase 2: plateau (blue), phase 3: complete repolarization (red) and phase 4: resting (black). The time from the onset of the AP upstroke to the return to resting potential is defined as AP duration (APD). Adapted from [52].

- **Phase 0 or depolarization.** This phase corresponds to the initial upstroke of the AP produced by an increment in inward flux of sodium ions (Na^+). The Na^+ influx is generated due to the application of an external stimulus that raises V_m to the threshold potential. When the V_m reaches this value, Na^+ fast channels open generating an inward Na^+ current (I_{Na}), which raises V_m to positive values.

- **Phase 1 or initial repolarization.** During this phase a small decrease in the AP is produced by the inactivation of Na^+ fast channels and by the activation of the transient outward potassium current (I_{to}) which extrudes potassium ions (K^+) out of the cell. This small repolarization leads the decrease of V_m to values around 0 mV.

- **Phase 2 or plateau.** This phase corresponds to the time interval during which V_m tends to remain constant due to a balance between the inward L-type calcium current (I_{CaL}), and the

outward slow delayed rectifier current (I_{Ks}). During this phase, the repolarization is slow and V_m remains around 0 mV.

- **Phase 3 or rapid repolarization.** This phase is the final stage of the AP. It causes by the closure of Ca^{2+} channels and the activation of the inward rectifier potassium current (I_{K1}). At this stage the V_m decreases from its plateau value to its RMP, around – 90mV.

- **Phase 4 or resting potential.** This phase is the period during which the cell remains at its resting state until a new electrical stimulus is applied. In this stage, the NaK pump removes the excess of Na^+ from the interior of the cell and introduces the excess of K^+ from the extracellular medium. In addition, I_{K1} remains slightly activated.

The cardiac muscle or myocardium consists of contractile cells (myocytes) distributed in interconnected muscle fibers allowing the propagation of the AP. Intercalated discs are structures located mainly at the ends of each myocyte (Figure 2.7). Within these structures there are low resistivity channels connecting the cytoplasm of two neighboring cells. These channels are called gap junctions and their function is to propagate the AP between myocytes. The AP propagation occurs due to the potential difference existing between a depolarized cell and neighboring cells at resting state. When this happens, an electrical current flows through gap junctions and stimulates the neighboring cells which are not in their refractory period. The CV of an AP varies depending on the propagation direction. In the ventricular muscle, the CV in the longitudinal direction of the fibers is 2 to 5 times higher than in the transverse direction [53]. This variation is due to structural anisotropy of cardiac tissue (cell morphology, ion channels, and gap junctions distribution), as well as to the conditions of the cellular environment.

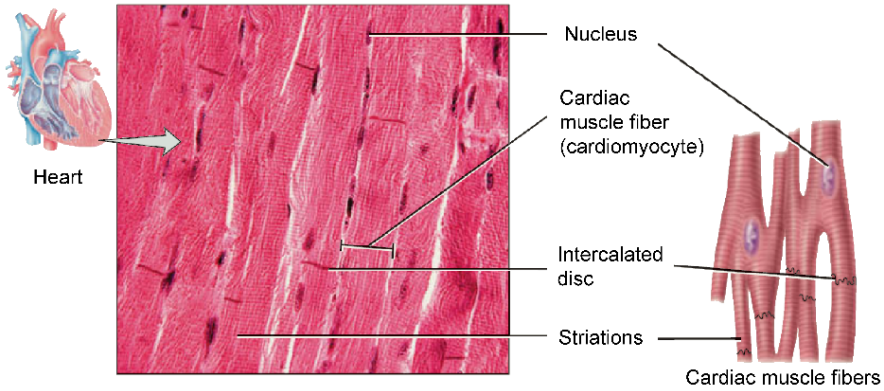

Figure 2.7 Microscopic photograph of a longitudinal section of the cardiac muscle, showing the striated fibers (cardiomyocytes) forming the cardiac muscle, and the intercalated discs connecting cardiomyocytes [39].

2.2.2 The electrocardiogram

During a cardiac cycle, APs propagating throughout the heart generate an electrical potential (or extracellular potential) that varies over time. An electrocardiogram (ECG) records this electrical activity of the heart on the body surface, providing relevant information for the diagnosis of abnormalities that affect the cardiac tissue.

The normal morphology of an ECG during a heartbeat consists of three main components representing the depolarization and repolarization of the myocardium. Figure 2.8 shows the typical morphology of an ECG with its waves. The P-wave represents the depolarization of the atria. The QRS complex corresponds to the depolarization of the ventricles, which in turn masks the atrial repolarization due to its high amplitude. It consists of a Q-, R- and S-wave. The T-wave represents the repolarization of the ventricles.

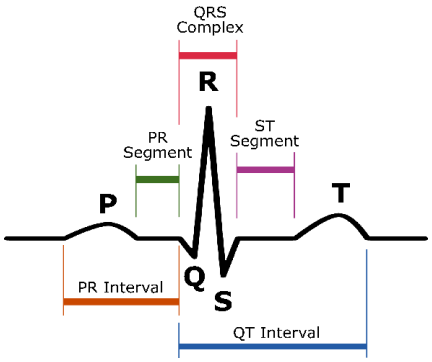

Figure 2.8 Morphology of a standard electrocardiogram (ECG), showing the P wave (atrial depolarization), QRS complex (ventricular depolarization) and Q wave (ventricular repolarization) [54].

Under normal conditions, the P-wave duration is less than 120 ms, and the QRS complex width is usually between 60 and 120ms [55], [56]. In addition, the PR interval or interval between the onset of atrial depolarization and the onset of ventricular depolarization varies between 120 and 200 ms [56], [57]. Values outside these intervals could be indicative of a cardiac pathology such as bundle branch block [58].

To properly record the ECG, 12 leads are used which record the electrical activity of the heart from different geometrical points. These leads are: three standard limbs leads (I, II, III), three augmented limb leads (aVR, aVL, aVF) and six precordial leads (V1 to V6). Each lead allows the analysis of a specific area of the heart, which can be useful to estimate the position of a cardiac injury within the myocardium [59].

The standard limb leads of the ECG are bipolar recordings that measure the potential difference between two different limbs. For the registration of lead I, the electrodes are set at the right arm and the left arm. For lead II, the electrodes are located at the right arm and left leg. Finally, for lead III the electrodes are placed at the left arm and left leg. In all cases the positive terminal is located at the second position indicated. In addition, the triangular distribution of the electrodes over the limbs (Einthoven triangle) allows the recording of the electrical activity of the heart in the front plane (left panel in Figure 2.9).

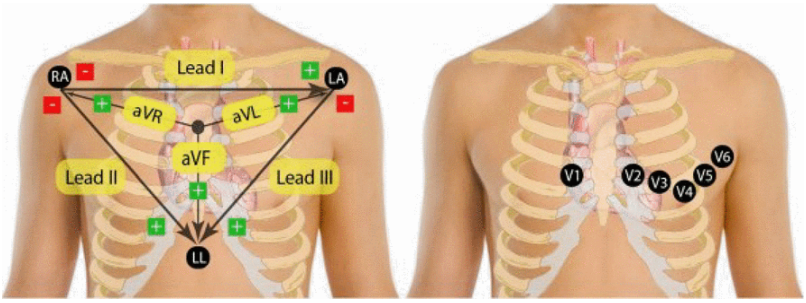

Figure 2.9 Twelve leads of the standard ECG. The left panel shows the standard limb leads (I, II, and III) and the augmented limb leads (aVL, aVR, and aVF). The right panel shows the precordial leads (V1-V6) [60].

The augmented limb leads are unipolar leads that record the difference of potential at a point: right arm (aVR), left arm (aVL) or left foot (aVF), with respect to the combination of the other two limbs. This last combination is known as the Goldberger central terminal and it represents the negative pole for the augmented limb leads. These latter also provide information about the electrical activity of the heart from the front plane (Figure 2.9).

The precordial leads are unipolar leads that record the electrical activity of the heart in the transverse plane, i.e., perpendicular to the plane of the other leads. For the recording of precordial leads (V1 to V6) the electrodes are located at six positions on the torso surface. These electrodes represent the positive terminal for each of the leads, while the Wilson's central terminal, which has a potential of approximately zero, represents the negative pole. In the right panel of the Figure 2.9 the positions of the ECG electrodes on the torso surface are shown, which are detailed below [61].

- **V1:** In the fourth intercostal space, on the right sternal border.
- **V2:** In the fourth intercostal space, on the left sternal border.
- **V3:** At the midpoint between V2 and V4.
- **V4:** In the fifth left intercostal space, on the midclavicular line.
- **V5:** Horizontally aligned with V4, on the anterior axillary line.
- **V6:** Horizontally aligned with V4, on the midaxillary line.

2.3 Modelling the electrical activity of the heart

2.3.1 Ventricular AP models

Mathematical models of the cellular AP are a complementary tool to understand electrophysiological phenomena, especially those which cannot be deduced from experiments in humans or animals.

In 1952, Hodgkin and Huxley developed the first AP model based on experimental measurements on squid neuronal axons [62]. Their model consisted of four differential equations that allow the analysis of the behavior of Na^+ and K^+ ion channels and the membrane potential. Later, several models have been developed based on the formalism of Hodgkin and Huxley. For instance, Luo and Rudy built in 1994 a more detailed model of the AP, which was based on data measured from guinea pig ventricular myocytes [63]. This last model included currents originated by pumps and exchangers, as well as an improved description of Ca^{2+} dynamics. In 1998, Priebe and Beuckelman formulated a first model of the human ventricular AP [64]. However, several ion currents included in this model were adopted from Luo Rudy's model for guinea pigs. The increase in the availability of experimental data, as well as the improvement of measuring techniques have favored the development of more complete models, such as ten Tusscher et al. 2004 [36], Grandi et al. 2010 [65], Carro et al. 2011 [66] and O'Hara et al. 2011 [37].

In the present thesis, the O'Hara AP model (ORd model) with some improvements was used. This is the most recent human ventricular AP model. Its formulation is based on experimental data from over one hundred non-pathological human hearts. Between the most relevant incorporations of the ORd model is the effects of Ca^{2+}/calmodulin-dependent protein kinase II (CaMK) on known ionic currents. As a result, the model can reproduce in a realistic way the APs of endocardial, epicardial and M cells. Figure 2.10 shows the graphic

scheme of the ventricular AP model developed by O'Hara et al. [37]. This model has recently been updated and improved by Tomek et al. [38].

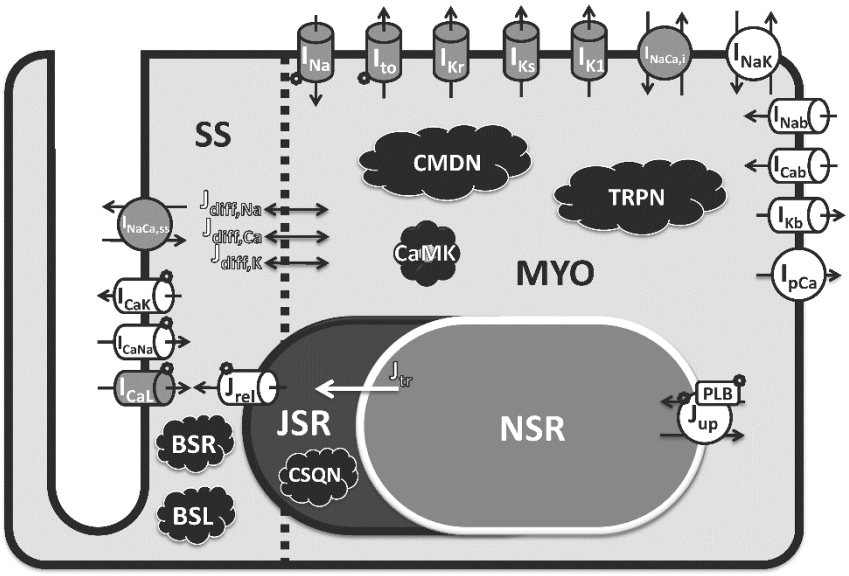

Figure 2.10 Schematic representation of the human ventricular AP model by O'Hara et al., showing the main ion currents and ion fluxes (labels starting with I and J, respectively), and the different subcellular compartments (MYO, JSR, NSR, SS) [37]. More details can be found in the text below.

The ORd model includes four intracellular compartments:

- Bulk myoplasm (MYO)
- Junctional sarcoplasmic reticulum (JSR)
- Network sarcoplasmic reticulum (NSR)
- Subspace (SS), representing the space near the T-tubules

The currents circulating through the membrane are:

- Na^+ current (I_{Na}; representing both fast and late components)
- Transient outward K^+ current (I_{to}).
- Rapid delayed rectifier K^+ current (I_{Kr})
- Slow delayed rectifier K^+ current (I_{Ks})
- Inward rectifier K^+ current (I_{K1})

- 80% of Na^+/Ca^{2+} exchange current ($I_{NaCa,i}$)
- Na^+/K^+ pump current (I_{NaK})
- Background currents (I_{Nab}, I_{Cab} e I_{Kb})
- Sarcolemmal Ca^{2+} pump current (I_{pCa})

The currents circulating into the subspace are:

- L-type Ca^{2+} current (I_{CaL}, with Na^+ and K^+ components I_{CaNa} e I_{CaK})
- 20% of Na^+/Ca^{2+} exchange current ($I_{NaCa,ss}$)

The ionic fluxes are:

- Ca^{2+} through ryanodine receptor (J_{rel})
- NSR to JSR Ca^{2+} translocation (J_{tr})
- Ca^{2+} uptake into NSR via SERCA2a/PLB (J_{up}; PLB - phospholamban)
- Diffusion fluxes from subspace to myoplasm ($J_{diff,Na}$, $J_{diff,Ca}$ y $J_{diff,K}$)

The Ca^{2+} buffers are:

- Calmodulin (CMDN)
- Troponin (TRPN)
- Calsequestrin (CSQN)
- Anionic SR binding sites for Ca^{2+} (BSR)
- Anionic sarcolemmal binding sites for Ca^{2+} (BSL)
- Ca^{2+}/calmodulin-dependent protein kinase II (CaMK)

2.4 Heart failure and left bundle branch block

Heart failure (HF) is a pathological condition in which the heart is unable to pump enough blood to meet the demand from the whole body. This disability is caused by a structural or functional anomaly which progressively worsens over time. The main electrophysiological changes affecting ventricular myocytes in HF conditions are AP prolongation and alterations in calcium handling [7]. In addition, the

number of gap junction proteins responsible for intracellular coupling between myocytes, called connexin 43 (Cx43), is reduced, leading to slower conduction velocity [8], [67]. As a result of these electrophysiological changes, HF patients are predisposed to develop complex ventricular arrhythmias which, in many cases, may be mortals [68], [69].

A great number of HF patients (approximately one third) also suffer from left bundle branch block (LBBB), which worsens their diagnosis [11]. LBBB is an abnormality in the left section of the CCS which blocks the propagation of electrical impulses to the LV. As a result, the LV is activated via the right bundle branch and RV, causing a delay in electrical activation, and subsequent contraction of the LV. Such a delay generates interventricular dyssynchrony, i.e. the RV contracts before the LV [12], [70]. In addition, due to late-activation of the LV free wall with respect to the interventricular septum activation, an intraventricular dyssynchrony occurs in the LV, i.e., the interventricular septum contracts before the LV free wall [13]. A dyssynchronyzed ventricular contraction reduces the efficiency of each heartbeat due to a reduction in the normal pumping capacity of the heart [71]. This reduced efficiency can accelerate the deterioration of the patient conditions [11], [14].

The ECG is a useful tool for the diagnosis of patients with HF and LBBB. Experimental and simulation studies have highlighted the widening, as well as a change in the morphology of the QRS complex on the surface ECG in patients with these pathologies [72], [73], caused by the intraventricular dyssynchrony [74]. Despite this fact, a standard criterion for LBBB diagnosis based on the ECG has not been established yet in the clinical practice.

Table 2.1 presents the definition of complete LBBB according to European [75] and American [76] guidelines, as well as the criteria suggested by Strauss and coworkers [73]. Figure 2.11 shows the ECG of a patient whose QRS width is increased from 76 ms to 148 ms with the development of complete LBBB.

ECG parameter for LBBB	ESC	AHA	Strauss
QRS duration (ms) >	120	120	♀130 ♂140
QS or rS pattern in V1	Yes	Yes	Yes
Positive T in V1	Yes	No	No
Normal ID R in V1 – V3	No	Yes	No
ID R in V5 ≥ 60ms	No	Yes	No
ID R in V6 ≥ 60ms	Yes	Yes	No
ID R in I ≥ 60ms	Yes	No	No
Notch-/slurred R in I, aVL and V5 – V6	No	Yes	No
Mild-QRS notch/slurring in ≥ 2 leads of V1 – V2, V5 – V6, I, aVL	No	No	Yes
RS pattern allowed in V5 – V6	No	Yes	Yes
Absent q in V5 – V6	No	Yes	No
Absent q in I	No	Yes	No
QS with positive T in aVR	Yes	No	No
Usually discordant T	Yes	Yes	No

Table 2.1 ECG parameters for complete LBBB according to guidelines of European Society of Cardiology (ESC) [75], American Heart Association (AHA)/American College of Cardiology Foundation (ACCF)/Heart Rhythm Society (HRS) [76], and Strauss et al. [73]. ID = intrinsicoid deflection. Adapted from [77].

Figure 2.11 ECG from a patient with an increase in QRS duration from 76ms (A) to 148ms (B) 1 year later with the development of complete LBBB. Changes in QRS morphology, such as mid-QRS notching in leads I and aVL, along with mid-QRS slurring in leads V5 and V6, are showed bottom [73].

2.4.1 Cardiac resynchronization therapy

As previously mentioned, patients with HF and LBBB have an electrical and therefore mechanical dyssynchrony of the ventricles which causes abnormal blood pumping. An effective treatment for this kind of patients is cardiac resynchronization therapy (CRT) [78]. CRT aims at restoring the electrical order of the heart, improving the ejection fraction of the LV (percentage of blood pumped during a heartbeat) and stopping arrhythmias. CRT is performed with a pacemaker which delivers coordinated biventricular pacing (standard modality) or LV-only pacing [79].

During standard CRT application, the LV pacing lead is placed into a coronary sinus venous branch, usually at the lateral or posterolateral location [80]. The RV pacing lead is located inside the RV, typically in the apical wall (Figure 2.12) [81]. In addition, a third lead is placed in the RA, which is used to monitor the sinus rhythm or as a source of stimulation and inhibition of impulses generated by the SAN. For synchronized contraction of the heart, the leads are paced with an atrioventricular delay (AVD) and interventricular delay (VVD). AVD is the time interval between the onset of electrical activity of the SAN (external or intrinsic stimulation) and the external CRT stimulation of the ventricles. VVD is defined as the time interval between the LV pacing and RV pacing during CRT application.

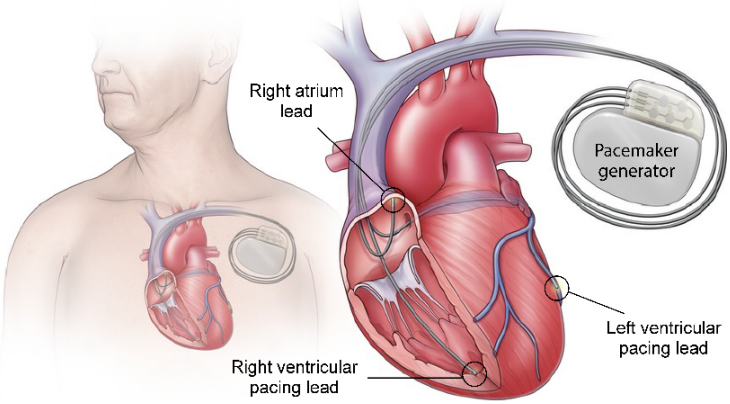

Figure 2.12 Placement of CRT pacemaker. Pulses generator is typically located in the subcutaneous tissue of the upper chest. The CRT leads are placed, one in the RA, other in the RV apical wall and a third within a coronary vein on the LV surface [82].

Although patients for CRT are selected under strict criteria, about 30% of them do not respond favorably to this therapy [19], [20]. In addition, severe complications such as RV perforation has been observed during CRT application [21]–[23]. Therefore, the optimization of pacing leads location and delays is crucial for a better response to CRT. Patients with a positive therapy response present QRS shortening and an increased LV ejection fraction, due to an

improvement in the electrical synchrony of the cardiac muscle [83], [84]. In addition, a reduction in mortality rate and HF-related hospitalizations have been observed in these patients, after implantation of the CRT device [17], [85].

2.5 Acute myocardial ischemia

In the healthy heart, the demand for oxygen of the myocardium is supplied by the coronary arteries. The most important are shown in Figure 2.13. If a partial or total arterial block is produced, commonly by an atheromatous plaque (atherosclerosis) [86], blood flow to the myocardium is reduced causing a lack of oxygen and nutrients to the affected tissue. This cardiac pathology is known as myocardial ischemia and its characteristics vary from patient to patient depending on both the magnitude and the duration of ischemia [87] (Figure 2.13). During the first 0 – 30 minutes after coronary artery occlusion, an acute phase of myocardial ischemia occurs [24]. However, if the occlusion persists for a longer period of time, it leads to irreversible damage and death of the ischemic cell, a phenomenon termed myocardial infarction.

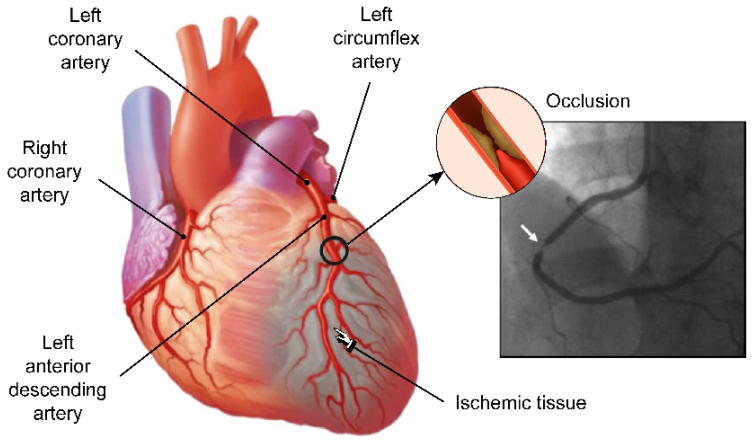

Figure 2.13 Example of myocardial ischemia caused by occlusion of left anterior descending artery. Adaptaded from [88], [89].

In the acute phase of myocardial ischemia, pathophysiological changes caused by the reduction of coronary blood flow lead to alterations in the electrical properties of ventricular tissue. As a result, potentially lethal arrhythmias, such as ventricular fibrillation, could be triggered [24], [90]. Experimental studies have reported that ventricular arrhythmias occur in two different stages during the first 30 min of acute myocardial ischemia [24], [91]. The first stage or phase 1A occurs between 2 – 10 min after the occlusion and it is highly arrhythmogenic due to electrophysiological heterogeneities between the ischemic and healthy tissues [90], as well as due to alterations in the conduction in the affected tissue [48]. Mapping recordings have shown that arrhythmias are usually triggered by reentrant processes [92], [93]. The most common arrhythmia in this phase is ventricular tachycardia (VT) and rarely evolves into ventricular fibrillation (VF) [90].

The second stage, or phase 1B, occurs within 20 – 30 min from the onset of ischemia [90]. At this stage, ventricular arrhythmias are also generated. However, the trigger mechanisms of these arrhythmias are not precisely defined [94], [95]. Animal experiments have shown a greater evolution to VF and sudden death in this phase [96], [97], although the incidence of arrhythmias is higher during phase 1A [97]. In this thesis, part of our work focuses on studying the role of the main pathophysiological changes due to ischemia (hyperkalemia, hypoxia, and acidosis) in arrhythmogenesis, during the first 10 minutes of ischemia (phase 1A).

2.5.1 Pathophysiological components of acute myocardial ischemia

Acute myocardial ischemia is a complex process that involves a series of pathological changes at the cellular and tissue levels, mainly hypoxia, acidosis and hyperkalemia. Each change or ischemic component evolves differently as ischemia progresses [98], [99]. In addition, a spatial variation of these components within the ischemic zone has been reported [28], [98], [100].

Hypoxia. It is a reduction of the oxygen reaching tissues, which produces a deterioration in cellular metabolism and a change in intracellular concentrations of adenosine tri-phosphate ($[ATP]_i$) and adenosine di-phosphate ($[ADP]_i$). In physiological conditions, the $[ATP]_i$ value has been reported to be between 5 – 10 mM [101]. After 10 minutes of ischemia, a study in dog hearts recorded a reduction by 61% with respect to its control value [102]. On the other hand, the experiments by Weiss et al. [101] in rabbits reported an $[ADP]_i$ level of 15 mM in normal conditions and 100 mM after 10 min of ischemia.

Hyperkalemia. This is defined as an increase of the extracellular potassium concentration ($[K^+]_o$), which is developed in two stages. At the initial stage, $[K^+]_o$ rapidly increases until it reaches a plateau level within the first 5 – 10 minutes after the coronary occlusion [94], [98]. Then, $[K^+]_o$ is maintained approximately constant and eventually increases again after 15 – 20 minutes of ischemia [98], [103]. An experiment in pig hearts showed that $[K^+]_o$ rises from 5.4 mM to approximately 11 mM at a site in the center of the ischemic region, 10 minutes after the coronary occlusion [98]. Then, it rises again from minute 20 onwards. However, these values varied depending on the measurement site.

Acidosis. It consists of the reduction of the intracellular and extracellular pH (pH_i and pH_o, respectively). As a result, I_{Na} and I_{CaL} currents decrease during cell depolarization [104], [105]. Studies by Mohabir et al. [106] and Garlick et al. [107] in perfused rabbit and rat hearts, respectively, reported a decrease in pH_i of around 0.7 pH units after 10 min of ischemia compared with its normal value (between 7.0 and 7.2). On the other hand, an experiment in pigs during five successive ischemic episodes showed that pH_o decreases from 7.4 in normal conditions to a value between approximately 6.3 and 6.9 within 10 min of occlusion, depending on the ischemic episode [108].

2.5.2 Electrophysiological effects of myocardial ischemia

The main components of ischemia produce several alterations in the electrical activity of the affected cells, which can trigger ventricular arrhythmias. These electrophysiological alterations include: reduction in cell excitability, decrease in conduction velocity (CV), shortening of the action potential duration (APD), and prolongation of the effective refractory period (ERP) (Figure 2.14) [90]. Each of these changes is described below.

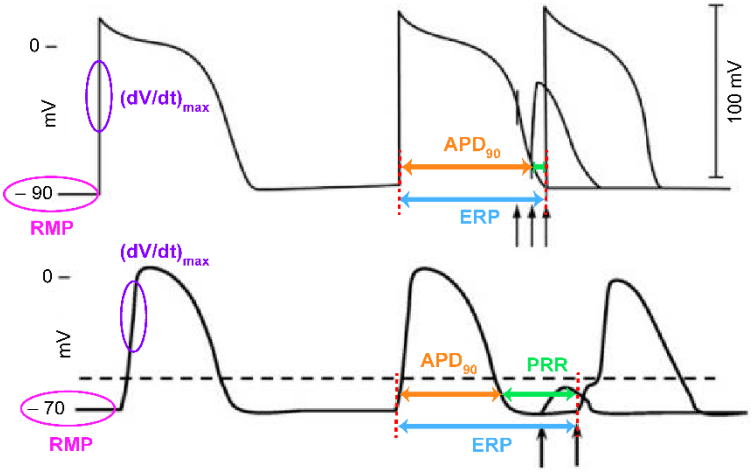

Figure 2.14 Schematic illustration of a normal (top) and ischemic (bottom) myocyte AP, showing the main alterations caused by acute ischemia. RMP is the resting membrane potential, $(dV/dt)_{max}$ is the maximum upstroke velocity, APD_{90} is the AP duration at 90% of repolarization, ERP is the effective refractory period and PRR is the post-repolarization refractoriness. Black arrows indicate the instant of application of an electrical stimulus. Adapted from [109].

During acute ischemia, $[K^+]$ raises producing a diastolic depolarization of the membrane, i.e., the RMP increases to a less negative value [110], [111]. In the porcine heart, RMP changed from normal values ≈ –90 mV to between –65 and –60 mV within 7 – 10 min after left anterior descending artery occlusion [112]. This depolarization decreases cell excitability due to reduced availability of Na^+ channels [113]. As a result, the maximum upstroke velocity

$(dV/dt)_{max}$ and the CV of AP propagation are reduced [48], [113], and the recovery period of the excitability of the cell (or ERP) is extended (Figure 2.14) [114]. A reduction in the transmural CV from 0.55 m/s at the onset of ischemia to 0.25 m/s after 3 min of occlusion was observed in humans by Sutton et al. [114]. On the other hand, Taggart et al. reported an increase in the ERP of 10 ms in group 1 and about 100 ms in group 2 [48]. In the latter case, a lower amplitude stimulus was applied.

In a non-ischemic myocyte, the recovery of excitability closely coincides with the end of the AP, allowing the myocyte to be stimulated with a suprathreshold electrical stimulus when it reaches the RMP [109], [115]. In acute ischemia, the recovery period is longer than the repolarization time, giving rise to a phenomenon called post-repolarization refractoriness (PRR) [114], [116]. PRR consists of a decoupling between the ERP and the APD (Figure 2.14). This phenomenon is potentially arrhythmogenic because the dispersion in recovery of excitability of the cardiac tissue favors unidirectional block of AP propagation, allowing the generation of reentrant arrhythmias [24], [117].

Another electrical alteration due to ischemia is APD shortening. It is caused mainly by the activation of ATP-sensitive K^+ current ($I_{K(ATP)}$), a consequence of hypoxia [113], [118]. In addition, Shaw and Rudy [113], and Ferrero et al. [118], in their respective studies reported that the increase of the extracellular K^+ level is also a secondary factor which slightly affects the APD. An experimental study in humans showed that APD decreased by approximately 60 ms after 3 min of ischemia [114].

2.5.3 Electrographic changes during acute myocardial ischemia

ECG is a commonly used tool for diagnosis of various cardiac pathologies, such as acute myocardial ischemia. Due to alterations in the electrical activity of cells affected by ischemia, typical and atypical

changes in ECG can be observed, mainly in the ST segment (interval between the end of the QRS and the onset of the T wave) and in the T wave [119]. These changes vary depending on the time, site, and extent of ischemia [120].

Clinical reports and simulation studies have reported a displacement of the ST segment during ischemia [119]–[122], although the presence of other factors, such as bundle branch block, can complicate diagnosis [61]. In a heart with subendocardial ischemia, leads near the affected area record a horizontal or down-sloping ST depressed at the J-point (end of the QRS complex) [61], [123]. Conversely, when the myocardium presents a transmural ischemia, which involves the full thickness of the myocardium, leads near the ischemic region record a ST elevation [61], [122], [123]. These different behaviors in the ST segment are due to the direction of injury currents, which flow from healthy or less injured tissue toward ischemic region [32], [123]. Figure 2.15 shows an example of subendocardial and transmural ischemia (left), as well as an ECG in both cases (right).

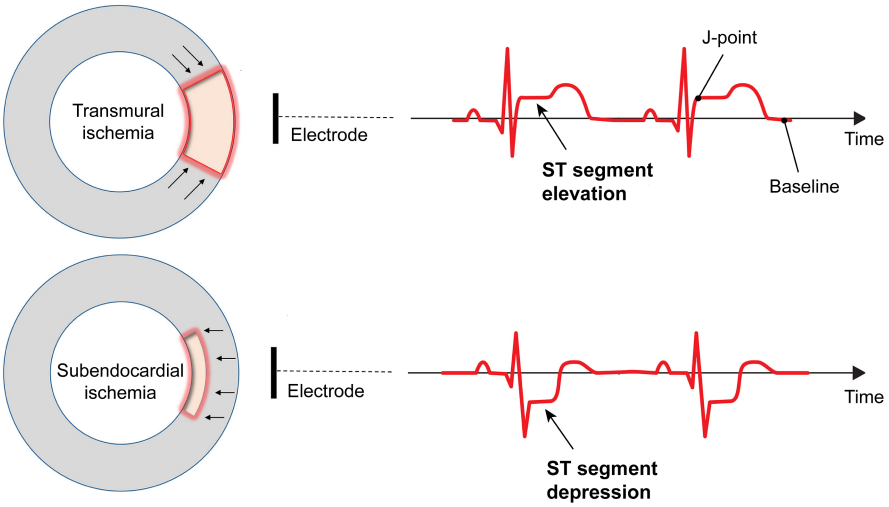

Figure 2.15 Schematic illustration showing the ST elevation during transmural ischemia (top), and ST depression in subendocardial ischemia. Modified from [124].

A second electrographic parameter affected by myocardial ischemia is the T wave morphology, which can vary in different ways [119]. The existence of tall symmetric T waves (referred to as hyperacute T waves) is an early electrocardiographic indicator of acute ischemia [61], [125]. For instance, an isolated tall T-wave in V1 to V3 leads could be a sign of ischemia on the posterior wall of the LV [119]. On the other hand, flattened, inverted or biphasic T waves have been also observed as ischemia progress over time (Figure 2.16) [119], [121]. However, inverted T waves are not only specific to myocardial ischemia and these need to be correlated with clinical history for a proper diagnosis.

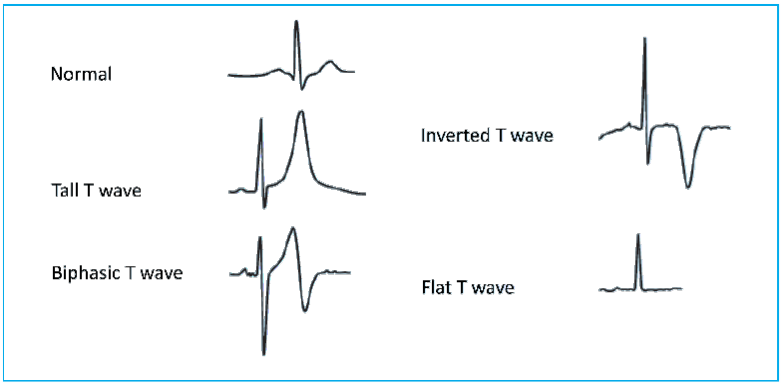

Figure 2.16 T wave changes associated with myocardial ischemia [119].

2.6 Cardiac arrhythmias and reentries

A cardiac arrhythmia is an abnormal heart rhythm disturbance caused by dysfunctions in the electrical activity of the heart, which can lead to sudden cardiac death. There are several categories of arrhythmias depending on whether the heart rate is faster, slower or irregular. Arrhythmias where the cardiac rhythm is less than 60 beats per minute (bpm) are called bradycardias. Conversely, when the heart rate is above 100 bpm, such arrhythmias are known as tachycardias. Finally, the most common type of cardiac arrhythmia characterized by irregular rapid rhythm is named fibrillation (usually at over 300 bpm).

Based on the location where cardiac arrhythmias occur, i.e. in the atria or ventricles, these are called supraventricular or ventricular arrhythmias, respectively. In general, as the ventricles are responsible for pumping blood to the whole organism, ventricular arrhythmias are the most serious of both arrhythmias [126]. These include ventricular tachycardia (VT) and ventricular fibrillation (VF). During VT, the ventricle contraction is accelerated due to a faster self-sustaining excitation wave that overrides the sinus rhythm. When VF occurs, the electrical activity of the ventricles is completely disorganized, making the heart unable to pump normally and efficiently. Figure 2.17 shows a characteristic ECG signal of VT and VF.

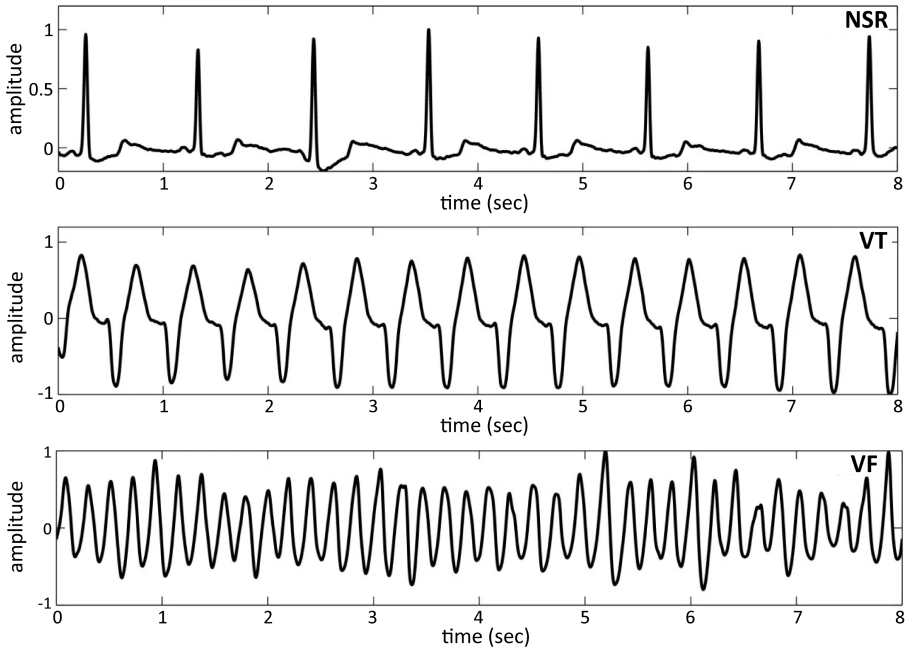

Figure 2.17 Characteristics ECG signals of normal sinus rhythm (NSR), ventricular tachycardia (VT) and ventricular fibrillation (VF). Adapted from [127].

During acute myocardial ischemia, reentries represent the fundamental mechanism of generation of VT and VF. A reentry is defined as a repetitive propagation of the activation wavefront returning quasi-periodically to its site of origin, after it recovers excitability, to

reactivate that site [128]. The most common reentrant patterns experimentally observed are single circus and double circus (figure-of-eight reentry) (Figure 2.18) [112], [129]. For a reentry to occur, a set of requisites is necessary, which are described below [130].

1. The presence of joined myocardial tissue with different electrophysiological properties, conduction and refractoriness. This can create an area of block or unexcitable tissue, which the wavefront can circunvalate.
2. Occurrence of a unidirectional conduction block.
3. The existence of a path of slowed conduction that allows sufficient delay in the conduction of the circulating wavefront to enable the recovery of the refractory tissue proximal to the site of unidirectional block.
4. The appearance of an initiating trigger, such as an ectopic beat or abnormal automaticity.

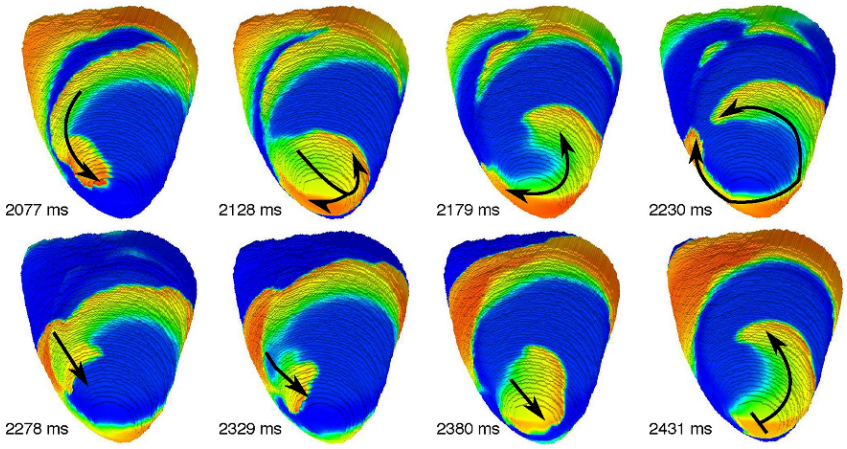

Figure 2.18 Reentry pattern that changes from a single circus to a double circus (figure-of-eight) to then come back to a single circus movement [34].

CHAPTER 3

Optimization of lead placement in the right ventricle during cardiac resynchronization therapy

3.1 Introduction

Heart failure (HF) constitutes a major public health problem worldwide and much attention has been paid to the understanding of the arrhythmogenic mechanisms in the failing heart induced by the structural, electrical, and metabolic remodeling. Heart failure is also characterized by a compromised ventricular contraction, which is fundamental for an optimal cardiac function. Lack of synchrony in heart contraction is worsened when the failing heart is also affected by left bundle branch block (LBBB). These patients present electrical and mechanical ventricular dyssynchrony causing pump dysfunction, reduced functional capacity, and myocardial remodeling. In particular, LBBB is associated with delayed contraction of the left ventricle (LV), reduced ventricular performance and widening of the QRS complex.

The relative QRS duration (QRSd) provides a powerful prognostic value for patients with HF and is a primary indicator of eligibility for cardiac resynchronization therapy (CRT). CRT helps to reduce mortality and morbidity associated with HF [17], [131]. Recent studies have also concluded that patients with LBBB are more likely to respond to CRT than those with right bundle branch block (RBBB) or nonspecific interventricular conduction delays (IVCDs) [19], [132].

During CRT, two synchronized electrical stimuli are usually delivered to reduce ventricular dyssynchrony. One stimulation lead is usually placed on the apex of the right ventricle (RV), and the other one on the epicardium of the LV lateral wall. Patients with positive therapy response present QRS shortening and an increased LV ejection fraction (LVEF) [83], [84], [133]. However, around one third of the patients do not respond favorably to this therapy [19], [134] and implantation issues, such as perforation of the RV apex, have been observed.

Optimal location of pacing leads is crucial to achieve the best degree of ventricular synchrony. LV lead position has been recognized as an important determinant for response to CRT since the initial development of this therapy [135]–[137]. Experimental studies and computational models [138] have been used to optimize LV lead location. In current guidelines [80], the LV posterior-lateral wall is the recommended LV region for CRT application. Several studies have reported the beneficial results of pacing from the lateral region of the LV [139]. However, there are still several open questions.

First, as suggested by Zanon et al. the ideal LV lead placement should be the latest electrical intrinsic activated region [140], typically the postero-lateral wall [141]. This location provided the maximum increase in contractility, expressed as the highest value of the first derivative of LV pressure over time (LV dP/dt_{max}). However, the electromechanical modelling study by Pluijmert et al. [142] determined that in fascicular block conditions the latest activated area did not provide the maximum response in contractility. A different criterion

suggested in the literature is to place the LV lead in the site corresponding to the shortest QRS registered. Nevertheless, simulation studies that apply this last non-invasive criterion [143], [144] estimated QRSd through calculation of the total ventricular activation time (TAT), a parameter not easily accessible in clinical or even experimental settings. In addition, studies such as Potse et al. [72] have observed that biventricular pacing did not change QRS duration but reduced total ventricular activation time when the stimulation was applied in one point of the LV free wall.

Second, there is controversy about whether a higher degree of synchrony can be achieved by stimulating from points in the RV other than the apex [145], [146]. Third, individualized programming of the atrioventricular delay (AVD) and interventricular delay (VVD) intervals is not typically performed in most patients in the normal clinical practice, and it has been primarily reserved for non CRT responders [147]. The largest trials studying CRT used various methods to optimize these intervals, most frequently based on echocardiography and intracardiac electrogram interval measurements, but unequivocal proof of the benefit brought by optimization is still lacking [148]–[150]. Echocardiography presents inherent variability of results and is highly operator dependent. Optimization based on intracardiac electrogram intervals has not proved yet to be of clear benefit above arbitrary atrioventricular interval [151]. Another optimization method based on the surface ECG uses fusion with intrinsic conduction and avoids echocardiographic atrioventricular and biventricular optimization [152]. Applying this method Arbelo et al. determined that electrocardiographic optimization improved invasive LV $dP/dt_{max.}$ Similarly, randomized studies demonstrated that electrocardiographic optimization had superior LV remodeling at 6-month follow up although survival was not different, compared with optimization by echocardiography [153], [154]. All these results suggest that minimizing QRSd could be used as a non-invasive method to optimize CRT.

In this study, we used a 3D biophysical model of the heart and torso to optimize pacing leads location, AVD, and VVD settings during CRT procedure, based on the shortest QRS duration measured on the torso surface. Results were compared with other optimization criteria. This analysis was used to define an electrical biomarker that relates the optimal lead configuration with the observed surface electrocardiogram signals.

3.2 Methods

3.2.1 Anatomical model

A 3D biventricular model of the heart was built from segmentation of a DE-MRI images stack. The cardiac DE-MRI was acquired from the Hospital Clinic Universitari de Valencia (Valencia, Spain). Regarding the ethical considerations, the protocol was approved by the Ethics Committee for Clinical Research of the Hospital Clinic Universitari de Valencia, which certifies that the present study was conducted in accordance with the recommendations gathered in the Declaration of Helsinki, originally adopted by the General Assembly of the World Medical Association in 1964, and in its subsequent revisions. Furthermore, the patient, who underwent the standard clinical protocol, gave written informed consent for the use of his anonymized clinical data in this study.

Manual image segmentation was performed using Seg3D software (Scientific Computing and Imaging Institute, University of Utah, USA) [155], including papillary muscles and main endocardial trabeculations (Figure 3.1A). From the segmented DE-MRI stack, a surface model of the ventricles was generated and subsequently meshed using MeshGems-Hexa (Distene S.A.S., Bruyeres-le-Chatel, France), obtaining a hexahedra-based volume mesh comprised of 4 million nodes (vertices) and 3.71 million elements, with an average edge length of 0.4 mm (see appendix A for further detailed information).

Transmural heterogeneity (Figure 3.1B) was defined by three different transmural layers for endocardial (blue), midmyocardial (green), and epicardial (red) cells within the volume mesh of our ventricular model, spanning 17%, 41%, and 42% of ventricular wall thickness, respectively [156]–[158].

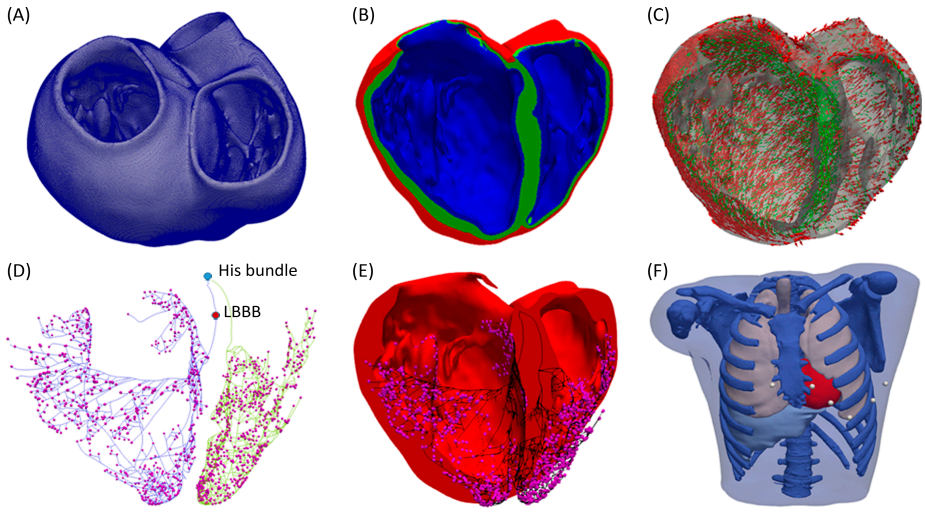

Figure 3.1 Anatomical model. (A) Biventricular hexahedral mesh of a segmented human heart. (B) Model color-coded to show the assignment of the elements to the different cellular model in order to model the transmural heterogeneity: endocardial cells (blue), midmyocardial cells (green) and epicardial cells (red). (C) Arrows indicating the principal myofiber orientation of epicardial (red) and midmyocardial (green) cells. (D) Purkinje System (PS), including three main LV branches (posterior, septal, anterior) and RV main brunches (septal and anterior). Purkinje-Junctions are represented as magenta spheres. His Bundle, and the location of the LBBB are labeled in the model. (E) PS (black) coupled to the biventricular model. (F) Torso model with the biventricular mesh embedded (red) and precordial leads location (white).

To include the anisotropy of the cardiac muscle through fibers orientation (Figure 3.1C), we implemented Streeter's rule-based method [159] modeled by the set of equations described in [160] defining the helix (α_h) and transmural (α_t) angles. In papillary muscles and endocardial trabeculations, fibers are known to be aligned parallel to the longitudinal axis of those anatomical structures [161]. In order to reproduce such configuration, we performed the topological

skeletonization of the volume mesh to extract the medial axes of each one of those structures, what enabled to properly assign the fiber orientation. Finally, we performed a Gaussian smoothing with a 3D kernel to soften abrupt transitions in fibers direction between the myocardial wall and the papillary muscles and trabeculations.

A Purkinje system (PS) network (Figure 3.1D, E) was developed based on a stochastic grown method [162] formed by linear elements. The RV section was composed of two main branches, one descending to the apex, and another extending to the surroundings of the moderator band, with several subdivisions. The LV section was formed by three main branches with several subdivisions: one descending to the apex towards the papillary muscles of the lateral wall, another one to the anterior wall, and the last one to the posterior wall. The location of the PMJs that start the endocardial activation from the main PS branches was optimized to obtain a typical ECG wave morphology in the precordial leads. Purkinje-Myocardial junctions (PMJs) conductivity were adjusted to allow retrograde and anterograde electrical propagation. A total of 1391 PMJ were distributed across the RV and LV.

The biventricular mesh was fit into a human torso mesh [163] to be able to properly solve the forward problem in electrophysiology and simulate the electrocardiogram (ECG) (Figure 3.1F). The torso dataset was obtained from the online open repository at the Centre for Integrative Biomedical Computing (CIBC) from University of Utah [164]. The torso volume mesh was made of tetrahedral elements of 0.5 mm spatial resolution. Note that the problem of passive propagation of extracellular potentials, i.e. only diffusion without reaction component, does not require such a fine spatial resolution outside the heart domain [165]; for this reason, the torso mesh is highly refined only in the region where it intersects with the ventricles (see appendix A for complementary description).

3.2.2 Electrophysiological model

O'Hara et al. [37] model is the most recent action potential model developed for human ventricular electrophysiology. Our simulations were conducted using a modified version of this model to achieve realistic conduction velocity and electrical propagation in 3D ventricular tissue. For this reason, the original fast sodium current (I_{Na}) formulation was modified. Firstly, the steady state inactivation (h_{ss} and j_{ss}) and activation (m_{ss}) gates were changed as in Passini et al. [166] and Mora et al. [167], respectively. Secondly, the time constant of the inactivation gates was modified as in Dutta et al. [168]. Finally, the sodium conductance (G_{Na}) was decreased to 23% of its original value to obtain approximately a maximum upstroke velocity (dV/dt_{max}) of 260 V/ms as in the original O'Hara et al. [37] model. Furthermore, the late sodium current (I_{NaL}) conductance (G_{NaL}) was duplicated to maintain the relationship between I_{NaL} and peak I_{Na} observed in voltage-clamp experiments as described in Mora et al. [167]. All these changes are detailed in the appendix A together with the action potential (Figure A.1) obtained with the original and modified O'Hara et al. models. The action potential model for Purkinje cells developed by Stewart el al. [169] was used in the cardiac conduction system.

The electrical propagation through the ventricles was calculated by solving the monodomain equation (Equation 3.1) using ELVIRA FEM software [170],

$$\nabla\cdot(\mathbf{D}\nabla V_{\mathrm{m}}) = C_{\mathrm{m}}\frac{\partial V_{\mathrm{m}}}{\partial t} + I_{\mathrm{ion}} + I_{\mathrm{stim}} \qquad (3.1)$$

where $\mathbf{D}$ is the equivalent conductivity tensor, V_{m} the transmembrane potential field, C_{m} the cell membrane capacitance, I_{ion} the transmembrane ionic current and I_{stim} the transmembrane stimulation current.

The ECG was simulated by solving the extracellular potential (φ_e) from the equation

$$\nabla\cdot\left([D_i+D_e]\nabla\varphi_e\right)=-\nabla\cdot(D_i\nabla V_m) \quad (3.2)$$

where D_i and D_e are the volume-average conductivity tensors of the intra and extracellular domains, respectively [171]. The reaction-diffusion simulation was run on the biventricular mesh. The right-hand side of Equation 3.2 was evaluated on this fine mesh and then interpolated on the coarser torso mesh. The extracellular potential was solved on the coarser mesh. The precordial ECG leads were then computed by extracting the extracellular potential at the electrode locations taking into account the Wilson terminal, as in clinical practice (see appendix A for details).

In order to establish the conductivities that will define the conduction velocities (CV) in the heart domain, we performed a set of test simulations on a 3D slab model (20x20x6 mm) composed of regular hexahedral elements (voxels) with an edge length of 0.4 mm, matching the average length in the ventricular model. As a result, we set the conductivity values to 0.5 S/m and 0.1 S/m for longitudinal (σ_L) and transversal (σ_T) conductivity, respectively. This resulted in a CV of 0.61 m/s along the fiber direction and of 0.29 m/s in transverse direction. These values are consistent with experimental measurements in human ventricles [48].

CV in the PS was adjusted to 2.5 m/s [46], [47]. The electrical propagation in the torso mesh was considered isotropic and specific conductivities were assigned to each organ: i) myocardium (4.589 mS/cm), ii) bones (0.200 mS/cm), iii) liver (0.277 mS/cm), iv) lungs (0.389 mS/cm), v) muscle (2.390 mS/cm), and vi) blood (7.0 mS/cm) based on several experimental studies [172]–[174].

3.2.3 Pathological model

To simulate LBBB, an electrical block was generated on the left section of the PS before the bifurcation into three sub-branches by

imposing null conductivity in two linear elements (see Figure 3.1D). HF condition was modeled by a reduction of 50% in CV, in accordance with protein connexin43 (Cx43) reduction observed in failing tissue [7]. The decrease and lateralization of this protein is associated with reduced longitudinal conduction velocity [67], [175], [176].

3.2.4 Stimulation protocols

For the present study a 3D anatomical model of the ventricles was generated, which does not include the geometry of the atria. Therefore, the intrinsic activation from the sinoatrial node was simulated by applying an electrical stimulus to the His bundle, either in healthy or HF + LBBB conditions (see Figure 3.1D). CRT leads were modeled as 0.5 mm3 cubes injecting a transmembrane current of 400 μA/μF in amplitude (see Equation 3.1). Four scenarios of CRT pacing were defined for HF + LBBB conditions with different combinations of atrioventricular delay (AVD) and interventricular delay (VVD) for each lead location configuration (AVD = 100 ms, VVD = 0 ms; AVD = 100 ms, VVD = 30 ms; AVD = 140 ms, VVD = 0 ms; AVD = 140 ms, VVD = 30 ms).

AVD is the time delay between the instant of initial activation of the sinoatrial node (external or intrinsic stimulation) and the instant of time of external CRT stimulation of the ventricles. To set the value of AVD in our simulations, several considerations were taken into account. Firstly, the typical duration of PR interval observed in LBBB patients is 200 ms [177], which is the time that takes the initial atrial stimulation to spread through the atria (100 ms), plus the time delay in the atrioventricular (AV) node (80 ms) [178], plus the propagation time from the His bundle through Purkinje system to finally reach the first activation site of the ventricles (20 ms approximately). Secondly, our model does not include the atria or the AV node as mentioned before, so that the intrinsic activation was simulated by stimulating His bundle, which is included in our 3D model.

In our simulations, different AVDs could be simulated by changing the stimulation time of the His bundle (coming from the intrinsic activation of the atria). Thus, an AVD of 100 ms was modeled by applying an electrical stimulus to the His bundle of 80 ms after ventricular leads activation. Indeed, when we applied the external CRT ventricular stimulation, 100 ms after initial activation of the sinoatrial node (AVD of 100 ms), this intrinsic activation had reached the atrial side of the AV node (this takes 100 ms) and needed still 80 ms to reach His bundle (delay needed in the AV node). In the case of an AVD of 140 ms, the electrical stimulus in the His bundle was applied 40 ms after ventricular leads activation. Indeed, when we applied the external CRT ventricular stimulation, 140 ms after initial activation of the sinoatrial node, this intrinsic activation had reached the AV node in 100 ms and 40 ms of delay in the AV have also elapsed, the stimulus needed 40 ms more to reach the His bundle, and this is why we stimulated the His bundle 40 ms after the ventricles. Additionally, VVD was set to 0 ms (stimulation in both ventricles simultaneously) and 30 ms (the RV was stimulated 30 ms after the LV), according to the time ranges used in clinical practice [80], [179].

3.2.5 Leads location

The RV septal wall is an alternative location for the RV pacing lead in CRT. In this study, three different locations for the RV pacing lead were tested based on medical protocols and research works [145], [146]. The RV septal electrode was placed in the apex (RVapex), middle septal region (RVmid) or upper region near the outflow tract (RVupper) (Figure 3.2A).

For the LV pacing lead location, the LV free wall was divided into three different regions [137], [180]: anterior, lateral, and posterior (Figure 3.2B). In addition, each region was divided into three segments: apical, mid-cavity, and basal, leading to a set of nine segments for the LV free wall as illustrated in Figure 3.2C as in Singh et al. [137]. The LV pacing lead was placed in the middle of each segment, both in the

epicardial (Figure 3.2C) and endocardial wall (Figure 3.2D) to represent and simplify the different possible positions of the electrode within the same region, due to variety of veins configurations observed in CRT patients.

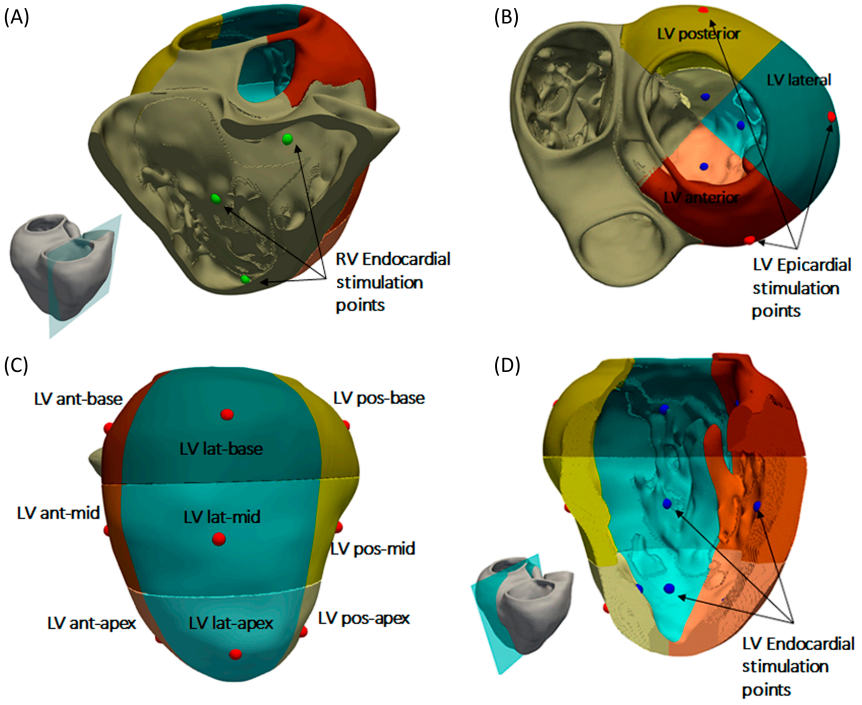

Figure 3.2 Heart subdivisions and stimulation points for CRT protocol. (A) RV septal endocardial stimulation points tested (green). (B) Left ventricular (LV) free wall region divided into three regions: posterior (yellow), anterior (brown), and lateral (green). (C) Subdivisions of the three LV free wall regions into nine segments. Epicardial stimulation points tested in the middle of each segment (red dots). (D) Endocardial stimulation points tested in the LV free wall (blue dots).

To summarize, we have a total of 54 lead location configurations obtained by combination of the three RV lead locations with eighteen LV lead locations (9 epicardial and 9 endocardial) for the application of the CRT protocol.

3.2.6 QRS measurements

QRS complex was computed in the precordial leads location on the torso surface for each CRT configuration and QRSd was measured using an algorithm implemented in Matlab software (Mathworks Inc., Natick, MA, USA). This algorithm determines the beginning and end of the QRS complex based on the first and second derivate of the electrocardiographic signal (see Figure A.2 in the appendix A). The QRS onset was calculated applying a threshold in the first derivate to determine a change in the slope. To estimate the end of QRS complex, additional signal processing was required as baseline was not reached in most CRT configurations. A time interval after the QRS complex was set based on the 95% of the accumulated area under the curve of the second derivate, and the end of the signal. To set the end of the QRS, the lowest value of the first derivate was used within this interval (see appendix A for details). Once the beginning and end of QRS complex were determined for each precordial lead, the QRSd was calculated as the time interval between the onset beginning and the latest end of the QRS among all leads [76]. This is the recommended criterion by the American Heart Association, the American College of Cardiology Foundation, and the Heart Rhythm Society (AHA/ACC/HRS). The total activation time (TAT) of the ventricular mesh was estimated as the time interval between the first and last depolarized node mesh above a threshold of –10 mV.

3.2.7 Correlation analysis

Shortest QRSd was the criterion applied to evaluate the optimal location of the LV lead for different positions of the pacing lead in the RV. However, the total activation time (TAT), QRS area (QRSa) and the time to 90% of activated tissue (t_{90}) are other important parameters that have been used to evaluate CRT response. For this reason, three linear correlations between these parameters were performed using Pearson correlation method. Values of $p < 0.05$ were considered

statistically significant. Values for the analysis are shown in Table A.1–A.5 in the appendix A.

3.3 Results

3.3.1 Model validation

Simulated ventricular activation maps for non-pathological and HF conditions with LBBB (HF + LBBB) are shown in Figure 3.3A. In healthy conditions, the electrical impulse traveled from the bundle of His to the first activation point in the LV endocardium in approximately 20 ms. RV activation started 10 ms after the onset of LV activation [47]. The computed time until all the ventricular tissue was depolarized (total activation time or TAT) was approximately 103 ms, in accordance with human data [181]. The outflow tract and the posterobasal area were the last activated regions in the RV, while the latest areas depolarized in the LV were the anterior mid and basal regions.

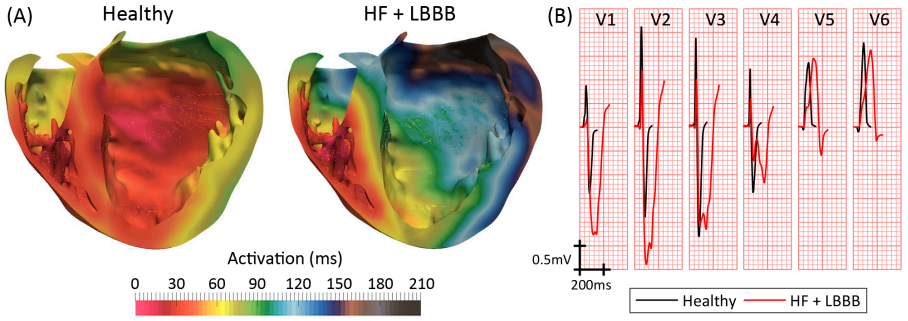

Figure 3.3 Model validation. (A) Cross section of biventricular model showing color coded local activation maps of a healthy (left) and pathological heartbeat (right). (B) Precordial leads signals recorded on torso surface.

Under HF + LBBB conditions, activation began in the RV endocardium and reached the LV endocardium in the apical septal region after 46 ms from the onset of the LV depolarization. This is in agreement with the data recorded experimentally by Auricchio et al. [182]. The last activated region in the LV was the lateral wall in

accordance with the study of Mafi-Rad et al. [183]. Additionally, the TAT was increased in 104% compared to a healthy heart.

Figure 3.3B shows the computed QRS complexes in the precordial leads for simulations in a healthy heart and under HF + LBBB conditions. For non-pathological conditions, QRS duration (QRSd) was 93 ms, while in HF + LBBB QRSd was increased to 190 ms. Both values are within experimental ranges [184], [185]. Additionally, QRS complexes in HF + LBBB simulations present an rS pattern (small R wave followed by a bigger S wave) [186] in leads V1 and V2 and a mid-QRS notching in several leads. These observations are in agreement with the criteria proposed by Strauss et al. [73] to define complete LBBB.

3.3.2 QRS duration during CRT

A total of 54 electrode placement configurations with four different delays (two AVD and two VVD configurations) settings were tested for the CRT simulations. QRSd values are shown in Table A.1 in the appendix A.

Figure 3.4 compares the simulated QRS complexes in a scenario with HF + LBBB before (red traces) and after (green traces) the application of the CRT protocol. The optimal configurations in terms of shortest QRSd for the RV lead placement tested (apex, mid septum, and upper septum) are shown in the different rows. Epicardial versus endocardial LV lead stimulation for those configurations are shown in columns.

Firstly, we analyzed the optimal lead placement. The shortest QRSd among all configurations tested was obtained when the RV lead was placed in the upper septum near the outflow track (third row). Furthermore, for all RV lead placement the optimal location of the LV lead, both in the epicardium and endocardium, was the LV mid posterior wall.

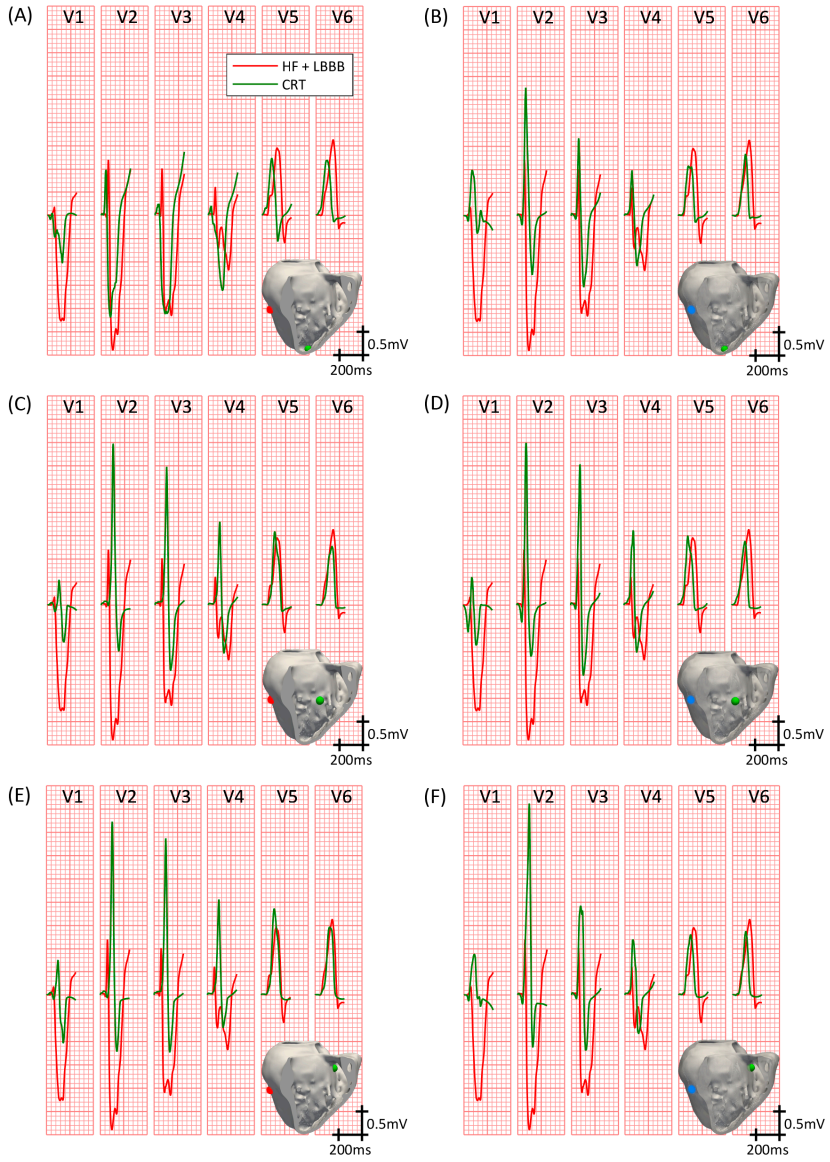

Figure 3.4 Precordial leads signals on CRT. QRS complexes in the precordial leads under HF + LBBB conditions, before (red trace) and after (green trace) the application of the best CRT configurations (shorter QRSd). Three different locations for the RV pacing lead were tested: RV apex with epicardial (A) and endocardial (B) LV lead stimulation; RV mid septum with epicardial (C) and endocardial (D) LV lead stimulation; and RV upper septum with epicardial (E) and endocardial (F) LV lead stimulation. Stimulation points are shown in light green inside the insets for the RV lead, and in blue and red for the LV endocardial and epicardial lead, respectively.

Secondly, we analyzed the effect of the delay between pacing leads and intrinsic activation in a fixed location. The best configurations for the RV lead placed in the apex are depicted in the first row. QRSd was reduced from 172 ms (Figure 3.4A) to 157 ms (Figure 3.4B), but bigger reductions were obtained for different intrinsic and pacing delays (AVD = 140 ms, VVD = 0 ms; AVD = 100 ms, VVD = 30 ms, respectively).

When the RV lead was located in the middle of the septum (second row), the QRSd was reduced from 161 ms (Figure 3.4C) to 146 ms (Figure 3.4D) for optimal configurations. In this case, these results were obtained for different pacing delays between leads but the same AVD (AVD = 140 ms and VVD = 30 ms vs AVD = 140 ms and VVD = 0 ms, respectively).

If the RV lead was placed in the upper septum, the QRSd was reduced from 149 ms (Figure 3.4E) to 143 ms (Figure 3.4F). However, in this case both configurations were achieved with the same intrinsic and biventricular delay (AVD = 140 ms, VVD = 30 ms).

Finally, the influence of LV epicardial versus endocardial pacing was assessed. QRSd was decreased in all cases after CRT application, but the reduction was greater for LV leads placed in the endocardium (column 2) compared to epicardium (column 1).

Summarizing, the optimal location in terms of shortest QRSd was obtained when the RV lead was placed in the upper septum and the LV lead was located in the mid posterior wall region. Once the optimal lead location was selected for both RV and LV leads, the shortest QRSd was measured for different intrinsic and biventricular delays, without highlighting a particular optimal setting. Finally, the shortest QRSd was obtained in all configurations when the LV lead was placed in the endocardium compared with those in the epicardium.

3.3.3 Ventricular activation time during CRT

Another helpful parameter to assess CRT outcome is the total activation time (TAT) of the ventricles. This parameter is not directly accessible in clinical practice during CRT procedures, but simulations can provide additional information to achieve the ideal configuration. Ideally, within normal physiological ranges, the shorter the QRS the shorter TAT, leading to an increase in ventricular synchrony. In Figure 3.5, the percentage of activated ventricular tissue is shown as a function of time for the healthy heart, under HF + LBBB conditions, and for the optimal CRT configurations (as a function of RV location), which are shown in Figure 3.4. Under HF + LBBB conditions (red trace), the electrical impulse spreads throughout the ventricles much slower (gradual slope) than in the healthy heart (black trace) or in CRT (green trace) configurations, completing ventricular activation after 210 ms. For CRT simulations, the rate of activated tissue was initially low, but increased rapidly to reach rates similar to those observed in healthy cases. This was especially noticeable when the LV lead was located in the epicardium (first column) and the RV lead was located in the mid and upper septum (Figure 3.5C, E, respectively). These results can be explained because of several factors. Firstly, the configuration of the PS and the PMJ distribution strongly affects the initial spread of the wavefront. Given the PS RV morphology, i.e. two main branches, one descending to the apex and another growing around the moderator band (Figure 3.1D), when the RV lead was located in the apex, the electrical stimulus entered fast in the PS (around 5 ms) and propagated to remote areas faster than through the myocardium (see Video 1 CRT). However, it took around 40 ms to retrogradely enter in the PS when the RV lead was located in the mid septal region, and around 90 ms when the RV lead was in the upper septum. For this reason, it took 75 ms to activate initially only 10% of the myocardium. Secondly, stimulation in the epicardial layer took longer to reach PMJ locations. Thirdly, the stimulation delay between both ventricles (VVD) also affected the initial slope of cardiac activation. Nevertheless, after 70 ms for the endocardial configurations (second column) and 125 ms for the

epicardial ones the percentage of activated tissue during CRT application was higher than the percentage of HF + LBBB conditions. Moreover, during the final phase of ventricular activation, the rising rate was considerably reduced. Indeed, the electrical impulse took between 26 to 54 ms (15% to 26% of the TAT) to activate the last 10% of the ventricular tissue.

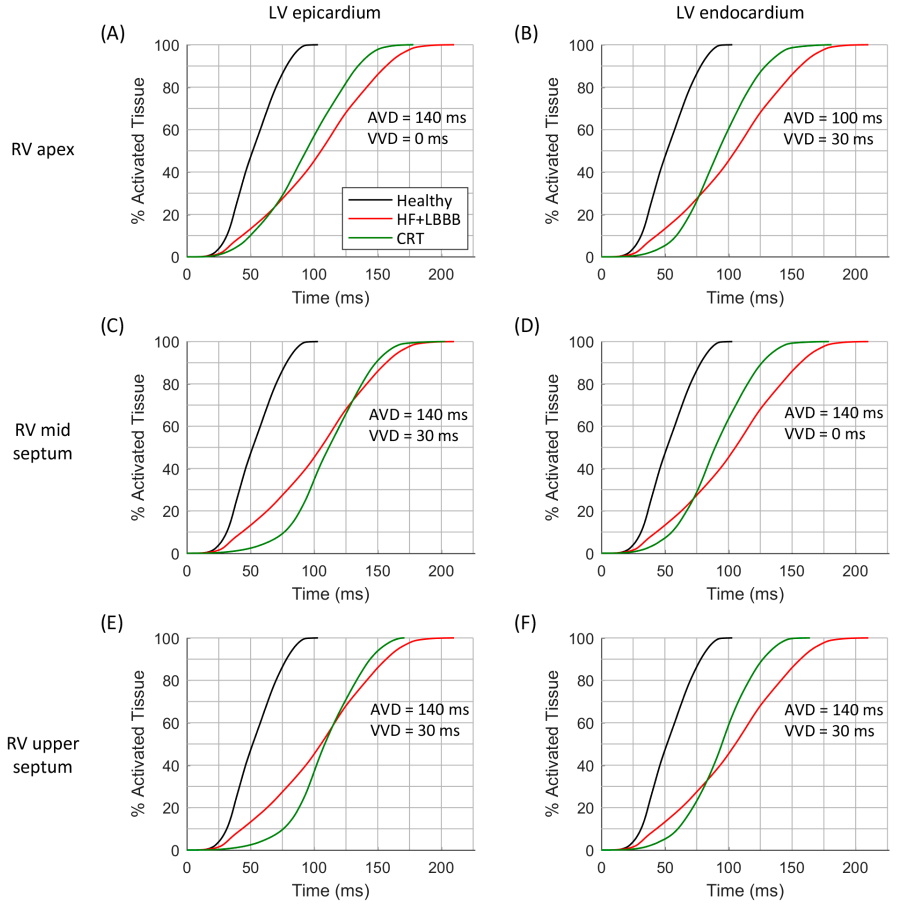

Figure 3.5 Cumulative frequency histograms of the normalized percentage of activated tissue. The curves correspond to healthy (black), HF + LBBB (red) and CRT (green) scenarios. The best CRT configurations (shortest QRSd) for the three locations of the RV lead were tested: RV apex with epicardial (A) and endocardial (B) LV lead stimulation; RV mid septum with epicardial (C) and endocardial (D) LV lead stimulation; and RV upper septum with epicardial (E) and endocardial (F) LV lead stimulation.

Finally, after applying the CRT protocol, the TAT was decreased by 15%, 14%, 12%, 15%, 19%, 22%, with respect to HF + LBBB conditions, as shown in Figure 3.5A–F, respectively. The locations of the pacing leads for the shorter QRS complexes coincided with the locations of the electrodes for the shorter TAT. However, when VVD and AVD were modified, the shortest QRS did not match the shortest TAT, which means that QRSd and TAT are not totally correlated. In addition, the difficulty in QRS measurement at the beginning and end of the signals has to be considered.

In clinical practice, a shorter QRSd is one of the standard criteria used to evaluate CRT response. However, both non-responder and responder patients show a reduction in QRSd after CRT application [187], [188]. Therefore, an additional indicator would be useful for a better perception of CRT benefit. As shown in Figure 3.5, TAT could be strongly modified by the initial rate of activation, as well as by the last activation interval. To avoid this, we analyzed the time elapsed to 90% of ventricular activation (t_{90}), (Figure 3.6). This parameter allows us to determine which configuration leads to a faster activation of most of the ventricular tissue, thus decreasing electrical dyssynchrony.

Figure 3.6 shows t_{90} values for a configuration with the RV lead placed in the apex, mid septum, and upper septum, and the LV lead located in the epicardium (panels A – C), and the same RV configurations with the LV located in the endocardium (panels D – F). The different delays applied between the His Bundle and CRT leads (AVD) and between the RV and LV leads (VVD) are shown in columns.

The optimal location of the LV pacing lead, both in the epicardium and endocardium, changed during CRT application for each of the pacing lead locations in the RV. However, the optimal AVD and VVD were the same in all cases, 140 ms and 0 ms (third column), respectively.

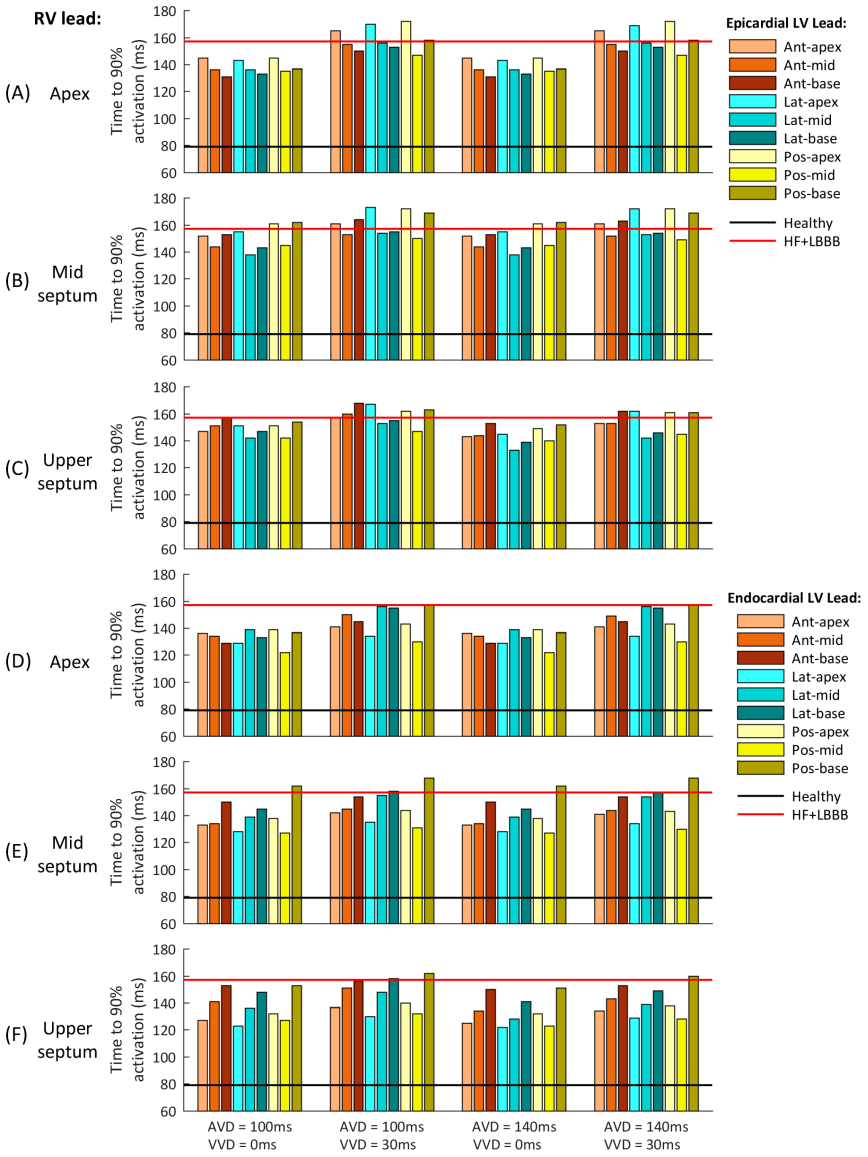

Figure 3.6 Time to 90% of ventricular activation for the different CRT configuration delays assessed. (A) – (C) Epicardial LV lead stimulation for the three RV lead location tested: (A) RV apex, (B) RV mid septum and (C) RV upper septum. (D) – (F) Endocardial LV lead stimulation for the three RV lead location tested: (D) RV apex, (E) RV mid septum and (F) RV upper septum. The three LV regions (anterior, lateral and posterior walls) are shown in different color brightness (red, blue and yellow). The values for healthy and HF + LBBB configurations are depicted in black and red lines respectively.

On the one hand, when AVD was modified (column 1 versus column 3 and column 2 versus column 4) similar results were obtained, except when the RV lead was located in the upper septum area. The electrical propagation of the intrinsic stimulus contributed to decrease t_{90} (7% reduction) for an AVD of 140 ms. On the other hand, when VVD was increased (column 1 versus column 2 and column 3 versus column 4) t_{90} increased up to 19% for all the RV lead locations.

When the RV lead was located in the apex, the optimal location of the LV lead in the epicardium was the LV anterior wall at basal level (Figure 3.6A). For the same RV lead location, the optimal LV lead location in the endocardium was the LV posterior wall at mid-cavity level (Figure 3.6D). Changing the RV lead location to mid septum, the optimal LV lead location in the epicardium was the LV mid lateral wall, while the optimal LV lead location in the endocardium was the LV mid posterior wall (Figure 3.6B, E, respectively).

Finally, for the RV lead location in the upper septum, the optimal placement of the LV pacing lead in the epicardium was in the LV mid lateral wall, while the optimal placement of the LV lead in the endocardium was the apex of the LV lateral wall (Figure 3.6C, F, respectively). Table 3.1 summarizes the optimal placement of the LV lead for a faster activation of 90% of the ventricular tissue. The optimal locations calculated are not in agreement with the optimal RV lead location determined based on a shorter QRSd in most cases. This result suggests the hypothesis that the shortest QRSd does not necessarily imply the fastest ventricular activation of 90% of the ventricular muscle.

3.3.4 Correlation between ventricular activation and QRS

To better highlight the relationship between QRSd and TAT, a correlation analysis was carried out (Figure 3.7A). Results showed an elliptical distribution of data with a moderate positive linear

relationship, statistically significant ($R = 0.78$ and $p < 0.05$). This moderate correlation could justify the difference between the optimal AVD and VVD values for the simulations with a shortest QRSd and with a shortest TAT.

LV epicardial stimulation				
Criterion	**RV lead**	**LV lead**	**AVD (ms)**	**VVD (ms)**
Shortest QRS duration	Apex	Posterior - mid	140	0
	Mid septum	Posterior - mid	140	30
	Upper septum	Posterior - mid	140	30
Shortest TAT	Apex	Posterior - mid	140	0
	Mid septum	Posterior - mid	140	0
	Upper septum	Posterior - mid	140	0
Faster activation of 90% of the ventricular tissue	Apex	Anterior - base	140	0
	Mid septum	Lateral - mid	140	0
	Upper septum	Lateral - mid	140	0
LV endocardial stimulation				
Criterion	**RV lead**	**LV lead**	**AVD (ms)**	**VVD (ms)**
Shortest QRS duration	Apex	Posterior - mid	100	30
	Mid septum	Posterior - mid	140	0
	Upper septum	Posterior - mid	140	30
Shortest TAT	Apex	Posterior - mid	140	0
	Mid septum	Posterior - mid	140	0
	Upper septum	Posterior - mid	140	0
Faster activation of 90% of the ventricular tissue	Apex	Posterior - mid	140	0
	Mid septum	Posterior - mid	140	0
	Upper septum	Lateral - apex	140	0

Table 3.1 Optimal placement of the LV lead on CRT.

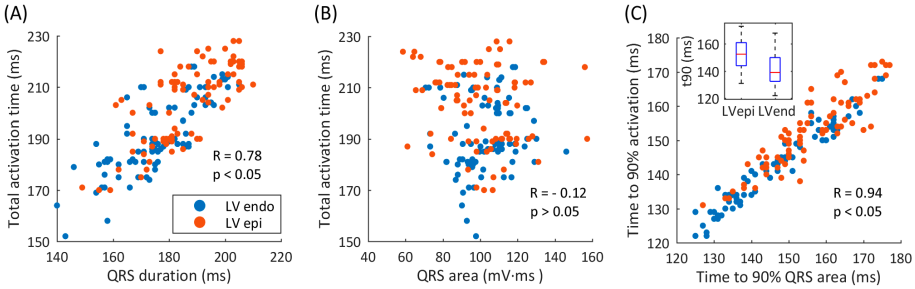

Figure 3.7 Correlation between ventricular activation and QRS. (A) Correlation between QRS duration and TAT (red circles show LV epicardial leads, blue circles show LV endocardial leads). (B) Correlation between the QRS area and TAT. (C) Correlation between t_{90}QRSa and t_{90}.

A similar correlation analysis was made between area of the QRS (QRSa) and TAT (Figure 3.7B). We first calculated the QRSa for the average signal of the six precordial leads, between the beginning and end values determined during the measurement of the QRSd. The results of the correlation show a scattering distribution of data with a statistically non-significant p value ($R = -0.12$ and $p = 0.076$). Thus, a linear relationship between QRSa and TAT was not observed in this study.

Finally, when correlating the curves of percentage of activated tissue and percentage of QRS area as a function of time, a direct relationship between both variables was observed. Figure 3.7C shows the correlation between time to 90% of QRSa (t_{90}QRSa) and time to 90% of the ventricular activation (t_{90}) for each CRT simulations. A significant correlation with a high linear dependence was observed ($R = 0.94$ and $P < 0.05$). Simulations with shorter t_{90}QRSa correspond to the simulations with shorter t_{90}. Therefore, a new biomarker based on time up to 90% of the QRS area can be used as an indicator of electrical synchrony.

3.4 Discussion

In this study, biophysical 3D multiscale simulations were conducted to assess alternative locations of the RV lead for a better CRT response in LBBB HF patients. The major findings of this study can be summarized as follows: i) the optimal leads location based on shortest QRS criterion was the RV upper septum and the LV mid posterior region minimizing also TAT; ii) for the optimal lead location, the delay configuration leading to the shortest QRSd was AVD = 140 ms, VVD = 30 ms. However, the AVD and VVD setting leading to the shortest TAT was different, suggesting that minimizing QRSd is a good criterion to select leads location but not to select the pacing delay; iii) the time to 90% of the QRS area (t_{90}QRSa) was a good predictor of the instant at which 90% of the ventricular tissue had been activated (t_{90}). This indicator could be used in clinical trials to complement QRSd criterion to select the optimal delay of the pacing leads to obtain a faster ventricular activation of most of the ventricular muscle.

3.4.1 Optimal lead location

The location of the optimal pacing site varies significantly between patients, so that a strategy of individualized LV lead placement is required to maximize the benefit of CRT [184], [189]. The apex for permanent LV pacing should be avoided, as this location has been associated with poor outcomes in studies such as MADIT-CRT [137], [190]. The experimental study PATH-CHF I suggested that the mid lateral left ventricular site for the LV lead may show greater acute benefit in patients with LBBB [191]. In general, a lateral or posterior vein is the desired location for achieving optimal hemodynamic support as this is usually the site of most delayed activation of the left ventricular wall in patients with LBBB [192], [193].

Our simulation results suggested the upper area of the RV septum as the optimal position for the RV lead, in agreement with some experimental [145], [194]–[196] and simulation [144] studies. The

study of Leclerq and coworkers [197] demonstrates that septal and apical RV pacing in CRT have a similar clinical outcome and similar LV reverse remodeling after 6 months of therapy. However, other studies [198] reported the shortest QRSd for RV septum pacing but not a better CRT response (similar LVEF at 6 months). This highlights the need of additional indicators to determine the optimal placement of the pacing leads.

In the present simulation study the most delayed activation area was located in the anterior basal LV region in the HF + LBBB configuration under intrinsic activation. We also assessed the latest activated area of the LV, when only RV stimulation was applied. If the RV lead was placed in the apex, the anterior basal LV area was activated the latest. However, the LV lateral wall was the latest activated area when the RV lead was located either in the middle or upper septal regions (see Figure A.3 in appendix A).

The study of Zanon and coworkers [140] determined that the LV lead location in the latest activated site was predictive of the maximum increase in contractility (LV dP/dt_{max}). On the other hand, in the recent study of Şipal and coworkers [141], comparing the clinical benefits of LV lead implantation guided by the shortest BiV-paced QRSd using surface ECG and with the standard unguided CRT, there was a significantly higher rate (85% vs. 50%, $p = 0.02$) of response (>15% reduction in LV end-systolic volume) to CRT as well as a shorter QRSd ($p < 0.001$) and a greater QRS shortening for the surface ECG guided group. Furthermore, the optimal site for LV lead placement was the posterior and posterolateral region, in agreement with our simulations. For all RV lead locations tested in our study, when the LV lead was placed in the latest activated area of the LV, none of those configurations led to the shortest QRSd.

In our study, we also showed that when pacing in the latest electrically activated area of the LV, that area did not provide the shortest TAT. Similar results were observed in the simulation study by

Pluijmert et al. [142]. In that work, the authors found that the LV pacing region that provided the maximum acute hemodynamic response, located near the latest activated area, did not lead to the largest reduction of TAT during biventricular stimulation. Even stimulating regions leading to the largest reduction of TAT showed poor increase of hemodynamic response. However, other studies have found a positive correlation between acute hemodynamic response and TAT reduction [135]. The optimal method to place the LV pacing lead is thus object of controversy: while several studies support that pacing in the latest activated area leads to better hemodynamic response, others consider the criterion of maximal reduction in QRSd as the best choice.

3.4.2 Optimal delay between pacing leads

Optimization of AVD and VVD is crucial during CRT application. A longer inter-lead electrical delay was associated with more pronounced LV reverse remodeling in CRT patients with a presumed optimal LV lead position concordant or adjacent to the latest mechanically activated non-scarred segment [199].

In clinical practice this value should be specifically set for each patient, although optimization is rarely performed in the real practice. The largest trials studying CRT used various methods to optimize these intervals, most frequently based on echocardiography and intracardiac electrogram interval measurement, but unequivocal proof of the benefit brought by optimization is still lacking [148]–[150]. Echocardiography presents inherent variability of results and is highly operator dependent [147]. Optimization based on intracardiac electrogram intervals has not proved yet to be of clear benefit above arbitrary AV interval [151]. Multisite pacing has shown favorable results, although it is technically complex [200]. A less time-consuming and easier optimization method might enable a more systematic optimization of the AVD and VVD at routine follow-up visits in all recipients of CRT systems.

The morphology of the PS clearly determined in our study the influence of AVD. When the RV lead was placed in the apex, the intrinsic activation of the His bundle found the majority of the Purkinje network already depolarized via retrograde conduction. However, if the RV lead was placed in the middle septum or closer to the outflow tract, further from any possible entrance to the cardiac conduction system, the intrinsic depolarization wavefront spread faster to the myocardium than the wavefront generated through the CRT leads, leading to a reduction in TAT. Some experimental studies [201] support the idea that PS may not allow retrograde conduction in LBBB patients due to structural damage, or if allowed, reduced conduction velocity would be observed in LV PS sections, neglecting the influence of PS. Whether the rest of the LV branches are able to conduct retrogradely [202] or other areas of the Purkinje network deteriorate, as HF evolves, remains unknown. Experimental studies have measured a strong reduction in septal conduction velocity during LBBB when HF was advanced compare to acute LBBB [203]. In that case, the simulation results of this study should be considered with caution. Although new methodologies are arising to better describe the PS [204], [205]. The lack of technology to characterize the PS in a patient specific manner, limits the optimal configuration for CRT.

Traditional CRT pacing mode does not promote ventricular activation through conduction system from the sinoatrial node. The lack of enough information on the chronic effects of the fusion leads (intrinsic stimulation combined with external pacing) and this method is avoided, setting the shortest AVD based on echocardiography [206]. In our study, a fusion between the intrinsic activation and biventricular (BiV) pacing for the optimal CRT configuration (pacing lead location and delays) was assessed. Several experimental works support this procedure [152], [207]–[209]. Guo et al. determined that congestive heart failure patients with BiV pacing + intrinsic activation presented improvement in cardiac function and quality of life [207]. Meanwhile, Vatasescu and coworkers observed that BiV pacing fused with intrinsic activation might increase the rate of structural responders [209].

Biophysical models of the heart have been used to optimize AVD, VVD and lead location during CRT simulation [136], [142]–[144], [210]. QRSd, estimated as the difference between the time of the first and last activated cardiac cell (or TAT), have been used as one optimization criterion by Miri and coworkers. In our study, the optimal LV lead location based on the shortest QRSd (calculated in the ECG signal) was similar to the region with shortest TAT (see Table 3.1). However, VVD value that produced the shortest QRSd did not match with the VVD that produced the shortest TAT, which means that QRSd and TAT are not totally correlated. A simulation study by Potse and coworkers [72] support this result. The authors observed that biventricular pacing did not change QRS duration but reduced total ventricular activation time when the LV stimulation was applied in one point of the LV free wall.

3.4.3 Indicators to evaluate CRT outcome

The Echocardiography Guided Cardiac Resynchronization Therapy (EchoCRT) study further reinforced the importance of QRSd over mechanical dyssynchrony as the most important indicator for CRT responses [211]. Other studies have proposed indexes based on QRS measurements. Van Gelder and colleagues [212] showed a relation between the Q-LV interval (the interval from Q wave to intrinsic deflection on the LV EGM) and the acute hemodynamic effect on optimized biventricular stimulation. A longer Q-LV interval predicted a greater increase in LV pressure rise ($LVdP/dt_{max}$) and vice versa. Normalizing the QLV by QRS duration, termed LV lead electrical delay (LVLED), was also shown to correlate with Doppler-derived dP/dt values. LVLED greater than or equal to 50 % was associated with significantly greater reductions in all-cause death or HF hospitalization at 12 months of follow-up in patients with non-ischemic cardiomyopathy [192].

Our simulations show that the difference in QRSd was significant when the LV was paced in different sites and for a fixed placement of RV. However, these differences in QRSd were decreased when adjusting the delay between leads in a fixed location for both leads (see Table A.1 in the appendix A). Thus, the shortest QRSd predicted precisely the region in the LV subdomains that produced the shortest TAT for the three locations of the RV lead tested, leading to an increase in ventricular synchrony. However, this index could not determine the pacing delay configuration between leads that allows to obtain the shortest TAT. There is no consensus on how QRS should be accurately measured, and therefore small differences are expected between methods [213]. In our study, the optimal QRSd obtained after CRT application supposed a 20% reduction of the QRSd. This result is in agreement with the study of Elhakam et al. [187], where 180 patients under heart failure conditions and LBBB were studied, and similar reductions were obtained. Other studies obtained lower QRS reduction values, namely 17% and 12%, for CRT responders in Molhoek et al. [188] and Pitzalis et al. [214] studies, respectively.

The assessment of interventricular dyssynchrony was done analyzing the TAT. Our results showed that a shorter duration of the QRS complex is moderately correlated with a shorter TAT (Figure 3.7A). The narrowest QRS complex predicted the optimal location of the stimulation leads but not the optimal value of the VVD. In this way, the t_{90} index selected correctly the best delay configuration to provide the fastest activation of the majority of the heart. In several configurations, TAT value was exactly the same (see Table A.2 in the appendix A), but t_{90} discerned the shortest order of activation. Thus, the shortest QRSd predicted the location for the optimal leads placement, but t_{90} predicted the best pacing delay with the shortest TAT. We hypothesized that setting the pacing delay properly with this new index could improve CRT non-responders rate.

Other simulation studies have assessed the evolution of TAT during CRT [72], [215] focused on the assessment of the LV intraventricular

delay. The recent study of Tomassoni [216] showed how CRT response assessment is highly variable depending on the criteria used to define the response. QRS width has been shown to correlate well with interventricular dyssynchrony but unfortunately this has poor accuracy for detecting intraventricular dyssynchrony. As a result, it is estimated that only 70% of patients with LBBB have echocardiographic evidence of mechanical dyssynchrony [74]. The role of mechanical dyssynchrony for improving patient selection for CRT remains controversial. The multicenter, nonrandomized Predictors of Response to CRT (PROSPECT) study evaluated the ability of 12 echocardiographic indices of dyssynchrony to predict CRT responses at 6 months [217]. These indices provided only modest sensitivity and specificity, and researchers reported large variability in quantification of dyssynchrony. Mechanical dyssynchrony has also been used to select CRT candidates with a narrow QRS duration ≤ 120 ms, with limited success in randomized multicenter studies. In this line, mechanical response generated by electrical excitation (excitation-contraction coupling) could be different depending on the heart region [218]. Multiple simulation studies have addressed CRT from different perspectives. The recent work of Lee et al. [219] organized and summarized the state of the art of computational modeling for CRT.

To our knowledge, and given the benefits of using a model where all variables are accessible, our study is the first to systematically explore the correlation between the activated portion of tissue (less accessible in clinical practice) and the QRS complex in the torso surface. Thus, we found that an index based on time to 90% of the QRS area (t_{90}QRSa) is a good predictor of the instant at which 90% of the ventricular tissue has been activated (t_{90}). This indicator could be used in clinical trials to complement QRSd measurements in defining the optimal location and delay of the pacing leads to produce faster ventricular activation of most of the ventricular muscle.

3.4.4 Epicardial vs endocardial pacing

Although LV epicardial stimulation decreased QRS width in most cases, a greater reduction was observed for endocardial pacing. The study conducted by Spragg et al. [184] showed that CRT administered at the optimal site of the LV endocardium was more effective than stimulation through an electrode in the coronary sinus. There is evidence to suggest that endocardial stimulation yields to more natural transmural activation patterns and a better response for CRT patients [220]–[222]. In this line, new devices that allow endocardial pacing and single lead stimulation [223] coordinated with intrinsic activation will provide new possibilities.

The better results obtained with endocardial pacing are strongly influenced by PS. As PMJs are located in the endocardial surface, the wavefront generated for the LV lead gets into the Purkinje conduction system retrogradely and spreads faster to other inactivated areas (see Video 2 Retrograde). Thus, knowing the distribution and location of PMJ, as well as the conduction system morphology is a determinant factor for CRT improvement.

3.5 Limitations

CRT was analyzed only from an electrical point of view in our study. Mechanical behavior based on echocardiography is a common alternative to assess hemodynamic response, although this method is time-consuming and the optimal measurements remain unclear. Simulation studies including the mechanical behavior would be certainly enlightening.

In this study, a particular heart geometry and PS were assessed. The inclusion or not of the moderator band (which may be very patient-specific) may affect QRSd and TAT measurements, especially when pacing on the RV upper septal area. Although our results have been compared to other related studies, the specific findings observed in this

study should be carefully validated against clinical studies and complemented with a set of computational models of different patients. In addition, two isolated stimuli were employed to assess CRT efficiency. The development of strategies that allow multi-site pacing should be taken into account in future studies. Additionally, the incorporation of levels of HF in different ventricular areas could modify simulation results.

CHAPTER 4

Analysis of vulnerability to reentry in acute myocardial ischemia using a realistic human heart model

4.1 Introduction

Electrophysiological heterogeneities in the myocardium caused by acute ischemia can lead to potentially lethal arrhythmias, such as ventricular tachycardia (VT) and ventricular fibrillation (VF) [224]. Indeed, within the first 10 to 15 minutes after a coronary artery occlusion and the subsequent lack of blood flow, the patient frequently suffers sudden cardiac death due to the appearance of arrhythmias [225].

Experimental evidence has shown that two discrete phases of ventricular arrhythmias occur within the first 30 minutes of myocardial ischemia [24], [91]. Phase 1A takes place between 2 and 10 min of ischemia approximately [91], with a reentrant process as predominant mechanism of origin. VT is the most common arrhythmia in this stage [92], [94]. Phase 1B occurs within 18 – 30 min after artery occlusion

[91], although the main mechanisms for triggering arrhythmias are not precisely defined [94], [95]. A great number of VF events and larger mortality have been reported during this stage [96], [97]. However, the overall incidence of arrhythmias is higher during phase 1A [97].

Electrophysiological changes at the cellular and intercellular levels occur during acute myocardial ischemia and predispose the heart to the occurrence of arrhythmias [112]. It is well know that the three main ischemic components that induce electrophysiological alterations in the affected tissue are hyperkalemia, hypoxia, and acidosis [25], [26]. Within the acute phase of ischemia, hyperkalemia (i.e., an increase of extracellular potassium concentration, $[K^+]_o$) generally reduces conduction velocity (CV) and cell excitability, and induces post-repolarization refractoriness [90], [112]. Hypoxia (i.e., a reduction in oxygen supply) shortens the action potential duration (APD) [101], [118], while acidosis (i.e., a reduction of pH) affects the behavior of certain ionic currents [105], [226]. All these alterations occur in a heterogeneous way through the myocardium, providing the pro-arrhythmic substrate for the occurrence of reentrant arrhythmias [90].

The influence of the main ischemic components in arrhythmogenesis has been investigated in the past. However, due to the complex process of acute myocardial ischemia, the relative contributions of each component are still not completely established. Experimental and simulation studies have analyzed the combined effect of hyperkalemia, hypoxia, and acidosis [25], [227]–[229], as well as the effect of one component at a time during the generation of arrhythmias [25], [34], [230]. Although some researchers have suggested the existence of a predominant ischemic component favoring the likelihood of arrhythmias [227], [228], [231], there are no works that have assessed and compared the individual influence of the three components simultaneously using a realistic 3D anatomical model during ischemia. A 2D simulation study by Trenor et al. [228] evaluated the individual effect of these components. However, a realistic ischemic region and His-Purkinje system (HPS) were not included in their work.

The role of the HPS as a possible element that favors the onset and maintenance of ventricular arrhythmias also needs further investigation. Experimental recordings of the HPS electrical activity have provided some evidence supporting the implication of the HPS in VF. For instance, experiments in canines showed retrograde and anterograde propagation between the myocardium and the HPS during VF [232]. In another study, endocardial cryoablation in pig hearts modified the activation pattern of VF [233]. Finally, a faster extinction of VF was observed in dogs after chemical ablation of Purkinje fibers [234]. Despite all these evidences results in animals do not always translate to human due to differences between species. In addition, the acquisition techniques of these studies may be not sufficient to measure the HPS electrical activity without recording the surrounding activity. Therefore, the role of the HPS in the onset and maintenance of ventricular arrhythmias is controversial, and complex to assess experimentally in humans.

Computational simulations are a useful and complementary tool to analyze ischemia-induced arrhythmias and the role of the HPS. Several simulation studies have assessed the likelihood of arrhythmias within the first minutes of acute ischemia by the quantification of the vulnerable window (VW) [34], [122], [228], [229]. The VW is defined as time interval during which ectopic stimuli can elicit a reentry. However, there are few ischemic simulation studies that include a detailed HPS [235], [236], and also a realistic ischemic region in a human ventricular model [237].

In this work, we investigate the effects of hyperkalemia, hypoxia, and acidosis on the VW to reentry during different ischemic scenarios involving different severities of ischemia. In addition, we analyze the role of the HPS and its mechanisms of action in the generation and propagation of reentrant activity. These studies were carried out using a 3D biventricular human model that includes a realistic geometry of the ischemic central and border zones, as well as the cardiac conduction system.

4.2 Methods

4.2.1 Anatomical model

In the present study, we used a 3D anatomical model of the ventricles including a realistic geometry of the ischemic region previously developed by our group [238]. The biventricular model was built from manual segmentation of a DE-MRI stack using Seg3D software (Scientific Computing and Imaging Institute, University of Utah, USA) [155]. A surface model of the ventricles was generated from the segmented images and meshed using MeshGems-Hexa (Distene S.A.S., Bruyeres-le-Chatel, France), obtaining a volume mesh formed of 4 million nodes (vertices) and 3.71 million hexahedral elements, with an average edge length of 0.4mm. Transmural heterogeneity of the ventricular myocardium was assigned in the model by defining endocardial, mid-myocardial and epicardial zones, which were adjusted to 17%, 41%, and 42% of the ventricular wall thickness, respectively [156]–[158]. Myocardial anisotropy was implemented by defining fiber orientation based on the method by Streeter et al. [159].

The biventricular model was based on cardiac DE-MRI images from a patient that revealed ischemic myocardial regions in the LV. Using the American Heart Association (AHA) nomenclature, these regions were located in the medial and basal segments of both inferolateral and inferoseptal walls (segments 3, 5, 9, and 11), and all segments of the inferior wall (apical, mid-cavity, and basal) (segments 4, 10, and 15), mainly associated with an occlusion of the right coronary artery (RCA) [239]. The 3D geometries of the ischemic central zone (ICZ) and the border zone (BZ) were obtained by applying the standard deviation (SD) method [240] during the segmentation of the DE-MRI stack. Briefly, the myocardium was divided into healthy and ischemic regions based on the gray color intensity of each pixel. Similarly, the ischemic region was categorized as ICZ or BZ. ICZ was assigned for pixel intensities higher than mean value + 3×SD of healthy tissue; BZ for

pixel intensities between mean + 2×SD and mean + 3×SD values; and healthy tissue (or normal zone (NZ)) for pixel intensities below mean + 2×SD. The different regions were mapped into the volume mesh of the ventricles and each hexahedral element was labeled as ICZ, BZ or NZ (Figure 4.1A). For further details regarding the biventricular model construction, see [238].

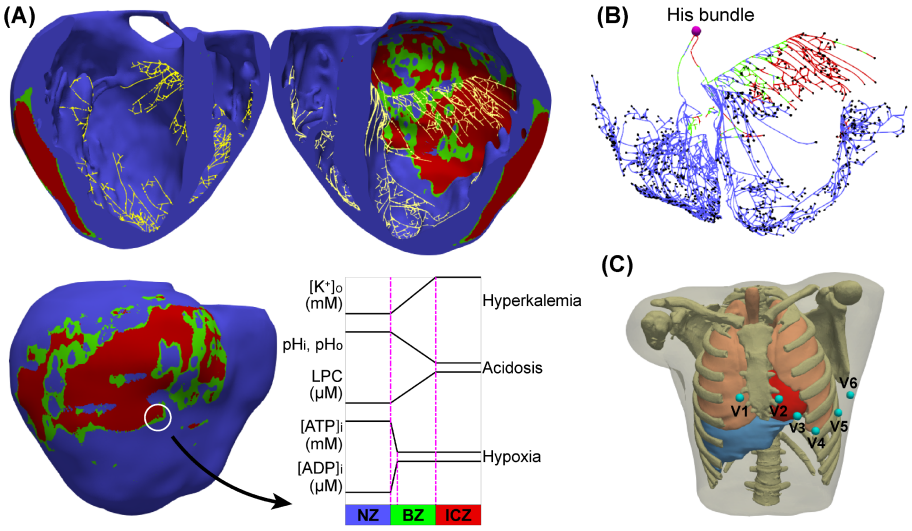

Figure 4.1 Anatomical model. (A) Endocardial (upper) and epicardial (lower) views of the biventricular model in acute ischemia. The ischemic central zone (ICZ) (red), the border zone (BZ) (green), the normal zone (NZ) (blue), the His-Purkinje system (HPS) (yellow), and the spatial variations of $[K^+]_o$, $[ATP]_i$, $[ADP]_i$, pH_i, pH_o, and LPC across the different zones are shown. (B) HPS with its elements labeled as ICZ (red), BZ (green), and NZ (blue). Purkinje-Muscle junctions are represented as small brown spheres. (C) Torso model, including the biventricular mesh (red) and the precordial leads location.

The HPS network used in our simulations was the same network developed in our previous work [241]. It was built based on a stochastic growth method [162] using linear elements. The right ventricle (RV) and left ventricle (LV) sections of the network comprised two and three main branches with several subdivisions, respectively. A total of 1391 Purkinje-Muscle junctions (PMJs) were distributed across the

myocardium, which, upon simulation, yielded a typical ECG wave morphology in the precordial leads. Furthermore, we adjusted the conductivity of the PMJs so as to allow retrograde and anterograde electrical propagation as it has been experimentally observed [242]. Finally, each HPS element was labeled as NZ, ICZ or BZ depending on its location (Figure 4.1B).

To compute the ECG in the precordial leads, we fitted the biventricular model into a torso mesh previously developed [163], using a linear transformation. The adjusted torso mesh comprised 1.26 million nodes and 7.35 million tetrahedral elements, with a spatial resolution of 0.55mm (Figure 4.1C). Furthermore, tissue conductivities of lungs, liver, bones, blood pools, great vessels, and skeletal muscle were included in the torso model. For further detailed information, see [238].

4.2.2 Action potential model in acute ischemia

As the basal model for our simulations, we used a modified version of the O'Hara action potential (AP) model [37] and we introduced it into our 3D biventricular model as in our previous work [241]. To include changes related to acute ischemia (hyperkalemia, hypoxia, and acidosis) in the model, we modified several currents and incorporated others, as in [243].

The effect of intracellular ATP ($[ATP]_i$) and ADP ($[ADP]_i$) (and their changes due to hypoxia) were introduced in the AP model through the following changes. First, we added the ATP-sensitive K^+ current ($I_{K(ATP)}$) proposed by Ferrero et al. [118] which was adapted to human ventricular myocytes by modifying the maximum conductance and the sensitivity to $[ATP]_i$ and $[ADP]_i$ using data from Babenko et al. [244]. Second, we introduced different scaling factors in the formulations of the Na^+/K^+, sarcolemmal Ca^{2+} and SERCA pumps that depend on $[ATP]_i$ and $[ADP]_i$ as in the model proposed by Cortassa et al. [245]. To introduce the effects of acidosis in the model, we modified the

inactivation (f_{ss}) and activation (d_{ss}) gates of the L-type Ca^{2+} current (I_{CaL}) and multiplied the maximum conductance by a scaling factor to mimic the experimental results observed by Saegusa et al. [105]. Furthermore, we multiplied the fast and late Na^+ currents (I_{Na} and I_{NaL}, respectively) and the Na^+/K^+ pump by different scaling factors that depend on extracellular and intracellular pH (pH_o and pH_i, respectively), and lysophosphatidylcholine (LPC). The effects of pH_o and pH_i were obtained from [104], [246]–[248], while those due to LPC were obtained from [249]–[251]. Finally, the effect of hyperkalemia was introduced by simply increasing the extracellular potassium concentration ($[K^+]_o$).

The values of $[K^+]_o$, $[ATP]_i$, $[ADP]_i$, pH_i, pH_o, and LPC used in the AP model were chosen in correspondence to four different severities of acute ischemia in the ICZ: mild (≈ 2.5 minutes after occlusion), moderate (≈ 5 minutes after occlusion), moderate-severe (≈ 7.5 minutes after occlusion), and severe (≈ 10 minutes after occlusion) (see Figure 4.2). The values for healthy and severe conditions were taken within a range of experimental data [98], [101], [103], [108], [249], [252]. Parameter values for mild, moderate, and moderate-severe conditions were calculated using linear interpolation, except for $[K^+]_o$. For the latter, we used a Boltzmann curve which approximately mimics the behavior of the $[K^+]_o$ during the first 10-15 minutes of ischemia in accordance with several experimental studies [98], [103], [253], [254] (Figure 4.2).

Within the BZ, we implemented a linear gradient of each ischemic-related parameter from its physiological value in the NZ to its ischemic value in the ICZ, as shown in experimental studies [28], [255]. The transition within the BZ occurred along its entire width for $[K^+]_o$, pH_i, pH_o, and LPC and along the proximal 10% of the BZ (next to the NZ) for $[ATP]_i$ and $[ADP]_i$ (see Figure 4.1A, bottom panel).

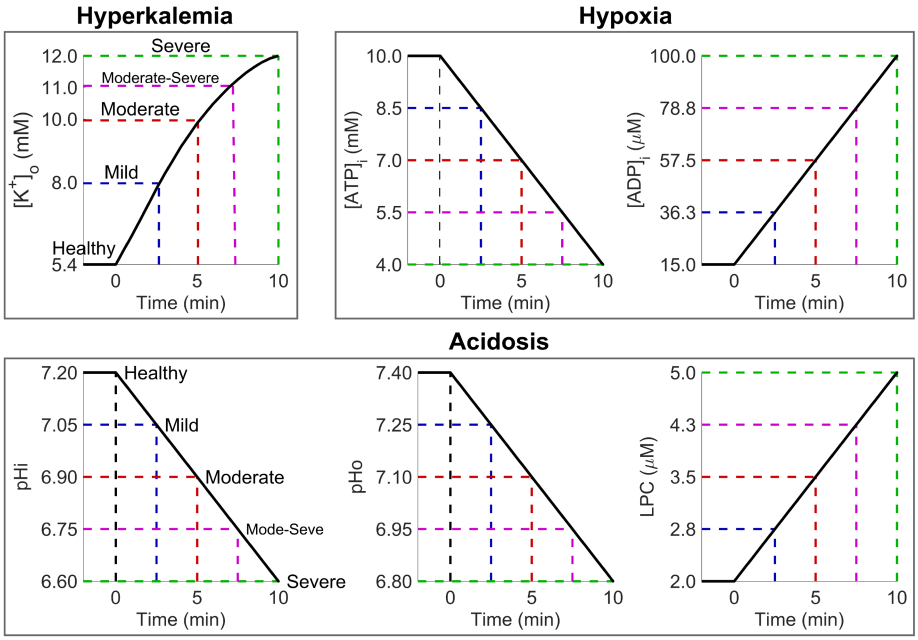

Figure 4.2 Time course of ischemia-related parameters during the first 10 minutes of acute ischemia. Parameter values before arterial occlusion (t = 0) correspond to healthy conditions. Parameter values for 2.5, 5.0, 7.5, and 10.0 minutes of ischemia correspond to a mild (blue traces), moderate (red traces), moderate-severe (magenta traces), and severe (green traces) ischemic condition, respectively.

Ischemic simulations including the HPS were performed using the AP model of Purkinje cells developed by Stewart et al. [169]. The effects of hyperkalemia on Purkinje cells were introduced in the model by simply increasing extracellular potassium concentration ($[K^+]_o$) as in the nearest cardiomyocyte. The effects of hypoxia and acidosis were not introduced due the lack of experimental information.

4.2.3 Stimulation protocol

In the present study, we analyzed the role of each ischemic component (hyperkalemia, hypoxia, and acidosis), as well as the role of the His-Purkinje system, in the generation of reentries. For this purpose, our 3D human ventricular model with and without the HPS was used to

simulate the bioelectric behavior of the ventricles under different acute ischemic conditions. In the presence of the HPS, sinus rhythm was simulated by applying an electrical stimulus (S1) in the hypothetical location where the bundle of His begins. Conversely, when the HPS was removed from the model, a stimulus was applied at each location of a PMJ at the same instant in which the PMJ was activated in the simulation with the HPS. Seven consecutive beats with a cycle length of 600 ms were simulated in both cases. After the fifth beat of the series, a premature stimulus (S2) was applied in a region of the epicardial BZ. This stimulus mimics the earliest epicardial activity experimentally observed in the myocardium adjacent to the border zone after a premature beat occurred in acute ischemia [129]. The time interval between the fifth S1 and S2 (coupling interval or CI) was varied with a resolution of 5 ms to determine the duration of the vulnerable window (VW) for reentry. The range of CIs that produced at least two reentrant cycles in the biventricular model was defined as the VW.

4.2.4 Numerical methods

Simulations were run using ELVIRA software [170]. The electrical propagation throughout the ventricles was computed by solving the reaction-diffusion monodomain equation

$$\nabla\cdot(\mathbf{D}\nabla V_{\mathrm{m}}) = C_{\mathrm{m}}\frac{\partial V_{\mathrm{m}}}{\partial t} + I_{\mathrm{ion}} + I_{\mathrm{stim}} \tag{4.1}$$

where $\boldsymbol{D}$ is the equivalent conductivity tensor, V_{m} is transmembrane potential, C_{m} is membrane capacitance, I_{ion} is transmembrane ionic current and I_{stim} is the transmembrane stimulation current. This system of differential equations that results from equation 4.1 plus the ordinary differential equations related to gating and dynamic changes in ionic concentrations [170] was solved using the finite element method (FEM).

To obtain a realistic conduction velocity (CV) in the biventricular model, we performed a set of test simulations on a 3D slab model of 20

mm x 20 mm x 8 mm as in our previous study [241]. The longitudinal (σ_L) and transversal (σ_T) conductivities were fit to 0.5 S/m and 0.1 S/m, respectively. This calibration yielded a CV of 0.61 m/s along the fiber direction and of 0.29 m/s perpendicular to the fiber direction, in accordance with experimental measurements in human ventricles [48]. For the HPS, the CV was adjusted to 2.5 m/s approximately [47], [256].

The ECG and the body surface potential maps (BSMP) were obtained using an approximation of the bidomain approach. Specifically, the transmembrane potentials computed in the nodes of the hexahedral biventricular mesh were interpolated to the nodes of the tetrahedral torso mesh that corresponded to the ventricular myocardium. Then, the extracellular potentials (φ_e) in the ventricles were calculated by solving the passive term of the bidomain approach

$$\nabla\cdot\left([D_i+D_e]\nabla\varphi_e\right)=-\nabla\cdot(D_i\nabla V_m) \tag{4.2}$$

where $\boldsymbol{D}_i$ and $\boldsymbol{D}_e$ are the volume-averaged conductivity tensors of the intra and extracellular domains, respectively [171], [174]. Subsequently, applying Dirichlet boundary conditions at the ventricles-torso interface and Neumann-type conditions at the torso surface, the extracellular potentials were computed in the whole domain of the 3D torso model (Ω_T) by using the FEM method to solve the following Laplace equation:

$$\nabla\cdot(\boldsymbol{D}_T\cdot\nabla V_T)=0 \quad \text{in} \quad \Omega_T \tag{4.3}$$

where V_T represents extracellular potentials within the domain of the torso model (except for the ventricles) and $\boldsymbol{D}_T$ is the heterogeneous conductivity tensor of the torso model defining its conductive properties [238]. We assigned isotropic conductivities to each tissue (see [241] for details). Finally, the ECG in each precordial lead was computed as the extracellular potential at the electrode location referred to the Wilson Central Terminal, as done in the clinical practice. The total activation time (TAT) of the ventricular mesh was estimated as the

time interval between the first and last depolarized node in the mesh above a threshold of −10mV.

4.3 Results

4.3.1 Changes in electrical activation and ECG under different severities of acute ischemia

Figure 4.3A shows ventricular activation maps under healthy conditions and under three different severities of acute ischemia. In non-pathological conditions, endocardial activation of the LV started 18 ms after the His stimulation, and 9 ms later the RV activation began. This results are similar to those obtained by Durrer et al. in human hearts [47]. The total activation time (TAT) of the ventricles was approximately 100 ms, comparable to [47], [181]. The last activated part in the LV was the antero-lateral region, while the latest areas depolarized in the RV were the outflow tract and postero-basal regions.

Under ischemic conditions, the electrical conduction in the sections of the His-Purkinje system located in the ischemic region was slower. This reduction in the propagation velocity led to a delay in the onset of ventricular activation. Accordingly, when mild ischemia was simulated, the LV and RV activation started at 26 ms and 30 ms, respectively. During moderate ischemia conditions, the electrical impulse from the His bundle arrived first to the RV endocardium at 34 ms, while the LV activation started 7 ms after the onset of RV activation. In severe ischemia, the first activation in the RV and LV occurred at 40 ms and 69 ms, respectively. Furthermore, a wavefront from the RV reached the LV endocardium in the apical septal region at 74 ms, which depolarized the apex and the endocardial lateral wall through myocardial propagation and retrograde conduction through the HPS. In this last case, an incomplete left bundle branch block (LBBB) was observed.

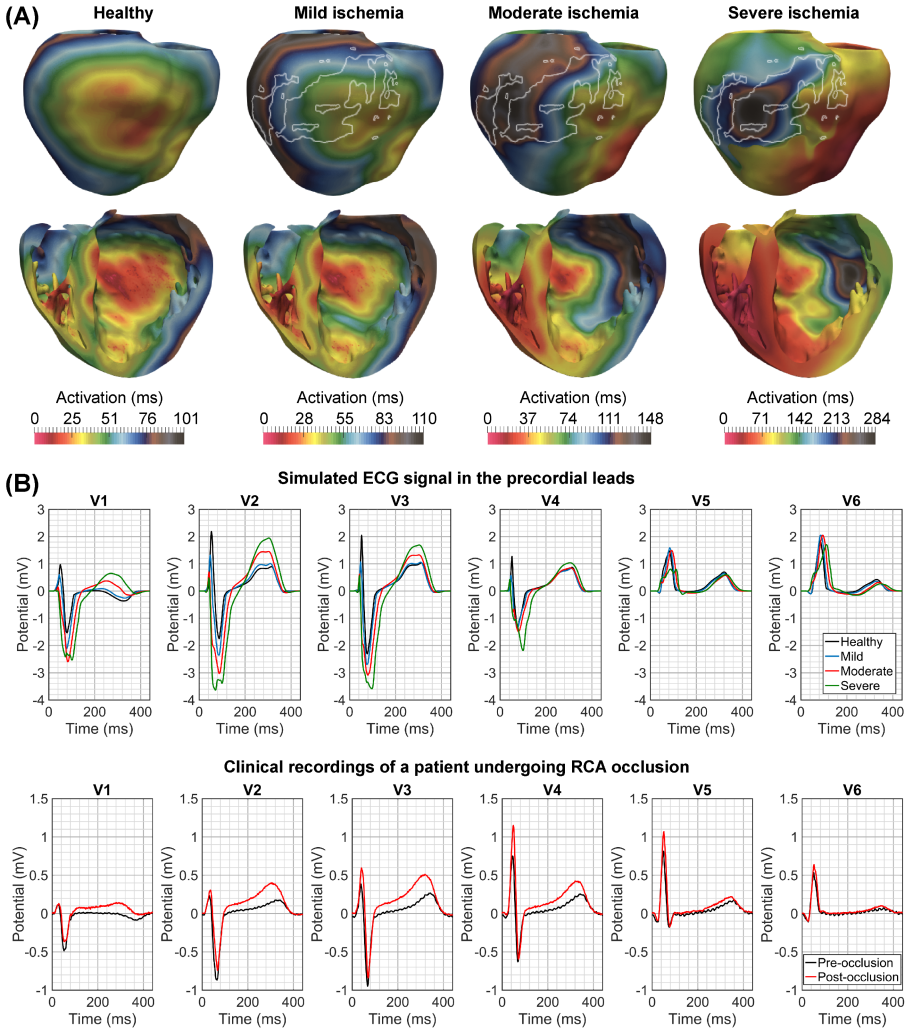

Figure 4.3 Simulated myocardial activation maps and ECG signals under different ischemic severities. (A) Posterior view (top row) and anterior cross-sectional view (bottom row) of the biventricular model showing the activation on the epicardium (upper) and endocardium and midmyocardium (lower), respectively. White curves represent the ischemic central zone. (B) Comparison between simulated precordial lead signals (top row) and clinical recordings of a patient before and 3 minutes after an RCA occlusion (bottom row). Patient data were taken from the STAFF III database of the Physionet repository [257].

Similarly, a reduced conduction velocity in the ischemic region led to a progressive increase in the TAT and a change in the latest activated area. In mild ischemic conditions, the activation of the whole myocardium took 110 ms. The last activated areas in the RV were the same regions than in healthy conditions. However, the latest area depolarized in the LV was shifted slightly to the lateral region. During moderate ischemic conditions, the TAT was increased to 148 ms and the latest activated region in the LV was the postero-lateral wall next to the ICZ. Under severe ischemic simulations, a marked increase in the TAT to 248 ms was obtained. In addition, the ICZ was the latest activated region, although in healthy conditions this region was one of the first parts of the LV epicardial wall to be activated.

Figure 4.3B shows a comparison between the computed ECG in the precordial leads for simulations in a healthy heart and under three different severities of acute ischemia (top panel), and clinical recordings of a patient before and 3 minutes after an RCA occlusion (bottom panel). Data were taken from the Physionet repository (https://physionet.org/), STAFF III database, patient 8 [257], [258]. In non-pathological conditions, the duration of the QRS complex (QRSd) was approximately 90 ms, in accordance with human data [56], [57]. Under ischemic conditions, the QRSd was increased to 98, 121, and, 133 ms for mild, moderate, and severe ischemia, respectively. This last value supports the diagnosis of an incomplete LBBB, caused by a reduced conduction velocity in the main branches of the His-Purkinje system probably due to the severe level of ischemia.

Several changes in the T-wave morphology of the precordial leads were observed during ischemic simulations. Our results show an increment in the T-wave amplitude, especially in leads V2 and V3, similarly to the clinical record of the example patient after RCA occlusion (red trace), as recorded as well in clinical practice [119]. In addition, a transition of the T-wave in lead V1 from negative in healthy conditions to a biphasic behavior during moderate ischemia (≈ 5 min after the onset of ischemia) was found, which agrees with the clinical

recording 3 minutes after RCA occlusion (red trace). This finding is considered very specific of ischemia [119], [121]. For severe ischemic conditions, an inverted T-wave was obtained in lead V1, in accordance with experimental data [119].

Finally, an elevation of the ST segment in leads V1–V3 was measured at the J point (end of the QRS complex) for a moderate ischemic condition (8, 110, and 100 μV, respectively). This alteration was also observed in the clinical ECG, although in a different degree (71, 81, and 70 μV). Conversely, the simulated ECG under severe ischemia displayed a marked ST depression of –426, –573, and –457 μV in leads V1–V3 compared to non-pathological tissue. This depression represents the combined effect of acute ischemia and LBBB, which is in accordance with the second criterion of Sgarbossa (ST segment depression ≥ 1 mm in V1, V2, and/or V3) for the diagnosis of a patient with these two pathologies [259], [260].

4.3.2 Effect of acute ischemia in the action potential

Figure 4.4 shows the alterations in APD and resting membrane potential (RMP) during mild, moderate, and severe acute ischemia. As shown in Figure 4.4A, simulations under ischemic conditions produced APD shortening, a reported effect in patients with this pathology [114]. In healthy conditions, the APD values ranged 232 – 347ms, depending on the location within the ventricles. The longest APDs were found in PMJ sites on the endocardial wall, whereas the shortest APDs were found in sites close to the latest electrically activated area on the epicardium wall, which is in accordance with experimental observations [236], [261], [262].

Under pathological conditions, the longest APDs remained localized at the functional PMJs, which is in accordance with [236], whereas the shortest APDs were found in the ischemic region. Under mild, moderate, and severe ischemia, APD was reduced by a maximum of 18%, 27%, and 49% of the normal values, which agrees with [114].

Furthermore, the degree of APD shortening varied spatially throughout the ischemic tissue, as reported in other studies [263]. This spatial heterogeneity was greater during severe ischemia. Co-existing areas were found inside the ICZ with and without APD reduction (ΔAPD = 45% and ΔAPD = 0%, respectively) (Figure 4.4A, green circle). To investigate the differences in APDs in this region, we analyzed the propagation patterns. Our results show that a wavefront entering the ICZ from its right side was able to stimulate the proximal ICZ, maintaining the peak potential and avoiding APD reduction in the region. However, the central section of the ICZ was stimulated by several wavefronts of reduced amplitude that led to APD shortening.

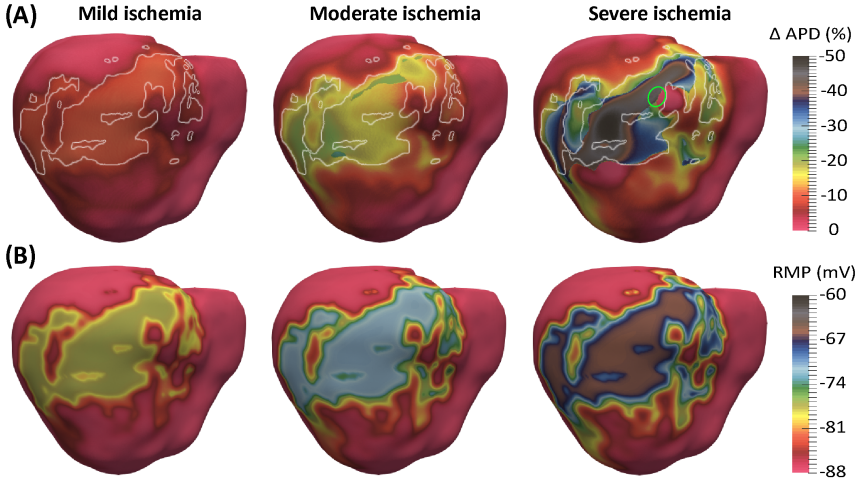

Figure 4.4 Electrophysiological changes in the action potential under acute ischemia. Simulated maps of action potential duration (APD) variation (A) and resting membrane potential (RMP) (B) under mild, moderate, and severe ischemia conditions. The white curves represent the ischemic central zone (ICZ), while the green circle shows the epicardial region within the ICZ where spatial heterogeneity was greater.

Similarly, our results (Figure 4.4B) show a less negative RMP under acute ischemia conditions, as in previous experimental and simulation studies [168], [228], [264]. In non-pathological tissue, the RMP was approximately –88mV, while in the ICZ RMP was –73mV, –68mV, and –63mV for mild, moderate, and severe ischemia, respectively. In

the BZ, resting potentials values varied between the healthy and ischemic values.

4.3.3 Role of acute ischemia in the generation of reentries

In order to assess the effect of the degree of ischemia in the generation of reentry, the vulnerable window during each ischemic condition was calculated by applying a premature stimulus (S2) in an area of the border zone in the epicardial wall (point P1 in Figure 4.5), as explained in the Methods section. S2 was delivered at different time intervals (coupling intervals) after the fifth sinus (S1) beat. Figure 4.5A shows the VW obtained during four different ischemic severities: mild, moderate, moderate-severe, and severe. Our results predict a VW of approximately 5 ms in moderate ischemic conditions, corresponding to a CI between 335 and 340 ms. A change in the ischemic severity to a moderate-severe condition yielded the maximum width of the VW (45 ms), with a range of CIs between 345 and 390 ms. Conversely, no reentries were found from mild or severe conditions. In summary, our results suggest that the ischemic severity plays an important role in the generation of reentries. A unimodal behavior of the VW during the first 10 minutes of ischemia was observed. In other words, a premature stimulus applied only in a moderate (≈ 5 minutes after occlusion) or moderate-severe level (≈ 7.5 minutes after occlusion) of acute ischemia could generate a reentry.

To evaluate the effects of each ischemic component (hyperkalemia, hypoxia, and acidosis) on the generation of reentries, we quantified the VW during seven different scenarios of acute ischemia in the biventricular model with and without the HPS (Figure 4.5B). Each scenario corresponded to different severities of each of the three components of ischemia (e.g. mild hyperkalemia + moderate acidosis + moderate hypoxia). Computational simulations in the model that included the HPS (red bars) showed a VW approximately of 5 ms under a moderate ischemic level in all components, with CIs originating reentries between 335 and 340 ms. An individual change of

hyperkalemia, hypoxia or acidosis from moderate to severe led to an increment to 25 ms in the VW with CIs between 380 and 405 ms, 45 ms with CIs between 320 and 365 ms, and 40 ms with CIs between 340 and 380 ms, respectively. Conversely, no reentry (VW = 0 ms) was found during the individual reduction of each ischemic parameter to mild.

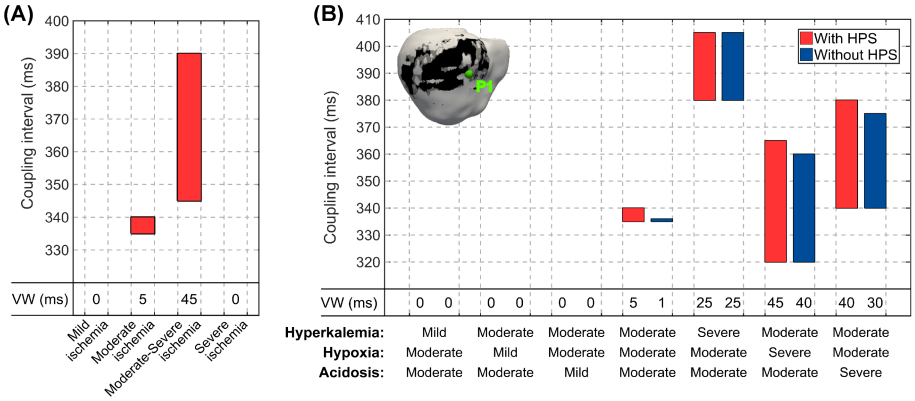

Figure 4.5 Vulnerable window (VW) for reentry. (A) VW under four different ischemic severities: mild, moderate, moderate-severe, and severe. These conditions correspond to 2.5, 5.0, 7.5, and 10.0 minutes of ischemia, respectively. (B) VW under seven different scenarios of acute ischemia. The severity of each ischemic component (hyperkalemia, hypoxia, and acidosis) in each scenario is shown at the bottom. Red and blue bars represent the results of simulations with and without the HPS, respectively. Stimulation point (P1) of the premature stimulus is show in light green inside the inset.

On the other hand, computational simulations in the model without the HPS (Figure 4.5B, blue bars) yielded reentries only for a CI = 335 ms under moderate ischemic conditions for all components of ischemia. An individual change of hyperkalemia, hypoxia or acidosis level from moderate to severe led to an increase in the VW to 25 ms with CIs between 380 and 405 ms, 40 ms with CIs between 320 and 360 ms, and 35 ms with CIs between 340 and 375 ms, respectively. Finally, any change of any ischemic component from moderate to mild did not generate reentries (VW = 0 ms).

The influence of the His-Purkinje system in the width of the VW was analyzed in the different scenarios. Results without HPS, but maintaining the normal sinus activation by stimulating the PMJ locations (as described in the Methods section), showed slight reductions in the VW width (blue bars in Figure 4.5B) with respect to simulations including the HPS (red bars). Under moderate ischemic conditions, the VW was reduced to less than 5 ms. An increment in the hyperkalemia level from moderate to severe did not produce changes in the VW between simulations with and without retrograde conduction (VW = 25 ms). On the other hand, when hypoxia or acidosis were individually increased to the severe level, the VW was reduced in 5 ms in simulations without the HPS. Furthermore, the suppression of the retrograde conduction through the HPS affected the VW only for the highest CI values (blue blocks). In summary, our results show that hypoxia has the most significant effect on the width of the VW and that the HPS is a fundamental element in the generation of reentry for higher CI values of the VW. Furthermore, the HPS provides propagation pathways favoring the maintenance of reentry.

The most common reentrant pattern observed during our acute ischemia simulations was a figure-of-eight reentry, which is in accordance with many experimental observations [112], [129], [265]. Also, the position, size and pattern of the reentrant circuit changed from beat to beat. Figure 4.6 shows the propagation patterns of a macro-reentry obtained in our biventricular model including the HPS. Simulated ischemic conditions were moderate hyperkalemia and acidosis, and severe hypoxia. Reentrant activity started with a premature stimulus (S2) in the right BZ occurring 320 ms after the fifth sinus beat (S1). In the first reentrant cycle, a unidirectional block within the ICZ (straight line, second row) gave rise to two circus movements around it, which were completed at 310 ms after S2 (third row). In the HPS, wavefronts were propagated by means of both retrograde and anterograde conduction.

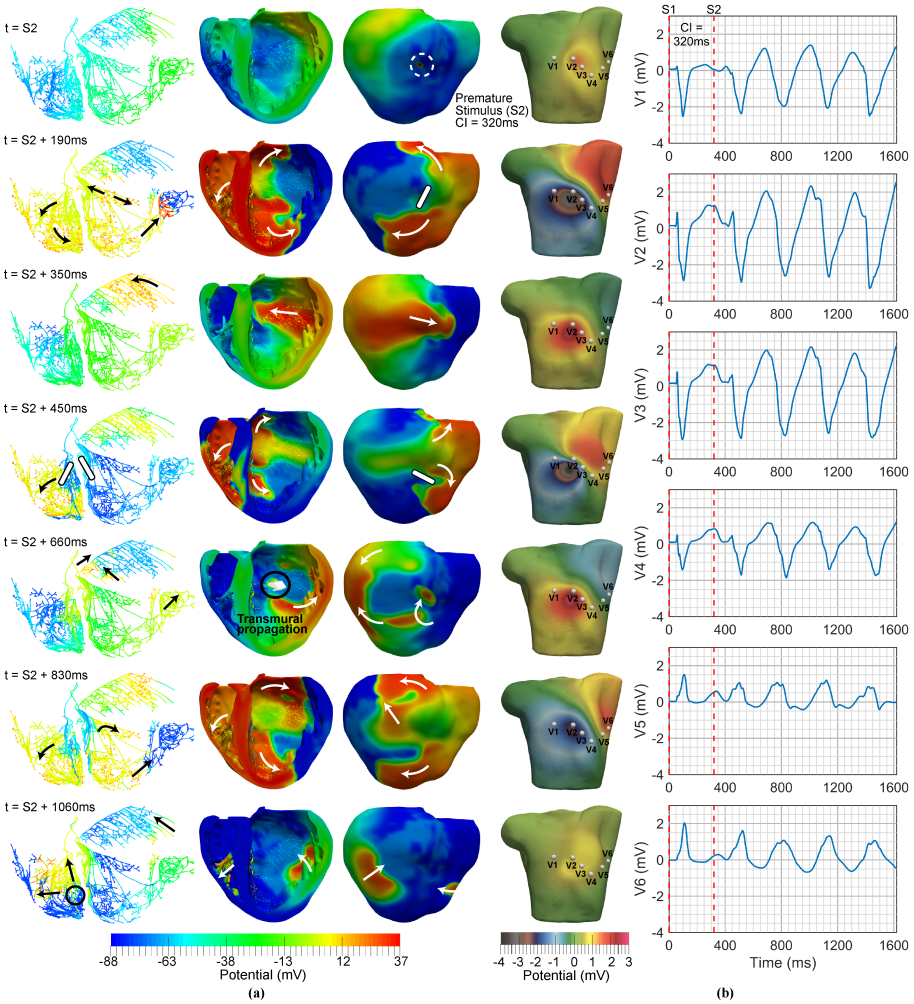

Figure 4.6 Reentrant pattern of a macro-reentry using the biventricular/torso model. (A) Ventricular potential maps that show the generation of a figure-of-eight reentry. (B) Body surface potential maps and ECG recorded at precordial leads during the reentry. The simulated ischemic conditions were moderate hyperkalemia and acidosis, and severe hypoxia. Arrows indicate the propagation direction of the wavefront, while the straight lines indicate unidirectional conduction block. The black circle in the last row shows the location where a new wavefront was generated due to current flow from the myocardium to HPS.

In the second reentrant cycle, the reentrant pattern also showed two circus movements. The lower circus movement was established around a zone of conduction block located in the lower part of the ischemic

region. The diameter of the block region was approximately 1.5 cm. The circus movement ended at 630 ms after S2 (fourth and fifth rows). The upper circus movement was established around the ICZ. This wavefront was combined with a fragmented wavefront coming from the lower circus movement, and this gave rise to the third cycle. In the HPS, a temporary conduction block was observed in two sections located on the septal wall (fourth row in Figure 4.6A).

During the third cycle of the reentry, two circus movements around the ICZ and another propagation circuit throughout the ICZ were established. The wavefront from the ICZ was combined with the upper wavefront. Later, both the lower and upper wavefronts were also combined to retrogradely cross the ICZ. During this same cycle, a wavefront was transmurally propagated to give rise to reentrant activity in the endocardium (black circle, fifth row). In the HPS, a new wavefront was generated in one of the RV PMJs due to current flow from the myocardium to the HPS. This event was produced during the repolarization of the RV septum when the HPS section located in the septum was able to allow electrical conduction (black circle, last row).

Figure 4.6B displays the body surface potential maps (BSPMs) and the ECG obtained during this particular reentry. As shown in the figure, positive and negative potential areas were registered on the torso during each reentrant cycle. A rotary clockwise pattern seems to occur in different planes. In that sense, when a reentrant cycle begins, a region of positive potential appears near the location of leads V2 and V3. Then, this region moves towards the left shoulder and from that site to the lower part of the back. Finally, the zone of positive potential returns to its initial location, giving rise to a new cycle. A clear example of this movement can be seen in the ECG computed in the precordial leads (Figure 4.6B, right). The ECG shows the typical pattern of a ventricular tachycardia with a mean cycle length of around 320 ms (which corresponds to approximately 188 beats per minute).

Figure 4.7 illustrates the role of the HPS in the generation of reentry during moderate ischemia elicited with a premature stimulus (S2) 340 ms after the onset of the last sinus beat. In the model including the HPS, a sustained reentry of at least 3 reentrant cycles was obtained (Figure 4.7A, C blue trace). Conversely, no reentry was generated under the same ischemic conditions when the HPS was removed from the model (Figure 4.7B, C red trace). In this last case, a bidirectional conduction block was observed at the right border of the ICZ.

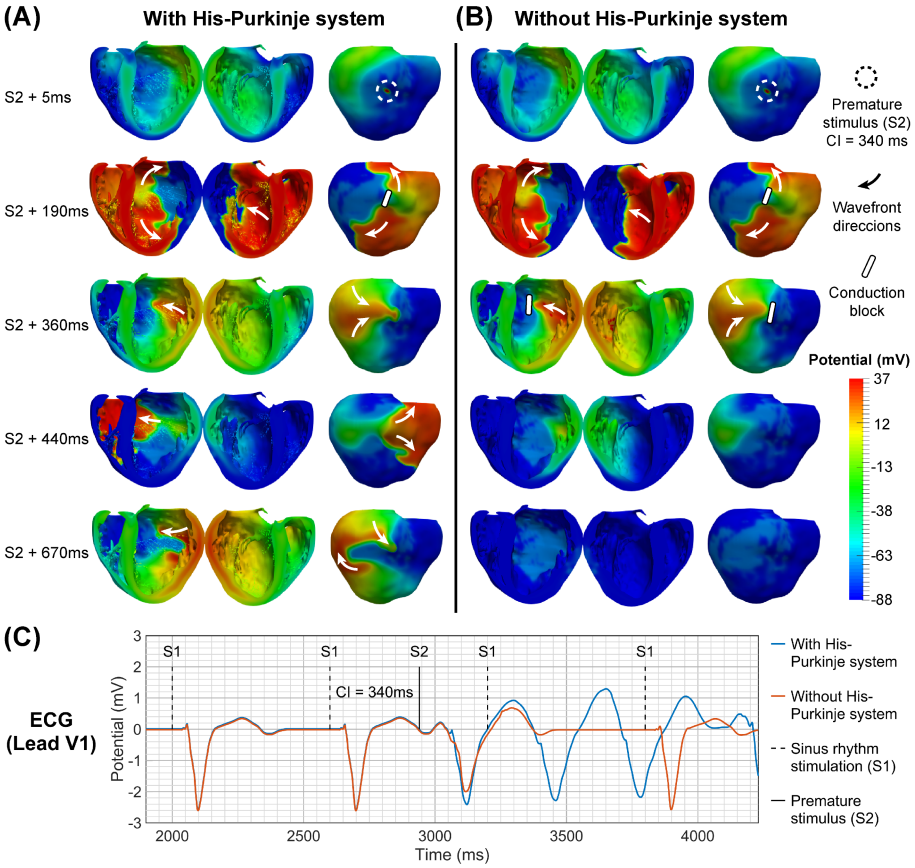

Figure 4.7 Role of the His-Purkinje system on reentry generation. (A) Macro-reentry obtained with the model that includes the HPS. (B) No reentry in the ischemic simulation using the model without HPS. (C) ECG simulated in lead V1 for both cases. Simulations were performed under moderate ischemia.

When the S2 stimulus was applied (first row), a conduction block in the ICZ produced two reentrant circuits in both scenarios (second row). This fragmented wavefront proceeded retrogradely into the ICZ and entered the NZ, sustaining the reentry during the simulation with the HPS (Figure 4.7A, third row). Conversely, the fragmented wavefront entered the ICZ but was blocked in the still refractory NZ in the simulation without HPS (Figure 4.7A, third row). Our results reveal a slow conduction velocity in the ischemic region for both scenarios. However, areas with high PMJs density within the ischemic region had a further slight reduction in conduction velocity due to current flowing from the myocardium to the HPS during the wavefront propagation through the myocardium. This slower conduction velocity in the simulations with the HPS allowed the NZ to recover once the wavefront had crossed the ICZ.

4.4 Discussion

In this study, a set of acute ischemic simulations were performed in a 3D biventricular/torso model with a realistic ischemic region and cardiac conduction system. We analyzed the influence of the three main components of ischemia (hyperkalemia, hypoxia, and acidosis) and the role of the HPS in reentry generation. Our simulations were performed using a modified version of the O'Hara et al. [37] action potential model in which we included the main ionic changes related to acute ischemia. The simulations results obtained with the model are in accordance with previous experimental and simulation studies and shed light into the mechanisms responsible for reentrant activity during acute ischemia.

The major findings of this study are the following. First, the severity of ischemia plays an essential role in determining the likelihood of reentrant arrhythmic activity. The worst scenario for arrhythmia development is moderate ischemia. Second, the single ischemic component with the most significant effect on the VW for reentry was hypoxia. Third, the retrograde conduction from the myocardium to the HPS in the ischemic region plays a decisive role in reentry generation

for higher CI values within the VW. Fourth, the hyperkalemia level in Purkinje cells affects the generation of reentries. And fifth, the maintenance of the sinus excitation overlapped with the reentrant activity does not significantly alter the wavefront propagation in the arrhythmic myocardium.

4.4.1 Role of ischemic severity in the generation of reentries

During the first 10 – 15 minutes of acute myocardial ischemia, metabolic changes in the injured tissue produce a series of electrical alterations in the affected cells, such as APD shortening, CV reduction and RMP increment to less negative values [28], [48], [114], [228]. These ischemia-induced alterations are not homogeneous within the ischemic region, but appear in the form of gradients between the ICZ and the BZ [255], [263]. In our study, simulation results for different severities (or minutes) of acute ischemia were consistent with the experimental and simulation data mentioned above. A combined effect of hyperkalemia, hypoxia, and acidosis due to ischemia led to a dispersion of refractoriness and CV in the ischemic myocardium, setting the pro-arrhythmic substrate for reentries generation [255], [266].

Previous experimental observations during acute myocardial ischemia reported that arrhythmias occur in two distinct phases: before 10 minutes, and between 20 and 40 minutes after coronary artery occlusion [94], [97], [266]. In our study, we only analyzed the appearance of arrhythmic activity during the first 10 minutes of ischemia. According to our results, reentries were triggered between the first 5 to 7.5 minutes of ischemia (moderate to moderate-severe ischemic conditions), corresponding with said first phase of arrhythmias. These results are also in agreement with the studies performed by Smith et al. [97] and Kaplinsky et al. [93], which reported that reentries occur 2 to 10 minutes after the occlusion, with the peak of arrhythmic events at 5 to 6 minutes approximately. Similarly, Morena et al. [25] reported a higher occurrence of arrhythmias and ventricular

fibrillation (VF) episodes between 3 and 8 minutes after the occlusion of the left anterior descending artery (LAD) in pigs. Finally, in the study by Coronel et al. VF was induced with one ventricular premature beat after 5 minutes of ischemia, but not after 10 minutes during LAD occlusion in perfused porcine hearts [230]. For this last experiment, an $[K^+]_o$ value between 8.0 and 13.5 mM was a necessary condition for the induction of VF.

In our simulations, reentries were generated for values of $[K^+]_o$ of 10 and 11 mM, which is in accordance with [230]. Also, in the study by Hirche et al. [253], $[K^+]_o$ levels between 10.7 ± 1.9 and 14 ± 2.9 mM were measured during the first phase of ventricular arrhythmias in pigs with acute coronary artery occlusion. Conversely, Tobar et al. [34] in their simulation study reported that reentries were not generated for values of $[K^+]_o$ greater than 9 mM. A possible explanation between the different results obtained in the present study and the one by Tobar et al. [34] lies on the most recent action potential model used in our simulations and the most realistic form of modeling the effects of acute ischemia in the AP ventricular model. In addition, the simulation study by Martinez-Navarro et al. [122] reported reentries for $[K^+]_o$ = 9.5 mM using the O'Hara model. This value is close to the levels of $[K^+]_o$ that induced reentries in our study. However in the work by Martinez-Navarro et al. [122] a realistic ischemic region and a detailed HPS were not included, as in the present research study.

4.4.2 Separate role of the ischemic component in the generation of reentries

Cells affected by acute ischemia experience hyperkalemia, hypoxia, and acidosis due to the lack of blood flow [253], [267]. However, the influence of each ischemic component on arrhythmogenesis is difficult to analyze experimentally. For this purpose, computational models have become an important tool in understanding the mechanisms responsible for reentry. For instance, Ferrero et al. [231] used computational simulations to analyze the mechanisms involved in figure-of-eight

reentry in a ring-shaped 1-dimensional strand of cardiac cells. The results of this study suggested that the most pro-arrhythmic ischemic component would be hypoxia. Subsequently, the same group studied the role of each ischemic component in the establishment of figure-of-eight reentry in a 2D model [229]. They reported that a sustained reentry can be generated under conditions of strong hyperkalemia alone ($[K^+]_o$ > 11.9 mmol/L), and that severe hypoxia tends to reduce myocardial vulnerability to reentry. Similar results were reported in the study by Trenor et al. [228]. In the latter, the authors observed that a lower hyperkalemia ($[K^+]_o \leq$ 11 mmol/L) level did not lead to reentry generation regardless of the presence of hypoxia or acidosis. In addition, a similar role of acidosis and hypoxia in the widening of the VW was reported in this study. Both computational analyses were performed using the Luo-Rudy AP model [63]. On the other hand, a more recent study by Tobar et al. [34] investigated the effects of hyperkalemia on the VW for reentry using the ten Tusscher AP model [36] in a 3D biventricular mesh. Their results showed that $[K^+]_o$ had a significant effect on the size of the VW. However, effects of hypoxia and acidosis were not analyzed.

In our study, a modified version of the O'Hara AP model was used to evaluate the individual effects of hyperkalemia, hypoxia, and acidosis in the width of VW for reentry. From a moderate ischemic severity in the three ischemic components, an individual change of a single ischemic component to mild or severe conditions was applied, resulting in a total of seven scenarios of ischemic severity analyzed (see Figure 4.5B). Our model showed that all components of ischemia affect the VW, although in a different degree and via different mechanisms. Indeed, our simulation results suggest that hypoxia has the most significant effect on the width of the VW, i.e., hypoxia could be the most pro-arrhythmic individual component of ischemia in accordance with Ferrero et al. [231]. However, this effect was only slightly major (a difference of 5 ms) compared to a change in acidosis alone, which brings our results closer to the observations reported by Trenor et al. [228], who observed a similar effect of hypoxia and acidosis on the

VW. The recent study by Lawson et al. [268] demonstrated that the wavelength (calculated as the product of APD times CV) is the most critical factor in reentry initiation, with hypoxia being the primary determinant of this factor, while acidosis had a minor effect. However, the authors mentioned that their results may underestimate the role of the lack of oxygen due to simplifications adopted by the reduced ten Tusscher ionic model used in their study. Experimentally, the relative contribution of each ischemic component to the genesis of ventricular arrhythmias is not established. That said, Wilde, in his review study about the role of ATP-sensitive K^+ channel current in ischemic arrhythmias, reported that the activation of the $I_{K(ATP)}$ current (activated by hypoxia) in the early phase of acute ischemia potentially contributes to the development of ventricular arrhythmias [269]. Moreover, the study by Said et al. [270] suggests that the presence of acidosis in perfused rat hearts may affect intracellular calcium management, causing the initiation of arrhythmias.

On the other hand, our study also shows that hyperkalemia was the ischemic component with less effect in the VW. Despite this, a minimum value of $[K^+]_o$ of 10 mM was necessary to trigger a reentry even in the presence of moderate hypoxia and acidosis. This result suggests that hyperkalemia level could play an important role in reentry generation, in agreement with the simulation study by Tobar et al. [34] and with the experimental study by Morena et al. [25]. In the latter, the regional combination of hypoxia with acidic perfusion did not generate early arrhythmia in porcine hearts. However, when hypoxia was combined with a $[K^+]_o$ around 10 mM, VT was observed after 10 minutes and VF after 20 minutes. A similar result was reported in the study performed in dogs by Senges et al. [227].

Finally, our model shows that an individual and combined change of the three ischemic components could produce opposite effects in the VW width. Indeed, an increment solely of hyperkalemia, hypoxia, or acidosis to severe conditions led to a widening of the VW, while the simultaneous increment of all components reduced the VW to 0 ms (i.e.,

no reentries were observed). This result shows the importance of the concomitant effects of the ischemic components on arrhythmogenesis, in accordance with other studies [227], [230]. In the work by Senges et al. [227] in canine hearts, the regional combination of hypoxia plus lactic acidosis, without hyperkalemia, failed to trigger reentrant arrhythmias, which were indeed observed when regional hyperkalemia was included. Similar results were reported in the study by Coronel et al. [230], which analyzed the effects on the arrhythmogenesis of both hyperkalemia and ischemia (i.e., all ischemic components). The results of their experiments showed that a reentrant arrhythmia could be generated in a tissue with $[K^+]_o$ between 8 and 13.5 mM, but only in hypoxic and acidotic conditions.

4.4.3 Role of His-Purkinje system in the generation of reentries

The role of the HPS in the generation and maintenance of ventricular arrhythmias is controversial. Experimental studies, such as Cha et al. [30] have reported that in the absence of the HPS, VF in dogs could continue but at a slower rate. Other study by Livia et al. [29] observed that the elimination of Purkinje fibers with irreversible electroporation reduced the threshold/vulnerability toward VF induction during an experiment with 8 canine hearts. Conversely, Janse et al. [27] reported that after the destruction of the subendocardium including the HPS, ectopic beats in the myocardium were triggered by ischemia, but none of these beats degenerated into VF.

In our study, simulation results showed a slight reduction of the VW when the HPS was removed from the biventricular model, in accordance with experimental observations reported by Livia et al. [29]. The inclusion of the HPS in the anatomical model played a double role in the generation of reentry. First, the HPS played an irrelevant role in the generation of reentrant activity in approximately 83% of the simulations where reentries were generated and sustained. This means that reentries were triggered without the need for HPS in 83% of the simulations. However, when the HPS was included in the model,

reentrant circuits which included the HPS in their pathways were observed in all simulations, as in [235], [271]. These circuits allowed an earlier activation of distant regions to the ischemic zone through retrograde and anterograde fast conduction, which suggests that the HPS could help to maintain a reentry as in the simulation study by Deo et al. [235]. In the latter work, authors reported that propagation pathways throughout the HPS prolong the arrhythmic activity and that the HPS plays an additional role in maintaining the later stages of reentry, although the CIs range for reentry inducibility in simulations with and without the HPS were similar. Second, in our simulations the inclusion of the HPS in the biventricular model was a necessary condition in the generation of reentries for higher CI values within the VW, opposite to the simulation results obtained by Deo et al. [235]. Indeed, our simulations revealed that the HPS further reduces conduction velocity in the ischemic region with high density of PMJs. This additional reduction allowed the NZ to recover once the wavefront had crossed the ICZ, generating a reentry.

Although our results indicate that the HPS plays an important role in the generation of reentries, they also suggest that this role depends on the degree of hyperkalemia that affects Purkinje cells. To confirm this observation, simulations under moderate ischemia were repeated in the biventricular model including the HPS, but without the effects of hyperkalemia in Purkinje cells (results not shown), i.e. no changes were made to the Purkinje AP model in ischemic conditions [236]. This change was applied in order to mimic the resistance of Purkinje to ischemia observed in several experimental studies [30], [272]. Under this consideration, no reentries were found for moderate ischemic conditions (VW = 0 ms). These results were different to the ones obtained in simulations that included the effects of hyperkalemia in the Purkinje cell (VW $\approx$ 5 ms). An explanation for the different behaviors lies on the slow CV and conduction blocks in discrete sections of the HPS due to hyperkalemia. These effects led to a delay in ventricular activation that allowed the recovery of excitability in areas of the NZ stimulated by the premature stimulus (S2). Thus, a wavefront that

propagates throughout the ICZ is able to re-stimulate the repolarized tissue. Our results are in agreement with experimental observations previously reported [273], [274]. These studies proved that slow conduction through discrete regions of Purkinje fibers subject to high $[K^+]_o$ may result in reentrant arrhythmias. Similar results were obtained in the study by Senges et al. [227] performed in the canine ventricular conduction system. In the latter study, researchers also observed that during regional hypoxia or lactic acidosis, no arrhythmias were generated, while regional increases of $[K^+]_o$ may be the predominant ischemic component to generation of reentrant arrhythmias.

Whenever reentry was induced, a typical figure-of-eight reentrant pattern was obtained in all our simulations with the biventricular model, as reported in canine and porcine hearts [112], [129], [265]. Changes in location, revolution time and size were observed in a beat-to-beat basis during each reentry. However, a changing reentrant pattern (e.g. a circus and double circus pattern) was obtained with the model that includes the HPS, similar to those observed by Janse et al. [112], [129]. All our reentries showed a VT pattern which did not evolve in VF, in accordance with other studies in animals [96], [97], [275]. In these studies, evolution from VT into VF was rare during the first phase of ischemic arrhythmias (phase 1A of arrhythmias).

Experimental evidence on the effects of heart rate on the occurrence of ventricular arrhythmias is scarce. Observations in dog hearts by Chadda et al. [276] have suggested that the sinus rhythm could be related with the initiation of ventricular arrhythmias. In this study, the authors observed that after coronary occlusion the incidence of VT and VF occurs mainly at slow and rapid heart rates. On the other hand, our simulation results showed that a sustained sinus rhythm at 100 beats/min (BCL = 600 ms) does not induce the generation or abolition of reentries. This result is supported by Sung et al. [277], who reported that tachycardia triggered by potential delayed afterdepolarizations, could be initiated by accelerating the sinus rate, but only in 3 of 21 patients with clinical evidence of recurrent sustained VT. Another study

performed in 262 subjects during 6 hours of infarction observed primary VF in 20 patients [278]. Within this group, 7 patients developed tachycardia, 10 had a sinus rate between 60 – 100 beats/min and 2 bradycardia immediately prior to VF. In summary, our results together with the experimental evidence, suggest that the effects of heart rate on reentry generation could vary among patients.

4.5 Limitations

An AP model of Purkinje cells that includes the effects of the main ischemic components has yet to be developed due to the lack of experimental information, especially in human hearts. Several studies in animals have reported that the HPS is more resistant to the effects of ischemia than cardiomyocytes, with many Purkinje fibers surviving after infarcts [272], [279], [280]. However, during the initial phase of acute ischemia it is not certain whether, or to what extent, the subendocardial Purkinje fibers change their electrophysiological properties. In this study, effects of hypoxia and acidosis in Purkinje cells were not simulated while hyperkalemia was introduced by increasing the $[K^+]_o$ as in the nearest cardiomyocyte. This $[K^+]_o$ increment has been reported as the potential predominant factor of the ischemic components that facilitates the onset of reentrant arrhythmias in Purkinje cells [227]. Although our results have been compared with experimental studies and clinical observations, a most realistic model of the effects of acute ischemia in the HPS could alter our results. Thus, the main findings should be carefully validated both in a set of computational models of different patients (with different HPS configurations) and in clinical studies.

To quantify the VW for reentry, a premature stimulus was applied in a region of the BZ. However, the location of the stimulation region in the BZ has been shown to affect the VW [122]. For this reason, a future study should investigate whether the effect of the three main ischemic components in the width the VW could be influenced by the

location of the premature stimulus or by the location of the ischemic region in the heart.

CHAPTER 5

General discussion

This chapter summarizes and briefly discusses the main contributions of the present thesis, going beyond the state of the art in the optimization of CRT in heart failure patients and in the understanding of arrhythmogenic mechanisms during acute myocardial ischemia.

5.1 Heart failure and cardiac resynchronization therapy

The study of the electrical activity of the heart, its pathologies and associated therapies using computational models has revealed additional insights for diagnosis, analysis and treatment of patients with different cardiac diseases that might otherwise have remained concealed. For instance, research in the field of CRT has made a substantial effort to improve the effectiveness of this treatment [219], [281]. Despite this, there are around 30% – 40% patients with HF and HF + LBBB who still do not respond favorably [134], [282]. Currently, CRT optimization, i.e., the determination of the optimal pacing leads location, as well as the optimal AVD and VVD values, is a hot research topic. Indeed, new techniques, such as His bundle pacing, endocardial electrodes and multi-sites pacing are being currently investigated.

In the present study, we performed CRT optimization in a 3D biventricular human model under HF + LBBB conditions, using the shortest QRSd criterion. Then, the results were compared with other optimization criteria. Our first main finding showed that the optimal leads location was the RV upper septum and the LV mid posterior region, in agreement with some experimental studies [141], [194]. These positions also minimize TAT, and therefore reduce the electrical dyssynchrony. In addition, better results were obtained with LV endocardial pacing compared to LV epicardial pacing, as in previous studies [184].

Our second main finding showed that the optimal delay configuration corresponded to AVD = 140 ms and VVD = 30 ms. These results were different to the AVD and VVD values leading to the minimum TAT. Thus, the best electrical synchrony may not be totally achieved using only the shortest QRSd criterion for CRT optimization, or to optimize biventricular pacing delay. In clinical practice, although optimization of AVD and VVD is crucial during CRT application [199], it is rarely performed.

Finally, our third main finding revealed that a biomarker based on the time to 90% of the QRS area (t_{90}QRSa) is a good predictor of the instant at which 90% of the ventricular tissue has been activated (t_{90}). Therefore, the minimization of this indicator could be a new or complementary tool to the shortest QRSd criterion for the definition the optimal location and delay of the pacing leads that produce the faster activation of ventricles.

5.2 Acute myocardial ischemia and generation of arrhythmias

Patients suffering from acute myocardial ischemia are prone to trigger complex ventricular arrhythmias due to electrophysiological alterations that occur in the affected myocardium. Experimental studies have investigated the mechanisms that initiate and sustain ischemia-

related arrhythmias [112], [265], [283]. However, it is difficult to completely understand these mechanisms using only experimental means. Computational simulations have become an important and complementary tool for this purpose [35], [284].

In the present work, we carried out computational simulations of acute myocardial ischemia using the most realistic 3D biventricular human ischemic model so far, to assess both the effects of hyperkalemia, hypoxia and acidosis on the VW to reentry, and the role of the HPS and its mechanisms of action in the generation and propagation of reentrant activity. In the first part of this investigation, our major findings showed that an intermediate ischemic condition is the worst scenario for reentry generation, as reported in experiment observations [93], [97]. In addition, hypoxia has a greater influence in the VW width, suggesting that it could be the most pro-arrhythmic individual component of ischemia, supporting the results of a previous study obtained with a simpler [231].

In the second part of this investigation about the HPS role, one of our main findings revealed that the retrograde conduction in PMJs during the inclusion of the HPS in the model, plays a decisive role in reentry generation for higher CI values within the VW. A study in canine hearts reported retrograde and anterograde propagation between myocardium and HPS during VF [232]. Our second main finding demonstrated that the effect the HPS in the onset of reentry depends on the degree of hyperkalemia that affects Purkinje cells, in agreement with the experimental study by Cranefield et al. [273]. Finally, our third main finding showed that the propagation patterns in the myocardium are not significantly altered when sinus rhythm overlaps with the reentrant activity. In addition, a sustained heart rate of 100 bpm is not able to induce reentry, similar to observations reported in the study by Sung et al. [277].

CHAPTER 6

Conclusions and outlook

6.1 Conclusions

The main objective of this doctoral thesis was to study the mechanisms underlying ventricular arrhythmias and their response to electrical therapies in a three-dimensional realistic anatomical model of the human ventricles under HF with LBBB and acute myocardial ischemic conditions using computer simulations. To do so, first we modified what was the most recent ventricular AP model (developed by O'Hara) available at the beginning of this doctoral thesis, validating it against the experimental data. Regarding CRT, we can conclude from our results that CRT optimization is crucial to reduce the electrical dyssynchrony in HF + LBBB patients. However, an optimization based solely on the shortest QRSd criterion is not totally effective. If this classical criterion is combined with our newly defined index t_{90}QRSa, CRT optimization leads to better ventricular synchrony. On the other hand, regarding acute myocardial ischemia, we can also conclude that patients under moderate ischemic conditions have the highest likelihood to develop malignant arrhythmias. The most pro-arrhythmic effect of hypoxia during acute ischemia suggests that $I_{K(ATP)}$ could be a therapeutic target for the reduction of arrhythmic events. Furthermore, the favorable role of the HPS in the onset and maintenance of VTs

shows that PMJs could be an optimal site for the termination of arrhythmias by radiofrequency ablation.

The following is a summary of our main findings is provided for each of the specific aims of this doctoral thesis.

GOAL: To improve the most recent human ventricular AP models to more realistically simulate the electrical behavior of the heart suffering from HF with LBBB and acute myocardial ischemia based on extensive literature review.

CONCLUSION: The O'Hara AP model, considered with our modifications, allowed us to overcome the constraints of the original model as well as to simulate the main alterations at cellular and intercellular level caused by the pathologies of (a) HF with LBBB and (b) acute myocardial ischemia. In physiological conditions, our results show that changes in the I_{Na} and I_{NaL} currents formulation lead to a more realistic CV and allow realistic electrical propagation in 3D ventricular tissue compared to the original model. In the HF + LBBB simulations, our new version of the O'Hara model reproduces the reduced CV caused by the decrease in connexin43 expression and/or conductance. Under acute myocardial ischemic conditions, the modification of several currents and the incorporation of others in the AP model allowed us to replicate the electrophysiological alterations observed experimentally in the ischemic cells, mainly the increase in PRR, a phenomenon that does not exist with the original O'Hara model.

GOAL: To improve the 3D anatomical models of the human ventricles by incorporating a His-Purkinje system that allows obtaining a realistic ECG morphology in the precordial leads in healthy and pathological conditions.

CONCLUSION: The HPS incorporated in our 3D anatomical model includes the main structural and functional properties published in the literature. Simulations performed including the HPS in healthy

conditions allowed a synchronized activation of the ventricles with a TAT within the physiologic values. Thus, a typical ECG morphology was obtained in the precordial leads on the torso surface.

In pathological conditions, simulations with the HPS included in the model reproduced the widening of QRSd under HF + LBBB conditions, and the opposite effect during the CRT application. Moreover, the inclusion of the HPS in the model played an important role in the CRT optimization, especially when the LV lead was located in the endocardium. For this last scenario, our results show that electrical propagation through HPS by retrograde conduction in the PMJs could contribute to improve CRT outcomes.

Under acute myocardial ischemic conditions, simulations using the model with the HPS included reproduced the main changes in the ST segment and T wave reported experimentally. Our simulation results revealed that the presence of the HPS increases the likelihood of reentry. The flow of current from the myocardium into the HPS in the ischemic region, conduction blocks in discrete sections of the HPS, and the degree of ischemia affecting the Purkinje cells, are suggested as mechanisms that could favor the triggering of ventricular arrhythmias.

GOAL: To analyze the optimal pacing leads location and AVD and VVD settings during CRT procedure in a tissue with HF and LBBB, based on the shortest QRS duration criterion. Subsequently, the results are to be compared with other optimization criteria.

CONCLUSION: Optimization of CRT is crucial to improve the electrical synchrony of the ventricles and LV ejection fraction in patients with HF and LBBB. Based on the shortest QRSd criterion, CRT simulations show that the optimal location for the RV lead, as an alternative to the RV apex, is the upper septum close to the outflow tract. The analysis of the optimal LV lead location revealed that endocardial stimulation leads to better CRT outcome than epicardial

stimulation. Furthermore, myocardial areas with a higher density of PMJ are suggested to improve CRT response.

Our simulations also demonstrated that CRT optimization based only on the shortest QRSd criterion may not be totally effective to reach the maximum TAT reduction, or to optimize biventricular pacing delay. However, a biomarker based on minimizing the value of t_{90} (time elapsed to 90% of ventricular activation) could be used to determine the optimal VVD value. The t_{90} is related to the time to reach the 90% of the QRS area (t_{90}QRSa), allowing it to be calculated non-invasively using only the ECG measured on the torso surface. Thus, t_{90}QRSa is suggested as an additional index to assess CRT effectiveness to improve biventricular synchrony.

GOAL: To investigate the effects of hyperkalemia, hypoxia and acidosis, as well as the role of the His-Purkinje system, in the vulnerability to reentry during different ischemic severity scenarios.

CONCLUSION: Simulation results performed in our 3D biventricular model are in accordance with reported experimental data. All reentries obtained show a reentrant pattern and ECG morphology similar to clinical VTs. The analysis of the VW for reentry under different ischemic scenarios showed that reentries can be only generated in intermediate ischemic conditions. Individual changes in the severity of hyperkalemia, hypoxia and acidosis may have opposite effect on the VW than a simultaneous change. In addition, hypoxia is the component of acute ischemia with the most significant effect on the width of the VW.

On the other hand, the study of the role of the HPS in the onset and maintenance of arrhythmias revealed that its inclusion in the anatomical model was decisive to generate reentries for higher CI values within the VW. Simulations performed to evaluate the Purkinje resistance to ischemia show that the degree of hyperkalemia in Purkinje cells

influences the triggering of reentries. Finally, the maintenance of the sinus excitation overlapped with the reentrant activity does not significantly alter the wavefront propagation in the arrhythmic myocardium.

6.2 Future work

Some of the limitations encountered in the studies presented in this Doctoral Thesis could be overcome by performing future research works described in this section. Our results can also be reinforced with clinical studies and a set of computational models of different patients. In this regard, several guidelines for next investigations are detailed in the paragraphs below.

Extension of the study improving HF model. During HF, myocytes undergo a series of electrophysiological changes. In the present study, in order to simulate HF we reduced the CV by 50% in accordance with protein connexin 43 reduction. This change led to QRS modifications similar to those observed in the clinical practice. However, a more realistic model of HF could also include alterations in the AP and calcium handling caused by HF remodeling. Thus, it would be very interesting to investigate in a future work the effects of these alterations during CRT application.

Coupling a mechanical model to the electrical model of the heart. In our study, CRT optimization was assessed from an electrical point of view. However, during clinical CRT application it is common to analyze the electrical synchrony as well as the hemodynamic response (mechanical function) of the heart. Therefore, it is important to evaluate whether CRT optimization based on the shortest QRSd leads to the better LV ejection fraction. In addition, strategies of multi-site pacing could be also evaluated.

Analysis of the t_{90}QRSa as an index to asses CRT effectiveness. About one third of HF patients do not respond to CRT; it is thus of vital

importance to improve this treatment. A new biomarker based on the time to reach the 90% of the QRS area (t_{90}QRSa**)** was suggested in our study as a complementary indicator for CRT optimization. In order to investigate the effectiveness of this non-invasive biomarker, it would be a crucial complement to this study a deeper analysis using a set of 3D anatomical models of different patients and validated against clinical data.

Study of the influence of ischemic region location and premature stimulus location. Simulations results using our anatomical model have shown that hypoxia is the ischemic component with the most significant effect on the width of the VW. However, factors such as location of the ischemic region and location of the premature stimulus, have also an influence on this parameter. Thus, an extension of our study could determine whether the effect of each ischemic component on the VW could be affected by these factors.

Use of improved AP models of Purkinje cell. A recent Purkinje AP model based on undiseased human hearts data has been recently published [285]. The model reproduces all AP features observed in humans, although AP alterations due to acute myocardial ischemia have not been studied. It would be valuable to assess and improve the response of this new model under ischemic conditions, and then, extend the study of role of HPS in the generation and maintenance of ventricular arrhythmias.

PUBLICATIONS

The contributions derived from this Doctoral Thesis are detailed below.

International Journal

1. **Carpio EF**, Gomez JF, Rodríguez-Matas JF, Trenor B, Ferrero JM. Analysis of vulnerability to reentry in acute myocardial ischemia using a realistic human heart model. *IEEE Transactions on Biomedical Engineering*. Manuscript in preparation.

2. **Carpio EF**, Gomez JF, Sebastian R, Lopez-Perez A, Castellanos E, Almendral J, Ferrero JM, Trenor B. Optimization of Lead Placement in the Right Ventricle During Cardiac Resynchronization Therapy. A Simulation Study. *Front Physiol*. 2019 Feb 11; 10:74. doi: 10.3389/fphys.2019.00074.
   JIF 2019: 3.367; Q1

Conferences

1. **Carpio EF**, Gomez JF, Rodríguez-Matas JF, Trenor B, Ferrero JM. Computational Analysis of Vulnerability to Reentry in Acute Myocardial Ischemia. *47th Computing in Cardiology Conference (CinC 2020)*, Rimini (Italy).

2. **Carpio EF**, Mora MT, Gomez JF, Ferrero JM, Trenor B. Multiscale modeling of human heart failure to optimize treatments. *2019 Cardiac Physiome Meeting*, Maastricht (Netherlands).

3. **Carpio EF**, Gomez JF, Sebastian R, Lopez-Perez A, Castellanos E, Almendral J, Ferrero JM, Trenor B. Optimization of Cardiac Resynchronization Therapy in 3D Electrophysiological Ventricular Models. *2019 Workshop on Cardiac Modelling: Towards an integrated numerical heart model, coupling the relevant physics the right way*, Bad Herrenalb (Germany).

APPENDIX A

1. Supplementary Data

Original O'Hara et al. formulation [37]

$$m_\infty = \frac{1}{1+\exp\left(\frac{-(V+39.57)}{9.871}\right)}$$

$$h_\infty = j_\infty = \frac{1}{1+\exp\left(\frac{V+82.9}{6.086}\right)}$$

$$h_{CaMK,\infty} = \frac{1}{1+\exp\left(\frac{V+89.1}{6.086}\right)}$$

$$\tau_{h,fast} = \frac{1}{1.432\cdot 10^{-5}\cdot\exp\left(\frac{-(V+1.196)}{6.285}\right)+6.149\cdot\exp\left(\frac{V+0.5096}{20.27}\right)}$$

$$\tau_j = 2.038 + \frac{1}{0.02136\cdot\exp\left(\frac{-(V+100.6)}{8.281}\right)+0.3052\cdot\exp\left(\frac{V+0.9941}{38.45}\right)}$$

$$G_{Na} = 75, \qquad G_{NaL} = 0.0075$$

Modified O'Hara et al. formulation

$$m_\infty = \frac{1}{1+\exp\left(\frac{-(V+48.97)}{7.5}\right)} \qquad [167]$$

$$h_\infty = j_\infty = \frac{1}{1+\exp\left(\frac{V+78.5}{6.22}\right)} \qquad [166]$$

$$h_{CaMK,\infty} = \frac{1}{1 + \exp\left(\frac{V + 84.7}{6.22}\right)} \qquad [166]$$

$$\tau_{h,fast} = \frac{1}{3.6860 \cdot 10^{-6} \cdot \exp\left(\frac{-(V + 3.8875)}{7.8579}\right) + 16 \cdot \exp\left(\frac{V - 0.4963}{9.1843}\right)} \qquad [168]$$

$$\tau_j = 4.8590 + \frac{1}{0.8628 \cdot \exp\left(\frac{-(V + 116.7258)}{7.6005}\right) + 1.1096 \cdot \exp\left(\frac{V + 6.2719}{9.0358}\right)} \qquad [168]$$

$$G_{Na} = 17 \qquad G_{NaL} = 0.0144$$

where

m_∞	steady state activation gate of the sodium current (I_{Na})
h_∞	steady state inactivation gate of the I_{Na}
j_∞	recovery from inactivation for fast I_{Na}
$h_{CaMK,\infty}$	phosphorylated steady state inactivation gate of the I_{Na}
$\tau_{h,fast}$	fast time constant of gate h
τ_j	time constant of gate j
V	membrane voltage (mV)
G_{Na}	I_{Na} conductance
G_{NaL}	I_{NaL} conductance

3D ventricular model

Cardiac DE-MRI was acquired by an MRI scanner Magnetom Avanto 1.5T (Siemens Healthcare, Erlangen, Germany) using a phased-array body surface coil, about 15 minutes after the administration of the gadolinium-based contrast MultiHance (gadobenate dimeglumine, 529 mg/ml) (Bracco Diagnostics Inc., Monroe Township, New Jersey, USA). The acquisition was synchronized with both ECG (ECG-gated) and breathing (navigator-gated), imaging the heart at the end-diastolic phase of cardiac cycle. The DE-MRI stack comprised 96 slices of 256×256 pixels encompassing the whole heart (ventricles and atria), with a pixel size of 1.4×1.4 mm and a slice thickness of 1.4 mm, thus

resulting in isotropic voxel. The cardiac DE-MRI was acquired from the Hospital Clinic Universitari de Valencia (Valencia, Spain). Regarding the ethical considerations, the protocol was approved by the Ethics Committee for Clinical Research of the Hospital Clinic Universitari de Valencia, which certifies that the present study was conducted in accordance with the recommendations gathered in the Declaration of Helsinki, originally adopted by the General Assembly of the World Medical Association in 1964, and in its subsequent revisions. Furthermore, the patient, who underwent the standard clinical protocol, gave written informed consent for the use of his anonymized clinical data in this study.

We generated the 3D patient-specific bi-ventricular model by segmenting the short-axis slices from the cardiac DE-MRI using Seg3D software (Scientific Computing and Imaging Institute, University of Utah, USA) [155]. We did it manually to perform a highly detailed segmentation of the whole ventricles, including papillary muscles and main endocardial trabeculae (see Figure 3.1). An expert radiologist in cardiac imaging checked all segmentations in order to ensure the fidelity of the 3D reconstruction of the patient-specific anatomy. From the segmented DE-MRI stack, we generated a surface model of the ventricles, carefully checked with Blender (Blender Foundation, Amsterdam, The Netherlands) to refine and correct defects in the mesh at the local level after applying a global smoothing. Then, using the surface model as a template, we performed a volume meshing with MeshGems-Hexa (Distene S.A.S., Bruyeres-le-Chatel, France), obtaining a hexahedra-based volume mesh comprised by 4 million nodes (vertices) and 3.71 million elements, with an average edge length 162 of 0.4 mm.

3D torso model

The torso dataset was obtained from the online open repository at the Centre for Integrative Biomedical Computing (CIBC) from

University of Utah [164]. The whole torso MRI stack was acquired in the coronal plane with a slice thickness of 10 mm. We roughly segmented the main organs (lungs, liver, heart) and structures (bones, body contour, blood pools, great vessels) using Seg3D software. The resolution of the torso MRI hampered a detailed reconstruction of some important structures, so we used the reconstructed parts of the model as landmarks to fit a detailed torso model previously developed [163] by means of a linear transformation. Next, we replaced the ventricles in the fitted detailed torso model by our patient specific model and removed any intersections between our ventricular model and surrounding organs. Finally, we used TetGen [286] to mesh the torso volume with tetrahedra, which resulted in 1.26 million nodes and 7.38 million elements organs. The average edge length was of 0.55 mm. Note that the problem of passive propagation of extracellular potentials, i.e. only diffusion without reaction component, does not require such a fine spatial resolution outside the heart domain [165]; for this reason, the mesh is highly refined only in the region of the ventricles.

We automatically labelled every tetrahedral element of the volume mesh as belonging to a given organ. The 3D torso model included bones, lungs, liver, whole heart (ventricles and atria) and blood pools of all cardiac chambers organs (see Figure 3.1). As in [163], conductivity values assigned to different organs and tissues were taken from the literature [287]–[291]. We considered isotropic propagation for all organs and tissues of our 3D torso model, except for the ventricular myocardium where we preserved the anisotropy imposed by the orientation of cardiac fibers. As in [290], for the space not covered by any organ or anatomical structure we set a conductivity of 0.239 S/m calculated as the average of the conductivities for the other tissues, including the skeletal muscle that was not considered as a specific region in our torso model. Finally, to simulate ECG signals we defined virtual electrodes on the surface of torso model corresponding to the precordial leads, which were placed in their standard positions (see Figure 3.1).

Computational simulations

To perform the simulations at the organ level, we used the software ELVIRA [170], FEM solver specifically developed for solving the anisotropic reaction-diffusion equation of the monodomain model for cardiac EP [292]. For the numerical solution of our simulations, we applied the conjugate gradient method with an integration time step of 0.02 ms, using implicit integration for the parabolic partial differential equation of monodomain model and explicit integration with adaptive time stepping for the systems of ordinary differential equations associated with the ionic model [37].

To obtain ECG signals on the body surface, we used an approximation of the bidomain model [293] to compute the extracellular potentials across the torso volume. This approximation, described elsewhere [174], comprises several steps. First, transmembrane potentials, previously computed by simulation at the organ level using the solver ELVIRA as explained above, were interpolated from the ventricular mesh model to the nodes of torso model corresponding to the ventricular myocardium. Then, solving the passive term (only diffusion) of the bidomain approach we obtained the extracellular potentials in the ventricles from the interpolated transmembrane voltages. Finally, applying Dirichlet boundary conditions at the ventricles-torso interface and Neumann-type conditions at the torso surface, the extracellular potentials were computed by using the FEM method to solve the Laplace equation over the volume mesh of the 3D torso model. To obtain the numerical solution of the problem, we used the conjugate gradient method with the incomplete Cholesky decomposition as a preconditioner.

2. Supplementary figures and tables

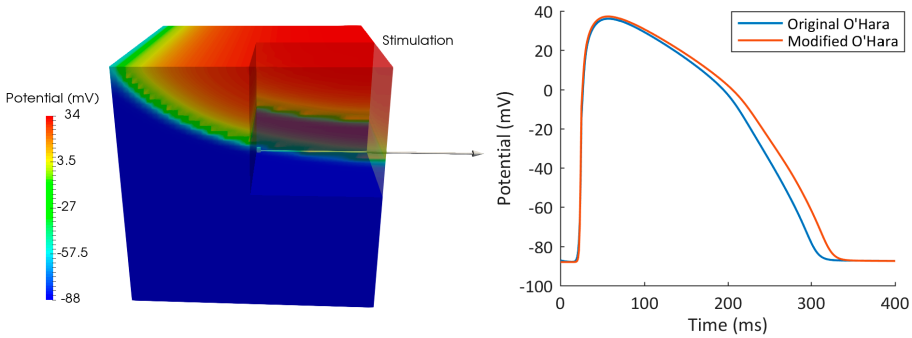

Figure A.1 Action potentials simulated in a cube with original O'Hara model (blue line) and with modified O'Hara model (red line).

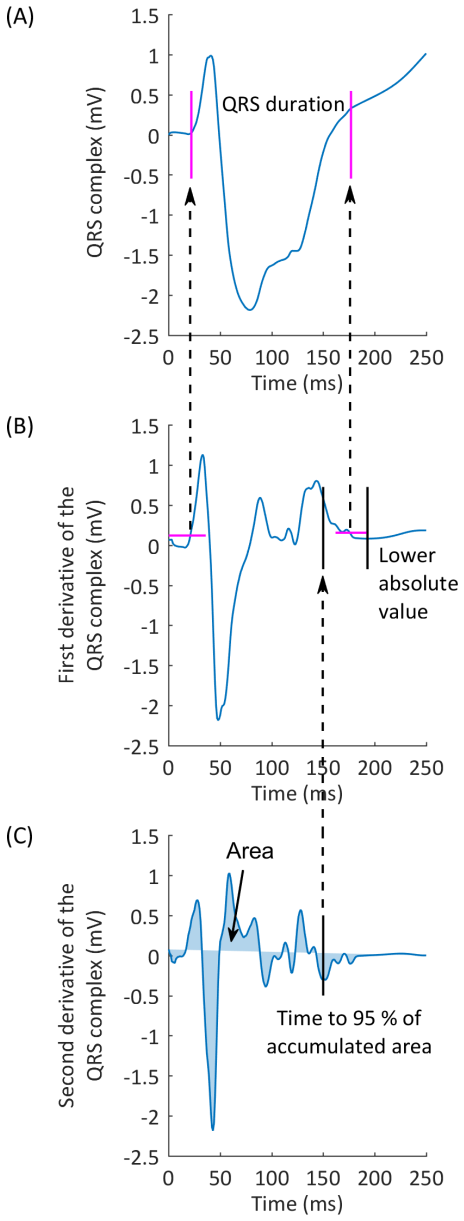

Figure A.2 Measurement of QRS duration. (A) QRS Complex where the onset and end of the QRS is shown. (B) First derivative of the QRS complex with the thresholds used (magenta lines) to determinate the QRS duration. The black lines indicate the limits of the time interval. (C) Second derivative of the QRS complex. The blue region represents the area under of second derivative and the black line indicates the time to 95 % of accumulated area.

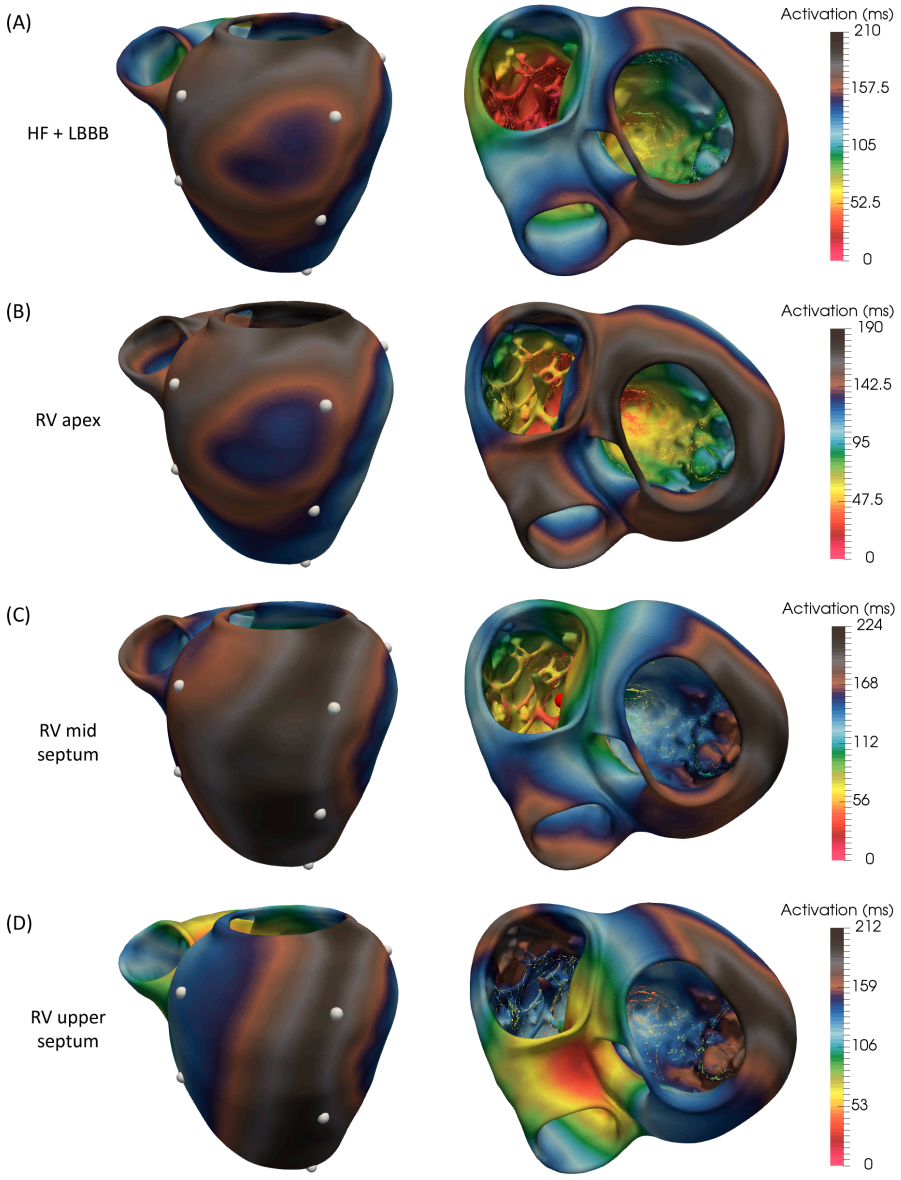

Figure A.3 Activation maps. (A) HF + LBBB configuration showing LV anterior mid and basal regions as latest activated areas. (B) Univentricular stimulation with RV lead placed in the apex. (C) Univentricular stimulation with RV lead placed in the mid septum. (D) Univentricular stimulation with RV lead placed in upper septum.

Lead locations		QRS duration (ms)							
		LV epicardial stimulation				LV endocardial stimulation			
RV	LV	AVD = 100 VVD = 0	AVD = 100 VVD = 30	AVD = 140 VVD = 0	AVD = 140 VVD = 30	AVD = 100 VVD = 0	AVD = 100 VVD = 30	AVD = 140 VVD = 0	AVD = 140 VVD = 30
Apex	Anterior - apex	179	184	179	184	169	182	169	182
	Anterior - mid	178	206	178	205	171	186	171	186
	Anterior - base	181	201	181	201	175	187	175	186
	Lateral - apex	181	196	181	195	169	175	169	174
	Lateral - mid	175	206	175	206	171	189	171	188
	Lateral - base	179	205	179	205	174	200	174	199
	Posterior - apex	181	206	181	202	176	180	176	173
	Posterior - mid	172	199	172	199	173	157	173	158
	Posterior - base	173	194	173	194	171	194	171	193
Mid Septum	Anterior - apex	173	182	173	181	174	193	174	195
	Anterior - mid	205	177	205	190	165	171	165	170
	Anterior - base	182	189	182	194	177	174	177	178
	Lateral - apex	182	205	182	203	171	188	171	188
	Lateral - mid	174	203	174	198	175	201	175	193
	Lateral - base	185	201	185	210	174	199	174	205
	Posterior - apex	187	203	187	202	176	190	176	189
	Posterior - mid	167	163	167	161	146	158	146	159
	Posterior - base	181	190	181	206	182	196	182	201
Upper Septum	Anterior - apex	180	194	167	177	175	174	155	162
	Anterior - mid	185	203	182	192	186	187	165	165
	Anterior - base	183	194	188	192	178	185	176	177
	Lateral - apex	185	200	177	194	166	162	156	157
	Lateral - mid	181	182	171	167	183	196	157	154
	Lateral - base	178	196	170	171	180	191	172	175
	Posterior - apex	198	205	183	206	171	167	168	166
	Posterior - mid	159	162	155	149	158	154	143	140
	Posterior - base	180	180	190	190	183	176	187	185

Table A.1 QRS duration (QRSd) estimated for all CRT configurations.

Lead locations		Total activation time (ms)							
		LV epicardial stimulation				LV endocardial stimulation			
RV	LV	AVD = 100 VVD = 0	AVD = 100 VVD = 30	AVD = 140 VVD = 0	AVD = 140 VVD = 30	AVD = 100 VVD = 0	AVD = 100 VVD = 30	AVD = 140 VVD = 0	AVD = 140 VVD = 30
Apex	Anterior - apex	190	218	190	218	185	202	185	202
	Anterior - mid	190	218	190	218	190	209	190	209
	Anterior - base	185	205	185	205	178	187	178	187
	Lateral - apex	190	220	190	220	175	200	175	200
	Lateral - mid	190	220	190	220	190	218	190	218
	Lateral - base	188	209	188	209	190	213	190	213
	Posterior - apex	190	219	190	219	181	202	181	202
	Posterior - mid	178	202	178	202	174	181	174	181
	Posterior - base	181	204	181	204	181	204	181	203
Mid Septum	Anterior - apex	203	212	203	212	185	206	185	204
	Anterior - mid	212	224	212	224	195	210	195	210
	Anterior - base	194	207	194	207	186	188	186	187
	Lateral - apex	215	228	215	228	185	200	185	200
	Lateral - mid	187	215	187	211	186	214	186	210
	Lateral - base	186	215	186	211	186	215	186	211
	Posterior - apex	218	220	218	220	185	206	185	203
	Posterior - mid	185	205	185	203	179	182	179	182
	Posterior - base	191	215	191	210	190	214	190	210
Upper Septum	Anterior - apex	200	212	200	212	180	185	180	180
	Anterior - mid	209	222	209	222	192	210	192	206
	Anterior - base	192	210	192	205	187	197	185	186
	Lateral - apex	211	225	211	225	171	175	171	171
	Lateral - mid	189	210	184	192	188	203	176	188
	Lateral - base	189	210	175	189	189	210	175	189
	Posterior - apex	212	220	212	220	181	182	181	181
	Posterior - mid	170	178	170	171	158	169	152	164
	Posterior - base	190	190	190	190	188	188	188	188

Table A.2 Total activation time (TAT) values estimated for all CRT configurations.

Lead locations		Time to 90% of ventricular activation (ms)							
		LV epicardial stimulation				LV endocardial stimulation			
RV	LV	AVD = 100 VVD = 0	AVD = 100 VVD = 30	AVD = 140 VVD = 0	AVD = 140 VVD = 30	AVD = 100 VVD = 0	AVD = 100 VVD = 30	AVD = 140 VVD = 0	AVD = 140 VVD = 30
Apex	Anterior - apex	145	165	145	165	136	141	136	141
	Anterior - mid	136	155	136	155	134	150	134	149
	Anterior - base	131	150	131	150	129	145	129	145
	Lateral - apex	143	170	143	169	129	134	129	134
	Lateral - mid	136	156	136	156	139	156	139	156
	Lateral - base	133	153	133	153	133	155	133	155
	Posterior - apex	145	172	145	172	139	143	139	143
	Posterior - mid	135	147	135	147	122	130	122	130
	Posterior - base	137	158	137	158	137	157	137	157
Mid Septum	Anterior - apex	152	161	152	161	133	142	133	141
	Anterior - mid	144	153	144	152	134	145	134	144
	Anterior - base	153	164	153	163	150	154	150	154
	Lateral - apex	155	173	155	172	128	135	128	134
	Lateral - mid	138	154	138	153	139	155	139	154
	Lateral - base	143	155	143	154	145	158	145	157
	Posterior - apex	161	172	161	172	138	144	138	143
	Posterior - mid	145	150	145	149	127	131	127	130
	Posterior - base	162	169	162	169	162	168	162	168
Upper Septum	Anterior - apex	147	157	143	153	127	137	125	134
	Anterior - mid	151	160	144	153	141	151	134	143
	Anterior - base	157	168	153	162	153	156	150	153
	Lateral - apex	151	167	145	162	123	130	122	129
	Lateral - mid	142	153	133	142	136	148	128	139
	Lateral - base	147	155	139	146	148	158	141	149
	Posterior - apex	151	162	149	161	132	140	132	138
	Posterior - mid	142	147	140	145	127	132	123	128
	Posterior - base	154	163	152	161	153	162	151	160

Table A.3 Time to 90% of ventricular activation (t_{90}) estimated for all CRT configurations.

Lead locations		QRS area (mV·ms)							
		LV epicardial stimulation				LV endocardial stimulation			
RV	LV	AVD = 100 VVD = 0	AVD = 100 VVD = 30	AVD = 140 VVD = 0	AVD = 140 VVD = 30	AVD = 100 VVD = 0	AVD = 100 VVD = 30	AVD = 140 VVD = 0	AVD = 140 VVD = 30
Apex	Anterior - apex	157.2	156.0	157.2	156.0	146.1	125.1	146.1	124.3
	Anterior - mid	108.4	82.7	108.4	82.8	115.7	95.6	115.7	95.1
	Anterior - base	103.5	87.3	103.5	87.8	101.6	73.1	101.6	73.2
	Lateral - apex	115.5	134.3	115.5	133.6	116.7	116.2	116.7	115.6
	Lateral - mid	84.3	78.7	84.3	78.1	130.1	118.7	130.1	117.4
	Lateral - base	119.2	109.0	119.2	109.3	125.9	110.1	125.9	110.3
	Posterior - apex	125.9	109.7	125.9	108.9	117.2	109.5	117.2	108.4
	Posterior - mid	112.6	79.1	112.6	79.1	86.9	81.8	86.9	82.0
	Posterior - base	131.1	113.5	131.1	114.0	129.0	109.3	129.0	109.5
Mid Septum	Anterior - apex	119.8	124.2	119.8	127.1	102.1	115.4	102.1	113.9
	Anterior - mid	76.6	64.7	76.6	58.6	92.8	72.5	92.8	78.6
	Anterior - base	101.8	97.8	101.8	87.6	110.0	108.0	110.0	100.1
	Lateral - apex	96.8	115.7	96.8	108.8	99.6	109.9	99.6	108.9
	Lateral - mid	61.0	94.0	61.0	84.6	104.1	111.3	104.1	109.0
	Lateral - base	105.7	87.9	105.7	83.6	111.6	91.2	111.6	87.6
	Posterior - apex	84.7	100.0	84.7	98.0	109.5	102.3	109.5	101.1
	Posterior - mid	98.1	94.3	98.1	91.3	95.7	89.0	95.7	90.5
	Posterior - base	127.9	103.8	127.9	97.5	125.1	103.7	125.1	96.2
Upper Septum	Anterior - apex	91.7	118.4	94.9	118.6	93.8	103.3	87.9	96.1
	Anterior - mid	65.5	68.1	69.0	64.0	73.1	70.7	86.5	80.4
	Anterior - base	114.5	118.4	113.9	104.9	123.8	128.7	118.9	106.9
	Lateral - apex	86.6	110.6	82.4	104.6	96.6	100.5	93.9	96.7
	Lateral - mid	93.7	103.1	74.3	73.4	95.0	104.2	88.0	90.6
	Lateral - base	106.5	98.7	107.0	97.9	110.0	96.3	112.6	102.9
	Posterior - apex	75.9	91.8	78.2	90.3	96.0	95.8	97.5	93.3
	Posterior - mid	102.0	93.5	106.7	98.0	92.8	90.8	97.7	90.2
	Posterior - base	116.0	111.3	119.5	111.7	115.8	111.5	118.6	109.6

Table A.4 QRS area estimated for all CRT configurations.

Lead locations		Time to 90% QRS area (ms)							
		LV epicardial stimulation				LV endocardial stimulation			
RV	LV	AVD = 100 VVD = 0	AVD = 100 VVD = 30	AVD = 140 VVD = 0	AVD = 140 VVD = 30	AVD = 100 VVD = 0	AVD = 100 VVD = 30	AVD = 140 VVD = 0	AVD = 140 VVD = 30
Apex	Anterior - apex	142	156	142	156	131	140	131	140
	Anterior - mid	138	160	138	160	133	149	133	149
	Anterior - base	127	150	127	149	125	148	125	148
	Lateral - apex	144	164	144	163	129	136	129	135
	Lateral - mid	141	165	141	165	138	158	138	158
	Lateral - base	133	154	133	153	133	156	133	156
	Posterior - apex	144	173	144	172	138	144	138	143
	Posterior - mid	135	154	135	154	128	135	128	135
	Posterior - base	138	162	138	162	138	162	138	162
Mid Septum	Anterior - apex	150	156	150	155	136	144	136	144
	Anterior - mid	154	159	154	159	138	149	138	147
	Anterior - base	160	173	160	171	160	162	160	163
	Lateral - apex	155	175	155	173	131	141	131	140
	Lateral - mid	153	172	153	170	148	162	148	161
	Lateral - base	149	167	149	163	151	169	151	166
	Posterior - apex	164	177	164	176	139	149	139	147
	Posterior - mid	150	153	150	153	130	137	130	135
	Posterior - base	168	176	168	176	167	175	167	174
Upper Septum	Anterior - apex	143	156	139	149	131	138	127	134
	Anterior - mid	153	166	148	159	147	157	136	146
	Anterior - base	161	173	160	169	158	162	159	162
	Lateral - apex	148	165	147	162	128	133	125	130
	Lateral - mid	143	153	134	147	141	153	132	145
	Lateral - base	150	153	148	150	153	156	151	152
	Posterior - apex	153	168	150	166	136	141	134	139
	Posterior - mid	144	150	144	150	130	137	128	131
	Posterior - base	164	171	163	169	163	169	162	168

Table A.5 Time to reach the 90% of the QRS area (t_{90}QRSa) estimated for all CRT configurations.

3. Supplementary videos

Video 1 CRT
https://youtu.be/Dp7GBOK6nJk

Video 2 Retrograde conduction
https://youtu.be/2Bqh_AfWzPU

REFERENCES

[1] E. Wilkins *et al.*, "European Cardiovascular Disease Statistics 2017 edition," Brussels, 2017. [Online]. Available: www.ehnheart.org.

[2] WHO, "World Health Statistics 2018: Monitoring health for the SDGs," World Health Organization, Geneva, 2018. Accessed: Sep. 30, 2020. [Online]. Available: http://www.who.int/gho/publications/world_health_statistics/2018/en/.

[3] M. Holmberg, S. Holmberg, and J. Herlitz, "Incidence, duration and survival of ventricular fibrillation in out-of-hospital cardiac arrest patients in Sweden," *Resuscitation*, vol. 44, no. 1, pp. 7–17, Mar. 2000, doi: 10.1016/S0300-9572(99)00155-0.

[4] D. Ludhwani, A. Goyal, and M. Jagtap, "Ventricular Fibrillation," in *StatPearls*, StatPearls Publishing, 2020.

[5] B. A. Koplan and W. G. Stevenson, "Ventricular tachycardia and sudden cardiac death," in *Mayo Clinic Proceedings*, Mar. 2009, vol. 84, no. 3, pp. 289–297, doi: 10.4065/84.3.289.

[6] J. W. Dean and M. J. Lab, "Arrhythmia in Heart Failure: Role of Mechanically Induced Changes in Electrophysiology," *The Lancet*, vol. 333, no. 8650. Elsevier, pp. 1309–1312, Jun. 10, 1989, doi: 10.1016/S0140-6736(89)92697-4.

[7] R. Coronel, R. Wilders, A. O. Verkerk, R. F. Wiegerinck, D. Benoist, and O. Bernus, "Electrophysiological changes in heart failure and their implications for arrhythmogenesis," *Biochimica et Biophysica Acta - Molecular Basis of Disease*, vol. 1832, no. 12. Elsevier, pp. 2432–2441, Dec. 01, 2013, doi: 10.1016/j.bbadis.2013.04.002.

[8] E. Dupont *et al.*, "Altered connexin expression in human congestive heart failure," *J. Mol. Cell. Cardiol.*, vol. 33, no. 2, pp. 359–371, Feb. 2001, doi: 10.1006/jmcc.2000.1308.

[9] D. Mele, M. Nardozza, and R. Ferrari, “Left ventricular ejection fraction and heart failure: an indissoluble marriage?,” *Eur. J. Heart Fail.*, vol. 20, no. 3, pp. 427–430, Mar. 2018, doi: 10.1002/ejhf.1071.

[10] B. D. Westenbrink, J. J. Brugts, T. A. McDonagh, G. Filippatos, F. Ruschitzka, and L. W. van Laake, “Heart failure specialization in Europe,” *Eur. J. Heart Fail.*, vol. 18, no. 4, pp. 347–349, Apr. 2016, doi: 10.1002/ejhf.506.

[11] A. L. Clark, K. Goode, and J. G. F. Cleland, “The prevalence and incidence of left bundle branch block in ambulant patients with chronic heart failure,” *Eur. J. Heart Fail.*, vol. 10, no. 7, pp. 696–702, Jul. 2008, doi: 10.1016/j.ejheart.2008.05.001.

[12] H. B. Rao, R. Krishnaswami, S. Kalavakolanu, and N. Calambur, “Ventricular dyssynchrony patterns in left bundle branch block, with and without heart failure.,” *Indian Pacing Electrophysiol. J.*, vol. 10, no. 3, pp. 115–21, Mar. 2010, Accessed: Sep. 16, 2020. [Online]. Available: http://www.ncbi.nlm.nih.gov/pubmed/20234808.

[13] A. Sami, M. F. Iftekhar, I. Khan, and R. Jan, “Intraventricular dyssynchrony among patients with left bundle branch block,” *Pakistan J. Med. Sci.*, vol. 34, no. 2, pp. 390–392, Mar. 2018, doi: 10.12669/pjms.342.14103.

[14] S. Baldasseroni *et al.*, “Left bundle-branch block is associated with increased 1-year sudden and total mortality rate in 5517 outpatients with congestive heart failure: A report from the Italian Network on Congestive Heart Failure,” *Am. Heart J.*, vol. 143, no. 3, pp. 398–405, Mar. 2002, doi: 10.1067/mhj.2002.121264.

[15] E. Huvelle, R. Fay, F. Alla, A. Cohen Solal, A. Mebazaa, and F. Zannad, “Left bundle branch block and mortality in patients with acute heart failure syndrome: A substudy of the EFICA cohort,” *Eur. J. Heart Fail.*, vol. 12, no. 2, pp. 156–163, Feb. 2010, doi: 10.1093/eurjhf/hfp180.

[16] S. Yamashita *et al.*, “The effectiveness of cardiac

resynchronization therapy for patients with New York Heart Association class IV non-ambulatory heart failure," *J. Arrhythmia*, vol. 31, no. 4, pp. 221–225, Aug. 2015, doi: 10.1016/j.joa.2014.12.008.

[17] J. G. F. Cleland *et al.*, "The Effect of Cardiac Resynchronization on Morbidity and Mortality in Heart Failure," *N. Engl. J. Med.*, vol. 352, no. 15, pp. 1539–1549, Apr. 2005, doi: 10.1056/NEJMoa050496.

[18] J. Osmanska, N. M. Hawkins, M. Toma, A. Ignaszewski, and S. A. Virani, "Eligibility for cardiac resynchronization therapy in patients hospitalized with heart failure," *ESC Hear. Fail.*, vol. 5, no. 4, pp. 668–674, Aug. 2018, doi: 10.1002/ehf2.12297.

[19] C. Linde, K. Ellenbogen, and F. A. McAlister, "Cardiac resynchronization therapy (CRT): Clinical trials, guidelines, and target populations," *Hear. Rhythm*, vol. 9, no. 8 SUPPL., p. S3, Aug. 2012, doi: 10.1016/j.hrthm.2012.04.026.

[20] N. Varma, M. Manne, D. Nguyen, J. He, M. Niebauer, and P. Tchou, "Probability and magnitude of response to cardiac resynchronization therapy according to QRS duration and gender in nonischemic cardiomyopathy and LBBB," *Hear. Rhythm*, vol. 11, no. 7, pp. 1139–1147, Jul. 2014, doi: 10.1016/j.hrthm.2014.04.001.

[21] M. Noguchi *et al.*, "Delayed right ventricular defibrillation lead perforation presenting as cardiac tamponade and treated surgically," *Clin. Case Reports*, vol. 5, no. 4, pp. 458–462, Apr. 2017, doi: 10.1002/ccr3.865.

[22] A. Ghani *et al.*, "Incidence of lead dislodgement, malfunction and perforation during the first year following device implantation," *Netherlands Hear. J.*, vol. 22, no. 6, pp. 286–291, May 2014, doi: 10.1007/s12471-014-0556-6.

[23] M. A. Akbarzadeh, R. Mollazadeh, S. Sefidbakht, S. Shahrzad, and N. Bahrololoumi Bafruee, "Identification and management of right ventricular perforation using pacemaker and cardioverter-defibrillator leads: A case series and mini review,"

J. Arrhythmia, vol. 33, no. 1, pp. 1–5, Feb. 2017, doi: 10.1016/j.joa.2016.05.005.

[24] M. J. Janse and A. L. Wit, "Electrophysiological mechanisms of ventricular arrhythmias resulting from myocardial ischemia and infarction," *Physiological Reviews*, vol. 69, no. 4. American Physiological Society Bethesda, MD , pp. 1049–1169, 1989, doi: 10.1152/physrev.1989.69.4.1049.

[25] H. Moréna, M. J. Janse, J. W. Fiolet, W. J. Krieger, H. Crijns, and D. Durrer, "Comparison of the effects of regional ischemia, hypoxia, hyperkalemia, and acidosis on intracellular and extracellular potentials and metabolism in the isolated porcine heart.," *Circ. Res.*, vol. 46, no. 5, pp. 634–646, May 1980, doi: 10.1161/01.RES.46.5.634.

[26] I. Kodama, A. Wilde, M. J. Janse, D. Durrer, and K. Yamada, "Combined effects of hypoxia, hyperkalemia and acidosis on membrane action potential and excitability of guinea-pig ventricular muscle," *J. Mol. Cell. Cardiol.*, vol. 16, no. 3, pp. 247–259, 1984, doi: 10.1016/S0022-2828(84)80591-X.

[27] M. J. Janse, A. G. Kleber, A. Capucci, R. Coronel, and F. Wilms-Schopman, "Electrophysiological basis for arrhythmias caused by acute ischemia. Role of the subendocardium," *J. Mol. Cell. Cardiol.*, vol. 18, no. 4, pp. 339–355, Apr. 1986, doi: 10.1016/S0022-2828(86)80898-7.

[28] R. L. Wilensky, J. Tranum-Jensen, R. Coronel, A. A. Wilde, J. W. Fiolet, and M. J. Janse, "The subendocardial border zone during acute ischemia of the rabbit heart: an electrophysiologic, metabolic, and morphologic correlative study.," *Circulation*, vol. 74, no. 5, pp. 1137–1146, Nov. 1986, doi: 10.1161/01.CIR.74.5.1137.

[29] C. Livia *et al.*, "Elimination of Purkinje Fibers by Electroporation Reduces Ventricular Fibrillation Vulnerability," *J. Am. Heart Assoc.*, vol. 7, no. 15, p. e009070, Aug. 2018, doi: 10.1161/JAHA.118.009070.

[30] Y. M. Cha *et al.*, "Effects of chemical subendocardial ablation

on activation rate gradient during ventricular fibrillation," *Am. J. Physiol. - Hear. Circ. Physiol.*, vol. 269, no. 6, pp. H1998–H2009, 1995, doi: 10.1152/ajpheart.1995.269.6.h1998.

[31] A. Carusi, K. Burrage, and B. Rodríguez, "Bridging experiments, models and simulations: an integrative approach to validation in computational cardiac electrophysiology," *Am. J. Physiol. Circ. Physiol.*, vol. 303, no. 2, pp. H144–H155, Jul. 2012, doi: 10.1152/ajpheart.01151.2011.

[32] B. Rodriguez, N. Trayanova, and D. Noble, "Modeling Cardiac Ischemia," *Ann. N. Y. Acad. Sci.*, vol. 1080, no. 1, pp. 395–414, Oct. 2006, doi: 10.1196/annals.1380.029.

[33] J. M. Ferrero, B. Trenor, and L. Romero, "Multiscale computational analysis of the bioelectric consequences of myocardial ischaemia and infarction," *Europace*, vol. 16, no. 3. Oxford University Press, pp. 405–415, Mar. 01, 2014, doi: 10.1093/europace/eut405.

[34] A. M. Tobar, J. M. Ferrero, F. Migliavacca, and J. F. Rodríguez Matas, "Vulnerability in regionally ischemic human heart. Effect of the extracellular potassium concentration," *J. Comput. Sci.*, vol. 24, pp. 160–168, Jan. 2018, doi: 10.1016/j.jocs.2017.11.009.

[35] S. Dutta, A. Mincholé, E. Zacur, T. A. Quinn, P. Taggart, and B. Rodriguez, "Early afterdepolarizations promote transmural reentry in ischemic human ventricles with reduced repolarization reserve," *Prog. Biophys. Mol. Biol.*, vol. 120, no. 1–3, pp. 236–248, Jan. 2016, doi: 10.1016/j.pbiomolbio.2016.01.008.

[36] K. H. W. J. Ten Tusscher, D. Noble, P. J. Noble, and A. V. Panfilov, "A model for human ventricular tissue," *Am. J. Physiol. - Hear. Circ. Physiol.*, vol. 286, no. 4 55-4, pp. 1573–1589, 2004, doi: 10.1152/ajpheart.00794.2003.

[37] T. O'Hara, L. Virág, A. Varró, and Y. Rudy, "Simulation of the Undiseased Human Cardiac Ventricular Action Potential: Model Formulation and Experimental Validation," *PLoS Comput. Biol.*, vol. 7, no. 5, p. e1002061, May 2011, doi: 10.1371/journal.pcbi.1002061.

[38] J. Tomek *et al.*, "Development, calibration, and validation of a novel human ventricular myocyte model in health, disease, and drug block," *Elife*, vol. 8, Dec. 2019, doi: 10.7554/eLife.48890.

[39] G. J. Tortora and B. Derrickson, *Principles of Anatomy and Physiology*, 14th Edition. John Wiley & Sons, 2014.

[40] J. G. Betts *et al.*, *Anatomy and Physiology*. Houston, Texas: OpenStax, 2013.

[41] A. Kennedy, D. D. Finlay, D. Guldenring, R. Bond, K. Moran, and J. McLaughlin, "The Cardiac Conduction System: Generation and Conduction of the Cardiac Impulse," *Critical Care Nursing Clinics of North America*, vol. 28, no. 3. W.B. Saunders, pp. 269–279, Sep. 01, 2016, doi: 10.1016/j.cnc.2016.04.001.

[42] P. A. Iaizzo, *Handbook of cardiac anatomy, physiology, and devices: Second edition*. Humana Press, 2005.

[43] F. Saremi, M. Torrone, and N. Yashar, "Cardiac conduction system: delineation of anatomic landmarks with multidetector CT," *Indian Pacing and Electrophysiology Journal*, vol. 9, no. 6. Elsevier, pp. 318–333, 2009, Accessed: Sep. 14, 2020. [Online]. Available: www.ipej.org318.

[44] D. Sánchez-Quintana and S. Yen Ho, "Anatomy of Cardiac Nodes and Atrioventricular Specialized Conduction System," *Rev. Española Cardiol. (English Ed.*, vol. 56, no. 11, pp. 1085–1092, Nov. 2003, Accessed: Sep. 14, 2020. [Online]. Available: http://www.revespcardiol.org/en-anatomy-of-cardiac-nodes-and-articulo-13054060.

[45] P. Ganesan, M. Sterling, S. Ladavich, and B. Ghoraani, "Computer-Aided Clinical Decision Support Systems for Atrial Fibrillation," in *Computer-aided Technologies*, R. Udroiu, Ed. Rijeka: IntechOpen, 2016.

[46] L. Dux-Santoy, J. F. Rodriguez, R. Sebastian, J. Saiz, and J. M. Ferrero, "Biophysical modelling of bundle branch reentry initiation and maintenance," in *2012 Computing in Cardiology*, 2012, pp. 221–224.

[47] D. Durrer, R. T. Van Dam, G. E. Freud, M. J. Janse, F. L. Meijler, and R. C. Arzbaecher, "Total Excitation of the Isolated Human Heart," *Circulation*, vol. 41, no. 6, pp. 899–912, Jun. 1970, doi: 10.1161/01.CIR.41.6.899.

[48] P. Taggart *et al.*, "Inhomogeneous Transmural Conduction During Early Ischaemia in Patients with Coronary Artery Disease," *J Mol Cell Cardiol*, vol. 32, pp. 621–630, 2000, doi: 10.1006/jmcc.2000.1105.

[49] J. Feher, "The Cardiac Action Potential," in *Quantitative Human Physiology*, Elsevier, 2012, pp. 458–466.

[50] J. M. Nerbonne and R. S. Kass, "Molecular physiology of cardiac repolarization," *Physiological Reviews*, vol. 85, no. 4. American Physiological Society, pp. 1205–1253, Oct. 2005, doi: 10.1152/physrev.00002.2005.

[51] Z. Qu, M. B. Liu, and M. Nivala, "A unified theory of calcium alternans in ventricular myocytes," *Sci. Rep.*, vol. 6, no. 1, pp. 1–14, Oct. 2016, doi: 10.1038/srep35625.

[52] M. Renganathan, H. Wei, and Y. Zhao, "Cardiac Action Potential Measurement in Human Embryonic Stem Cell Cardiomyocytes for Cardiac Safety Studies Using Manual Patch-Clamp Electrophysiology," in *Methods in Pharmacology and Toxicology*, Humana Press, New York, NY, 2017, pp. 37–56.

[53] A. G. Kléber, M. J. Janse, and V. G. Fast, "Normal and Abnormal Conduction in the Heart," in *Comprehensive Physiology*, Hoboken, NJ, USA: John Wiley & Sons, Inc., 2011, pp. 455–530.

[54] J. M. Bote, J. Recas, F. Rincon, D. Atienza, and R. Hermida, "A Modular Low-Complexity ECG Delineation Algorithm for Real-Time Embedded Systems," *IEEE J. Biomed. Heal. Informatics*, vol. 22, no. 2, pp. 429–441, Mar. 2018, doi: 10.1109/JBHI.2017.2671443.

[55] P. Dilaveris, V. Batchvarov, J. Gialafos, and M. Malik, "Comparison of Different Methods for Manual P Wave Duration Measurement in 12-Lead Electrocardiograms," *Pacing Clin.*

Electrophysiol., vol. 22, no. 10, pp. 1532–1538, Oct. 1999, doi: 10.1111/j.1540-8159.1999.tb00358.x.

[56] S. Mahendrappa and T. Sathyanarayana, "The normal variations in heart rate and QRS complex of healthy individuals in different age groups," *Int. J. Res. Med. Sci.*, vol. 2, no. 3, pp. 861–865, Jan. 2014, doi: 10.5455/2320-6012.ijrms20140821.

[57] J. Wu, J. A. Kors, P. R. Rijnbeek, G. Van Herpen, Z. Lu, and C. Xu, "Normal limits of the electrocardiogram in Chinese subjects," *Int. J. Cardiol.*, vol. 87, no. 1, pp. 37–51, Jan. 2003, doi: 10.1016/S0167-5273(02)00248-6.

[58] E. W. Hancock, B. J. Deal, D. M. Mirvis, P. Okin, P. Kligfield, and L. S. Gettes, "AHA/ACCF/HRS recommendations for the standardization and interpretation of the electrocardiogram: Part V: Electrocardiogram changes associated with cardiac chamber hypertrophy: A scientific statement from the American Heart Association Electrocardiography and Arrhythmias Committee, Council on Clinical Cardiology; The American College of Cardiology Foundation; And the Heart Rhythm Society," *Circulation*, vol. 119, no. 10. Lippincott Williams & Wilkins, Mar. 17, 2009, doi: 10.1161/CIRCULATIONAHA.108.191097.

[59] M. P. Andersen *et al.*, "The ST injury vector: electrocardiogram-based estimation of location and extent of myocardial ischemia," *J. Electrocardiol.*, vol. 43, no. 2, pp. 121–131, Mar. 2010, doi: 10.1016/j.jelectrocard.2009.12.001.

[60] J. E. Gaxiola-Sosa, N. Mohsin, A. J. Palliyali, R. Tafreshi, and K. Entesari, "A portable 12-lead ECG wireless medical system for continuous cardiac-activity monitoring," in *Middle East Conference on Biomedical Engineering, MECBME*, 2014, pp. 123–126, doi: 10.1109/MECBME.2014.6783221.

[61] M. Romanò, *Text Atlas of Practical Electrocardiography*. Springer Milan, 2015.

[62] A. L. Hodgkin and A. F. Huxley, "Currents carried by sodium and potassium ions through the membrane of the giant axon of Loligo," *J. Physiol.*, vol. 116, no. 4, pp. 449–472, Apr. 1952, doi:

10.1113/jphysiol.1952.sp004717.

[63] C. H. Luo and Y. Rudy, “A dynamic model of the cardiac ventricular action potential. I. Simulations of ionic currents and concentration changes.,” *Circ. Res.*, vol. 74, no. 6, pp. 1071–1096, Jun. 1994, doi: 10.1161/01.RES.74.6.1071.

[64] L. Priebe and D. J. Beuckelmann, “Simulation Study of Cellular Electric Properties in Heart Failure,” *Circ. Res.*, vol. 82, no. 11, pp. 1206–1223, Jun. 1998, doi: 10.1161/01.RES.82.11.1206.

[65] E. Grandi, F. S. Pasqualini, and D. M. Bers, “A novel computational model of the human ventricular action potential and Ca transient,” *J. Mol. Cell. Cardiol.*, vol. 48, no. 1, pp. 112–121, Jan. 2010, doi: 10.1016/j.yjmcc.2009.09.019.

[66] J. Carro, J. F. Rodríguez, P. Laguna, and E. Pueyo, “A human ventricular cell model for investigation of cardiac arrhythmias under hyperkalaemic conditions,” *Philos. Trans. R. Soc. A Math. Phys. Eng. Sci.*, vol. 369, no. 1954, pp. 4205–4232, Nov. 2011, doi: 10.1098/rsta.2011.0127.

[67] Y. Wang and J. A. Hill, “Electrophysiological remodeling in heart failure,” *Journal of Molecular and Cellular Cardiology*. 2010, doi: 10.1016/j.yjmcc.2010.01.009.

[68] M. Luu, W. G. Stevenson, L. W. Stevenson, K. Baron, and J. Walden, “Diverse mechanisms of unexpected cardiac arrest in advanced heart failure.,” *Circulation*, vol. 80, no. 6, pp. 1675–1680, Dec. 1989, doi: 10.1161/01.CIR.80.6.1675.

[69] M. J. Janse, “Electrophysiological changes in heart failure and their relationship to arrhythmogenesis,” *Cardiovascular Research*, vol. 61, no. 2. Oxford Academic, pp. 208–217, Feb. 01, 2004, doi: 10.1016/j.cardiores.2003.11.018.

[70] R. B. de M. Barretto *et al.*, “Mechanical dyssynchrony is similar in different patterns of left bundle-branch block,” *Arq. Bras. Cardiol.*, vol. 101, no. 5, pp. 449–456, Nov. 2013, doi: 10.5935/abc.20130190.

[71] E. Surkova *et al.*, “Left bundle branch block: From cardiac

mechanics to clinical and diagnostic challenges," *Europace*, vol. 19, no. 8. Oxford University Press, pp. 1251–1271, Aug. 01, 2017, doi: 10.1093/europace/eux061.

[72] M. Potse, D. Krause, L. Bacharova, R. Krause, F. W. Prinzen, and A. Auricchio, "Similarities and differences between electrocardiogram signs of left bundle-branch block and left-ventricular uncoupling," *Europace*, vol. 14, no. SUPPL. 5, pp. v33–v39, Nov. 2012, doi: 10.1093/europace/eus272.

[73] D. G. Strauss, R. H. Selvester, and G. S. Wagner, "Defining left bundle branch block in the era of cardiac resynchronization therapy," *American Journal of Cardiology*, vol. 107, no. 6. Elsevier, pp. 927–934, Mar. 15, 2011, doi: 10.1016/j.amjcard.2010.11.010.

[74] G. B. Bleeker *et al.*, "Relationship between QRS duration and left ventricular dyssynchrony in patients with end-stage heart failure," *J. Cardiovasc. Electrophysiol.*, vol. 15, no. 5, pp. 544–549, May 2004, doi: 10.1046/j.1540-8167.2004.03604.x.

[75] F. G. Cosío, J. Palacios, A. Pastor, and A. Núñez, "The Electrocardiogram," in *The ESC Textbook of Cardiovascular Medicine*, 2nd Edition., no. November, Oxford, UK: Oxford University Press, 2009, pp. 29–82.

[76] B. Surawicz, R. Childers, B. J. Deal, and L. S. Gettes, "AHA/ACCF/HRS recommendations for the standardization and interpretation of the electrocardiogram: Part III: Intraventricular conduction disturbances: A scientific statement from the American Heart Association Electrocardiography and Arrhythmias Committee, Council on Clinical Cardiology; The American College of Cardiology Foundation; And the Heart Rhythm Society," *Circulation*, vol. 119, no. 10. Lippincott Williams & Wilkins, Mar. 17, 2009, doi: 10.1161/CIRCULATIONAHA.108.191095.

[77] C. J. M. Van Deursen *et al.*, "The value of the 12-lead ECG for evaluation and optimization of cardiac resynchronization therapy in daily clinical practice," in *Journal of Electrocardiology*, Mar. 2014, vol. 47, no. 2, pp. 202–211, doi:

10.1016/j.jelectrocard.2014.01.007.

[78] M. S. Turner *et al.*, "Electrical and mechanical components of dyssynchrony in heart failure patients with normal QRS duration and left bundle-branch block: Impact of left and biventricular pacing," *Circulation*, vol. 109, no. 21, pp. 2544–2549, Jun. 2004, doi: 10.1161/01.CIR.0000131184.40893.40.

[79] P. Dilaveris *et al.*, "Comparison of left ventricular and biventricular pacing: Rationale and clinical implications," *Anatolian Journal of Cardiology*, vol. 22, no. 3. Turkish Society of Cardiology, pp. 132–139, 2019, doi: 10.14744/AnatolJCardiol.2019.35006.

[80] M. Brignole *et al.*, "2013 ESC Guidelines on cardiac pacing and cardiac resynchronization therapy," *European Heart Journal*, vol. 34, no. 29. Oxford University Press, pp. 2281–2329, Aug. 01, 2013, doi: 10.1093/eurheartj/eht150.

[81] S. P. Sharma, K. Dahal, P. Dominic, and R. S. Sangha, "Clinical and echocardiographic response of apical vs nonapical right ventricular lead position in CRT: A meta-analysis," *J. Arrhythmia*, vol. 34, no. 2, pp. 185–194, Apr. 2018, doi: 10.1002/joa3.12041.

[82] K. T. Lappegård, H. Bjørnstad, T. E. Mollnes, and A. Hovland, "Effect of Cardiac Resynchronization Therapy on Inflammation in Congestive Heart Failure: A Review," *Scand. J. Immunol.*, vol. 82, no. 3, pp. 191–198, Sep. 2015, doi: 10.1111/sji.12328.

[83] G. Coppola *et al.*, "Magnitude of QRS duration reduction after biventricular pacing identifies responders to cardiac resynchronization therapy," *Int. J. Cardiol.*, vol. 221, pp. 450–455, Oct. 2016, doi: 10.1016/j.ijcard.2016.06.203.

[84] H. R. Bonakdar *et al.*, "Prediction of response to cardiac resynchronization therapy using simple electrocardiographic and echocardiographic tools," *Europace*, vol. 11, no. 10, pp. 1330–1337, Oct. 2009, doi: 10.1093/europace/eup258.

[85] J. G. Cleland *et al.*, "An individual patient meta-analysis of five randomized trials assessing the effects of cardiac

resynchronization therapy on morbidity and mortality in patients with symptomatic heart failure," *Eur. Heart J.*, vol. 34, no. 46, pp. 3547–3556, Dec. 2013, doi: 10.1093/eurheartj/eht290.

[86] P. C. Rezende, F. F. Ribas, C. V. Serrano, and W. Hueb, "Clinical significance of chronic myocardial ischemia in coronary artery disease patients," *Journal of Thoracic Disease*, vol. 11, no. 3. AME Publishing Company, pp. 1005–1015, 2019, doi: 10.21037/jtd.2019.02.85.

[87] T. Kalogeris, C. P. Baines, M. Krenz, and R. J. Korthuis, "Cell Biology of Ischemia/Reperfusion Injury," in *International Review of Cell and Molecular Biology*, vol. 298, Elsevier Inc., 2012, pp. 229–317.

[88] K. Thygesen *et al.*, "Fourth Universal Definition of Myocardial Infarction (2018)," *J. Am. Coll. Cardiol.*, vol. 72, no. 18, pp. 2231–2264, Oct. 2018, doi: 10.1016/j.jacc.2018.08.1038.

[89] L. S. Lilly and Harvard Medical School, *Pathophysiology of Heart Disease: A collaborative Project of Medical Students and Faculty*. Wolters Kluwer, 2016.

[90] E. Carmeliet, "Cardiac ionic currents and acute ischemia: From channels to arrhythmias," *Physiological Reviews*, vol. 79, no. 3. American Physiological Society, pp. 917–1017, 1999, doi: 10.1152/physrev.1999.79.3.917.

[91] M. J. Janse, R. Coronel, F. J. G. Wilms-Schopman, and J. R. De Groot, "Mechanical effects on arrhythmogenesis: From pipette to patient," in *Progress in Biophysics and Molecular Biology*, May 2003, vol. 82, no. 1–3, pp. 187–195, doi: 10.1016/S0079-6107(03)00015-4.

[92] S. M. Pogwizd and P. B. Corr, "Reentrant and nonreentrant mechanisms contribute to arrhythmogenesis during early myocardial ischemia: results using three-dimensional mapping.," *Circ. Res.*, vol. 61, no. 3, pp. 352–371, Sep. 1987, doi: 10.1161/01.RES.61.3.352.

[93] E. Kaplinsky, S. Ogawa, C. W. Balke, and L. S. Dreifus, "Two periods of early ventricular arrhythmia in the canine acute

myocardial infarction model.," *Circulation*, vol. 60, no. 2, pp. 397–403, Aug. 1979, doi: 10.1161/01.CIR.60.2.397.

[94] W. E. Cascio, "Myocardial Ischemia: What Factors Determine Arrhythmogenesis?," *J. Cardiovasc. Electrophysiol.*, vol. 12, no. 6, pp. 726–729, Jun. 2001, doi: 10.1046/j.1540-8167.2001.00726.x.

[95] A. B. Chicos and A. H. Kadish, "Arrhythmias in Coronary Artery Disease," in *Electrophysiological Disorders of the Heart*, 2nd Edition., Saunders, 2012, pp. 825–834.

[96] F. M. McDonald *et al.*, "Acute myocardial ischaemia in the anaesthetised pig: local catecholamine release and its relation to ventricular fibrillation," *Basic Res. Cardiol.*, vol. 81, no. 6, pp. 636–645, Nov. 1986, doi: 10.1007/BF02005187.

[97] W. T. Smith, W. F. Fleet, T. A. Johnson, C. L. Engle, and W. E. Cascio, "The Ib Phase of Ventricular Arrhythmias in Ischemic In Situ Porcine Heart Is Related to Changes in Cell-to-Cell Electrical Coupling," *Circulation*, vol. 92, no. 10, pp. 3051–3060, Nov. 1995, doi: 10.1161/01.CIR.92.10.3051.

[98] J. L. Hill and L. S. Gettes, "Effect of acute coronary artery occlusion on local myocardial extracellular K^+ activity in swine.," *Circulation*, vol. 61, no. 4, pp. 768–778, Apr. 1980, doi: 10.1161/01.CIR.61.4.768.

[99] G. X. Yan and A. G. Kléber, "Changes in extracellular and intracellular pH in ischemic rabbit papillary muscle.," *Circ. Res.*, vol. 71, no. 2, pp. 460–470, Aug. 1992, doi: 10.1161/01.RES.71.2.460.

[100] R. Coronel, F. J. G. Wilms-Schopman, J. W. T. Fiolet, T. Opthof, and M. J. Janse, "The relation between extracellular potassium concentration and pH in the border zone during regional ischemia in isolated porcine hearts," *J. Mol. Cell. Cardiol.*, vol. 27, no. 9, pp. 2069–2073, Sep. 1995, doi: 10.1016/0022-2828(95)90028-4.

[101] J. N. Weiss, N. Venkatesh, and S. T. Lamp, "ATP-sensitive K^+ channels and cellular K^+ loss in hypoxic and ischaemic

mammalian ventricle.," *J. Physiol.*, vol. 447, no. 1, pp. 649–673, Feb. 1992, doi: 10.1113/jphysiol.1992.sp019022.

[102] K. A. Reimer, C. E. Murry, I. Yamasawa, M. L. Hill, and R. B. Jennings, "Four brief periods of myocardial ischemia cause no cumulative ATP loss or necrosis," *Am. J. Physiol. - Hear. Circ. Physiol.*, vol. 251, no. 6 (20/6), 1986, doi: 10.1152/ajpheart.1986.251.6.h1306.

[103] J. Weiss and K. I. Shine, "Extracellular potassium accumulation during myocardial ischemia: Implications for arrhythmogenesis," *J. Mol. Cell. Cardiol.*, vol. 13, no. 7, pp. 699–704, Jul. 1981, doi: 10.1016/0022-2828(81)90277-7.

[104] C. L. Watson and M. R. Gold, "Effect of intracellular and extracellular acidosis on sodium current in ventricular myocytes," *Am. J. Physiol.*, vol. 268, no. 4, pp. H1749–H1756, 1995, doi: 10.1152/ajpheart.1995.268.4.H1749.

[105] N. Saegusa, E. Moorhouse, R. D. Vaughan-Jones, and K. W. Spitzer, "Influence of pH on Ca^{2+} current and its control of electrical and Ca^{2+} signaling in ventricular myocytes," *J. Gen. Physiol.*, vol. 138, no. 5, pp. 537–559, Nov. 2011, doi: 10.1085/jgp.201110658.

[106] R. Mohabir, H. C. Lee, R. W. Kurz, and W. T. Clusin, "Effects of ischemia and hypercarbic acidosis on myocyte calcium transients, contraction, and pHi in perfused rabbit hearts.," *Circ. Res.*, vol. 69, no. 6, pp. 1525–1537, Dec. 1991, doi: 10.1161/01.RES.69.6.1525.

[107] P. B. Garlick, G. K. Radda, and P. J. Seeley, "Studies of acidosis in the ischaemic heart by phosphorus nuclear magnetic resonance," *Biochem. J.*, vol. 184, no. 3, pp. 547–554, Dec. 1979, doi: 10.1042/bj1840547.

[108] W. F. Fleet, T. A. Johnson, C. A. Graebner, and L. S. Gettes, "Effect of serial brief ischemic episodes on extracellular K+, pH, and activation in the pig.," *Circulation*, vol. 72, no. 4, pp. 922–932, Oct. 1985, doi: 10.1161/01.CIR.72.4.922.

[109] N. El-Sherif and J. Jalife, "Paroxysmal atrioventricular block:

Are phase 3 and phase 4 block mechanisms or misnomers?," *Hear. Rhythm*, vol. 6, no. 10, pp. 1514–1521, Oct. 2009, doi: 10.1016/j.hrthm.2009.06.025.

[110] A. G. Kléber, "Resting membrane potential, extracellular potassium activity, and intracellular sodium activity during acute global ischemia in isolated perfused guinea pig hearts.," *Circ. Res.*, vol. 52, no. 4, pp. 442–450, Apr. 1983, doi: 10.1161/01.RES.52.4.442.

[111] R. N. Gasser and R. D. Vaughan-Jones, "Mechanism of potassium efflux and action potential shortening during ischaemia in isolated mammalian cardiac muscle.," *J. Physiol.*, vol. 431, no. 1, pp. 713–741, Dec. 1990, doi: 10.1113/jphysiol.1990.sp018356.

[112] M. J. Janse and A. G. Kléber, "Electrophysiological changes and ventricular arrhythmias in the early phase of regional myocardial ischemia.," *Circ. Res.*, vol. 49, no. 5, pp. 1069–1081, Nov. 1981, doi: 10.1161/01.RES.49.5.1069.

[113] R. Shaw, "Electrophysiologic effects of acute myocardial ischemia: a theoretical study of altered cell excitability and action potential duration," *Cardiovasc. Res.*, vol. 35, no. 2, pp. 256–272, Aug. 1997, doi: 10.1016/S0008-6363(97)00093-X.

[114] P. M. I. Sutton *et al.*, "Repolarisation and refractoriness during early ischaemia in humans," *Heart*, vol. 84, no. 4, pp. 365–369, Oct. 2000, doi: 10.1136/heart.84.4.365.

[115] Z. F. Issa, J. M. Miller, and D. P. Zipes, *Clinical Arrhytmology and Electrophysiology a Companion to Braunwald's Heart Disease*, 3rd Edition. Elsevier, 2018.

[116] R. Coronel, M. J. Janse, T. Opthof, A. A. Wilde, and P. Taggart, "Postrepolarization refractoriness in acute ischemia and after antiarrhythmic drug administration: Action potential duration is not always an index of the refractory period," *Hear. Rhythm*, vol. 9, no. 6, pp. 977–982, Jun. 2012, doi: 10.1016/j.hrthm.2012.01.021.

[117] M. A. Allessie, F. I. Bonke, and F. J. Schopman, "Circus

movement in rabbit atrial muscle as a mechanism of tachycardia. II. The role of nonuniform recovery of excitability in the occurrence of unidirectional block, as studied with multiple microelectrodes.," *Circ. Res.*, vol. 39, no. 2, pp. 168–177, Aug. 1976, doi: 10.1161/01.RES.39.2.168.

[118] J. M. Ferrero, J. Sáiz, J. M. Ferrero, and N. V. Thakor, "Simulation of Action Potentials From Metabolically Impaired Cardiac Myocytes," *Circ. Res.*, vol. 79, no. 2, pp. 208–221, Aug. 1996, doi: 10.1161/01.RES.79.2.208.

[119] K. Channer and F. Morris, "ABC of clinical electrocardiography: Myocardial ischaemia," *BMJ*, vol. 324, no. 7344, pp. 1023–1026, Apr. 2002, doi: 10.1136/bmj.324.7344.1023.

[120] M. Wilhelms, O. Dössel, and G. Seemann, "Comparing simulated electrocardiograms of different stages of acute cardiac ischemia," in *Lecture Notes in Computer Science (including subseries Lecture Notes in Artificial Intelligence and Lecture Notes in Bioinformatics)*, 2011, vol. 6666 LNCS, pp. 11–19, doi: 10.1007/978-3-642-21028-0_2.

[121] E. B. Hanna and D. L. Glancy, "ST-segment depression and T-wave inversion: Classification, differential diagnosis, and caveats," *Cleveland Clinic Journal of Medicine*, vol. 78, no. 6. Cleveland Clinic Journal of Medicine, pp. 404–414, Jun. 01, 2011, doi: 10.3949/ccjm.78a.10077.

[122] H. Martinez-Navarro, A. Mincholé, A. Bueno-Orovio, and B. Rodriguez, "High arrhythmic risk in antero-septal acute myocardial ischemia is explained by increased transmural reentry occurrence," *Sci. Rep.*, vol. 9, no. 1, pp. 1–12, Dec. 2019, doi: 10.1038/s41598-019-53221-2.

[123] B. Foster, *Twelve-Lead Electrocardiography*, 2nd Edition. Springer London, 2007.

[124] E. C. de Bliek, "ST elevation: Differential diagnosis and caveats. A comprehensive review to help distinguish ST elevation myocardial infarction from nonischemic etiologies of ST elevation," *Turkish J. Emerg. Med.*, vol. 18, no. 1, pp. 1–10, Mar.

2018, doi: 10.1016/j.tjem.2018.01.008.

[125] J. T. Levis, "ECG Diagnosis: Hyperacute T Waves," *Perm. J.*, vol. 19, no. 3, p. 79, Jun. 2015, doi: 10.7812/TPP/14-243.

[126] S. Nattel, "New ideas about atrial fibrillation 50 years on," *Nature*, vol. 415, no. 6868. Nature Publishing Group, pp. 219–226, Jan. 10, 2002, doi: 10.1038/415219a.

[127] E. M. A. Anas, S. Y. Lee, and M. K. Hasan, "Sequential algorithm for life threatening cardiac pathologies detection based on mean signal strength and EMD functions," *Biomed. Eng. Online*, vol. 9, no. 1, p. 43, Sep. 2010, doi: 10.1186/1475-925X-9-43.

[128] D. P. Zipes, "Mechanisms of Clinical Arrhythmias," *J. Cardiovasc. Electrophysiol.*, vol. 14, no. 8, pp. 902–912, Aug. 2003, doi: 10.1046/j.1540-8167.2003.03228.x.

[129] M. J. Janse *et al.*, "Flow of 'injury' current and patterns of excitation during early ventricular arrhythmias in acute regional myocardial ischemia in isolated porcine and canine hearts. Evidence for two different arrhythmogenic mechanisms.," *Circ. Res.*, vol. 47, no. 2, pp. 151–165, Aug. 1980, doi: 10.1161/01.RES.47.2.151.

[130] L. Gaztañaga, F. E. Marchlinski, and B. P. Betensky, "Mecanismos de las arritmias cardiacas," *Rev. Esp. Cardiol.*, vol. 65, no. 2, pp. 174–185, Feb. 2012, doi: 10.1016/j.recesp.2011.09.018.

[131] W. T. Abraham *et al.*, "Cardiac resynchronization in chronic heart failure," *N. Engl. J. Med.*, vol. 346, no. 24, pp. 1845–53, Jun. 2002, doi: 10.1056/NEJMoa013168.

[132] W. Zareba *et al.*, "Effectiveness of cardiac resynchronization therapy by QRS morphology in the multicenter automatic defibrillator implantation trial-cardiac resynchronization therapy (MADIT-CRT)," *Circulation*, vol. 123, no. 10, pp. 1061–1072, 2011, doi: 10.1161/CIRCULATIONAHA.110.960898.

[133] J. Zhang *et al.*, "QRS duration shortening predicts left ventricular

reverse remodelling in patients with dilated cardiomyopathy after cardiac resynchronization therapy," *Acta Cardiol.*, vol. 70, no. 3, pp. 307–313, Jun. 2015, doi: 10.1080/ac.70.3.3080635.

[134] E. Bertaglia *et al.*, "Stricter criteria for left bundle branch block diagnosis do not improve response to CRT," *PACE - Pacing Clin. Electrophysiol.*, 2017, doi: 10.1111/pace.13104.

[135] A. Crozier *et al.*, "The relative role of patient physiology and device optimisation in cardiac resynchronisation therapy: A computational modelling study," *Journal of Molecular and Cellular Cardiology*. 2016, doi: 10.1016/j.yjmcc.2015.10.026.

[136] A. W. C. Lee *et al.*, "Biophysical Modeling to Determine the Optimization of Left Ventricular Pacing Site and AV/VV Delays in the Acute and Chronic Phase of Cardiac Resynchronization Therapy," *J. Cardiovasc. Electrophysiol.*, 2017, doi: 10.1111/jce.13134.

[137] J. P. Singh *et al.*, "Left ventricular lead position and clinical outcome in the multicenter automatic defibrillator implantation trial-cardiac resynchronization therapy (MADIT-CRT) trial," *Circulation*, vol. 123, no. 11, pp. 1159–1166, 2011, doi: 10.1161/CIRCULATIONAHA.110.000646.

[138] A. Lopez-Perez, R. Sebastian, and J. M. Ferrero, "Three-dimensional cardiac computational modelling: METHODS, features and applications," *BioMedical Engineering Online*. 2015, doi: 10.1186/s12938-015-0033-5.

[139] A. Rossillo *et al.*, "Impact of coronary sinus lead position on biventricular pacing: Mortality and echocardiographic evaluation during long-term follow-up," *J. Cardiovasc. Electrophysiol.*, vol. 15, no. 10, pp. 1120–1125, 2004, doi: 10.1046/j.1540-8167.2004.04089.x.

[140] F. Zanon *et al.*, "Determination of the longest intrapatient left ventricular electrical delay may predict acute hemodynamic improvement in patients after cardiac resynchronization therapy," *Circ. Arrhythmia Electrophysiol.*, 2014, doi: 10.1161/CIRCEP.113.000850.

[141] A. Şipal *et al.*, "Surface electrogram-guided left ventricular lead placement improves response to cardiac resynchronization therapy," *Anatol J Cardiol*, vol. 19, no. 3, pp. 184–191, 2018, doi: 10.14744/AnatolJCardiol.2018.09216.

[142] M. Pluijmert, P. H. M. Bovendeerd, J. Lumens, K. Vernooy, F. W. Prinzen, and T. Delhaas, "New insights from a computational model on the relation between pacing site and CRT response," *Europace*, vol. 18, no. 4, pp. iv94–iv103, 2016, doi: 10.1093/europace/euw355.

[143] R. Miri, M. Reumann, D. Farina, and O. Dössel, "Concurrent optimization of timing delays and electrode positioning in biventricular pacing based on a computer heart model assuming 17 left ventricular segments," *Biomed. Tech.*, vol. 54, no. 2, pp. 55–65, 2009, doi: 10.1515/BMT.2009.013.

[144] R. Miri, I. M. Graf, and O. DÖssel, "Efficiency of timing delays and electrode positions in optimization of biventricular pacing: A simulation study," *IEEE Trans. Biomed. Eng.*, 2009, doi: 10.1109/TBME.2009.2027692.

[145] A. Da Costa *et al.*, "Focus on right ventricular outflow tract septal pacing," *Archives of Cardiovascular Diseases*. 2013, doi: 10.1016/j.acvd.2012.08.005.

[146] G. Pastore *et al.*, "How can we identify the optimal pacing site in the right ventricular septum? A simplified method applicable during the standard implanting procedure," *Am J Cardiovasc Dis*, vol. 3, no. 4, pp. 264–272, 2013.

[147] D. Gras, M. S. Gupta, E. Boulogne, L. Guzzo, and W. T. Abraham, "Optimization of AV and VV delays in the real-world CRT patient population: An international survey on current clinical practice," *PACE - Pacing Clin. Electrophysiol.*, vol. 32, no. SUPPL. 1, 2009, doi: 10.1111/j.1540-8159.2008.02294.x.

[148] W. T. Abraham, D. Gras, C. M. Yu, L. Guzzo, and M. S. Gupta, "Rationale and design of a randomized clinical trial to assess the safety and efficacy of frequent optimization of cardiac resynchronization therapy: The Frequent Optimization Study

Using the QuickOpt Method (FREEDOM) trial," *Am. Heart J.*, vol. 159, no. 6, pp. 944-948.e1, 2010, doi: 10.1016/j.ahj.2010.02.034.

[149] J. Brugada *et al.*, "Automatic Optimization of Cardiac Resynchronization Therapy Using SonR - Rationale and Design of the Clinical Trial of the SonRtip Lead and Automatic AV-VV Optimization Algorithm in the Paradym RF SonR CRT-D (RESPOND CRT) Trial," *Am. Heart J.*, vol. 167, no. 4, pp. 429–436, 2014, doi: 10.1016/j.ahj.2013.12.007.

[150] H. Krum *et al.*, "A novel algorithm for individualized cardiac resynchronization therapy: Rationale and design of the adaptive cardiac resynchronization therapy trial," *Am. Heart J.*, vol. 163, no. 5, pp. 747-752.e1, 2012, doi: 10.1016/j.ahj.2012.02.007.

[151] I. Ulč and V. Vančura, "Optimization of pacing intervals in cardiac resynchronization therapy," *Cor Vasa*, vol. 55, no. 5, pp. e403–e410, Oct. 2013, doi: 10.1016/j.crvasa.2013.06.001.

[152] E. Arbelo *et al.*, "Fusion-Optimized Intervals (FOI): A New Method to Achieve the Narrowest QRS for Optimization of the AV and VV Intervals in Patients Undergoing Cardiac Resynchronization Therapy," *284Journal Cardiovasc. Electrophysiol.*, vol. 25, pp. 283–292, 2014, doi: 10.1111/jce.12322.

[153] M. Bertini *et al.*, "Interventricular Delay Interval Optimization in Cardiac Resynchronization Therapy Guided by Echocardiography Versus Guided by Electrocardiographic QRS Interval Width," *Am. J. Cardiol.*, 2008, doi: 10.1016/j.amjcard.2008.07.015.

[154] D. Tamborero *et al.*, "Electrocardiographic versus echocardiographic optimization of the interventricular pacing delay in patients undergoing cardiac resynchronization therapy," *J. Cardiovasc. Electrophysiol.*, 2011, doi: 10.1111/j.1540-8167.2011.02085.x.

[155] CIBC, "Seg3D: Volumetric Image Segmentation and Visualization. Scientific Computing and Imaging Institute

(SCI).” 2016, [Online]. Available: http://www.seg3d.org.

[156] S. Sicouri and C. Antzelevitch, “A subpopulation of cells with unique electrophysiological properties in the deep subepicardium of the canine ventricle. The M cell.,” *Circ. Res.*, vol. 68, no. 6, pp. 1729–1741, Jun. 1991, doi: 10.1161/01.RES.68.6.1729.

[157] S. Sicouri, J. Fish, and C. Antzelevitch, “Distribution of M Cells in the Canine Ventricle,” *J. Cardiovasc. Electrophysiol.*, vol. 5, no. 10, pp. 824–837, Oct. 1994, doi: 10.1111/j.1540-8167.1994.tb01121.x.

[158] G.-X. Yan, W. Shimizu, and C. Antzelevitch, “Characteristics and Distribution of M Cells in Arterially Perfused Canine Left Ventricular Wedge Preparations,” *Circulation*, vol. 98, no. 18, pp. 1921–1927, Nov. 1998, doi: 10.1161/01.CIR.98.18.1921.

[159] D. D. Streeter, H. M. Spotnitz, D. P. Patel, J. Ross, and E. H. Sonnenblick, “Fiber Orientation in the Canine Left Ventricle during Diastole and Systole,” *Circ. Res.*, vol. 24, no. 3, pp. 339–347, Mar. 1969, doi: 10.1161/01.RES.24.3.339.

[160] R. Sebastian, V. Zimmerman, F. Sukno, B. B. Bijnens, and A. F. Frangi, “Cardiac modelling for pathophysiology research and clinical applications. The need for an automated pipeline,” *IFMBE Proc.*, vol. 25, no. 4, pp. 2207–2210, 2009, doi: 10.1007/978-3-642-03882-2-586.

[161] R. A. Greenbaum, S. Y. Ho, D. G. Gibson, A. E. Becker, and R. H. Anderson, “Left ventricular fibre architecture in man.,” *Heart*, vol. 45, no. 3, pp. 248–263, 1981, doi: 10.1136/hrt.45.3.248.

[162] R. Sebastian, V. Zimmerman, D. Romero, D. Sanchez-Quintana, and A. F. Frangi, “Characterization and modeling of the peripheral cardiac conduction system,” *IEEE Trans. Med. Imaging*, vol. 32, no. 1, pp. 45–55, 2013, doi: 10.1109/TMI.2012.2221474.

[163] A. Ferrer *et al.*, “Detailed Anatomical and Electrophysiological Models of Human Atria and Torso for the Simulation of Atrial

Activation," *PLoS One*, vol. 10, no. 11, p. e0141573, Nov. 2015, doi: 10.1371/journal.pone.0141573.

[164] R. S. MacLeod, C. R. Johnson, and P. R. Ershler, "Construction of an inhomogeneous model of the human torso for use in computational electrocardiography," *Proc. Annu. Conf. Eng. Med. Biol.*, vol. 13, pp. 688–689, 1991.

[165] A. J. Prassl *et al.*, "Automatically generated, anatomically accurate meshes for cardiac electrophysiology problems.," *IEEE Trans. Biomed. Eng.*, vol. 56, no. 5, pp. 1318–30, May 2009, doi: 10.1109/TBME.2009.2014243.

[166] E. Passini *et al.*, "Mechanisms of pro-arrhythmic abnormalities in ventricular repolarisation and anti-arrhythmic therapies in human hypertrophic cardiomyopathy," *J. Mol. Cell. Cardiol.*, 2016, doi: 10.1016/j.yjmcc.2015.09.003.

[167] M. T. Mora, J. M. Ferrero, L. Romero, and B. Trenor, "Sensitivity analysis revealing the effect of modulating ionic mechanisms on calcium dynamics in simulated human heart failure," *PLoS One*, 2017, doi: 10.1371/journal.pone.0187739.

[168] S. Dutta, A. Mincholé, T. A. Quinn, and B. Rodriguez, "Electrophysiological properties of computational human ventricular cell action potential models under acute ischemic conditions," *Progress in Biophysics and Molecular Biology*, vol. 129. Elsevier Ltd, pp. 40–52, Oct. 01, 2017, doi: 10.1016/j.pbiomolbio.2017.02.007.

[169] P. Stewart, O. V. Aslanidi, D. Noble, P. J. Noble, M. R. Boyett, and H. Zhang, "Mathematical models of the electrical action potential of Purkinje fibre cells," *Philos. Trans. R. Soc. A Math. Phys. Eng. Sci.*, vol. 367, no. 1896, pp. 2225–2255, Jun. 2009, doi: 10.1098/rsta.2008.0283.

[170] E. A. Heidenreich, J. M. Ferrero, M. Doblaré, and J. F. Rodríguez, "Adaptive macro finite elements for the numerical solution of monodomain equations in cardiac electrophysiology," *Ann. Biomed. Eng.*, vol. 38, no. 7, pp. 2331–2345, Jul. 2010, doi: 10.1007/s10439-010-9997-2.

[171] M. Potse, B. Dubé, J. Richer, A. Vinet, and R. M. Gulrajani, "A Comparison of Monodomain and Bidomain Reaction-Diffusion Models for Action Potential Propagation in the Human Heart," *IEEE Trans. Biomed. Eng.*, vol. 53, no. 12, 2006, doi: 10.1109/TBME.2006.880875.

[172] B. J. Roth, "How the anisotropy of the intracellular and extracellular conductivities influences stimulation of cardiac muscle," *J. Math. Biol.*, 1992, doi: 10.1007/BF00175610.

[173] C. P. Bradley, A. J. Pullan, and P. J. Hunter, "Geometric Modeling of the Human Torso Using Cubic Hermite Elements," *Ann. Biomed. Eng.*, vol. 25, pp. 96–11, 1997.

[174] D. U. J. Keller, F. M. Weber, G. Seemann, and O. Dössel, "Ranking the influence of tissue conductivities on forward-calculated ecgs," *IEEE Trans. Biomed. Eng.*, 2010, doi: 10.1109/TBME.2010.2046485.

[175] X. Ai and S. M. Pogwizd, "Connexin 43 downregulation and dephosphorylation in nonischemic heart failure is associated with enhanced colocalized protein phosphatase type 2A," *Circ. Res.*, 2005, doi: 10.1161/01.RES.0000152325.07495.5a.

[176] F. G. Akar *et al.*, "Dynamic changes in conduction velocity and gap junction properties during development of pacing-induced heart failure," *Am J Physiol Hear. Circ Physiol*, vol. 293, 2007, doi: 10.1152/ajpheart.00079.2007.-End.

[177] J. Rickard *et al.*, "Effect of PR interval prolongation on long-term outcomes in patients with left bundle branch block vs non–left bundle branch block morphologies undergoing cardiac resynchronization therapy," *Hear. Rhythm*, 2017, doi: 10.1016/j.hrthm.2017.05.028.

[178] F. W. Prinzen, K. Vernooy, J. Lumens, and A. Auricchio, "Physiology of Cardiac Pacing and Resynchronization," in *Clinical Cardiac Pacing, Defibrillation and Resynchronization Therapy*, 5th ed., K. A. Ellenbogen, B. L. Wilkoff, G. N. Kay, C.-P. Lau, and A. Auricchio, Eds. Philadelphia, PA: Elsevier, 2017, pp. 213–248.

[179] B. Urbanek *et al.*, "Potential benefit of optimizing atrioventricular & interventricular delays in patients with cardiac resynchronization therapy," *Indian J. Med. Res.*, 2017, doi: 10.4103/ijmr.IJMR_1560_14.

[180] J. Dou *et al.*, "A study of mechanical optimization strategy for cardiac resynchronization therapy based on an electromechanical model," *Comput. Math. Methods Med.*, 2012, doi: 10.1155/2012/948781.

[181] B. J. Boukens, M. R. Rivaud, S. Rentschler, and R. Coronel, "Misinterpretation of the mouse ECG: 'Musing the waves of Mus musculus,'" *Journal of Physiology*, vol. 592, no. 21. Blackwell Publishing Ltd, pp. 4613–4626, Nov. 01, 2014, doi: 10.1113/jphysiol.2014.279380.

[182] A. Auricchio *et al.*, "Characterization of Left Ventricular Activation in Patients with Heart Failure and Left Bundle-Branch Block," *Circulation*, 2004, doi: 10.1161/01.CIR.0000118502.91105.F6.

[183] M. Mafi Rad *et al.*, "Different regions of latest electrical activation during left bundle-branch block and right ventricular pacing in cardiac resynchronization therapy patients determined by coronary venous electro-anatomic mapping," *Eur. J. Heart Fail.*, 2014, doi: 10.1002/ejhf.178.

[184] D. D. Spragg *et al.*, "Optimal left ventricular endocardial pacing sites for cardiac resynchronization therapy in patients with ischemic cardiomyopathy," *J. Am. Coll. Cardiol.*, 2010, doi: 10.1016/j.jacc.2010.06.014.

[185] Y. Tian *et al.*, "Fragmented QRS complex in healthy adults: Prevalence, characteristics, mechanisms, and clinical implications," *Int. J. Hear. Rhythm*, vol. 2, no. 1, pp. 34–39, 2017, doi: 10.4103/2352-4197.208459.

[186] M. O. Sweeney, A. S. Hellkamp, R. J. Van Bommel, M. J. Schalij, C. Jan Willem Borleffs, and J. J. Bax, "QRS fusion complex analysis using wave interference to predict reverse remodeling during cardiac resynchronization therapy," *Hear.*

Rhythm, vol. 11, no. 5, pp. 806–813, May 2014, doi: 10.1016/j.hrthm.2014.01.021.

[187] I. A. Elhakam Elzoghby, I. Attia, A. El Azab, and M. Hammouda, "Impact of Cardiac Resynchronization Therapy on Heart Failure Patients: Experience from One Center," *Arch. Med.*, vol. 09, no. 04, pp. 1–7, 2017, doi: 10.21767/1989-5216.1000232.

[188] S. G. Molhoek *et al.*, "QRS duration and shortening to predict clinical response to cardiac resynchronization therapy in patients with end-stage heart failure.," *Pacing Clin. Electrophysiol.*, vol. 27, no. 3, pp. 308–313, 2004, doi: 10.1111/j.1540-8159.2004.00433.x.

[189] N. Derval *et al.*, "Optimizing Hemodynamics in Heart Failure Patients by Systematic Screening of Left Ventricular Pacing Sites. The Lateral Left Ventricular Wall and the Coronary Sinus Are Rarely the Best Sites," *J. Am. Coll. Cardiol.*, vol. 55, no. 6, pp. 566–575, 2010, doi: 10.1016/j.jacc.2009.08.045.

[190] H. Yoshikawa, M. Suzuki, N. Tezuka, T. Otsuka, and K. Sugi, "Differences in left ventricular dyssynchrony between high septal pacing and apical pacing in patients with normal left ventricular systolic function," *J. Cardiol.*, 2010, doi: 10.1016/j.jjcc.2010.02.002.

[191] A. Auricchio *et al.*, "Transvenous biventricular pacing for heart failure: Can the obstacles be overcome," *Am. J. Cardiol.*, vol. 83, no. 5 B, 1999, doi: 10.1016/S0002-9149(98)01015-7.

[192] J. P. Singh *et al.*, "Left ventricular lead electrical delay predicts response to cardiac resynchronization therapy," *Hear. Rhythm*, vol. 3, no. 11, pp. 1285–1292, 2006, doi: 10.1016/j.hrthm.2006.07.034.

[193] C. Stellbrink *et al.*, "Pacing therapies in congestive heart failure II study," *Am. J. Cardiol.*, vol. 86, no. 9 SUPPL. 1, pp. K138–K143, 2000, doi: 10.1016/S0002-9149(00)01298-4.

[194] O. Cano *et al.*, "Comparison of Effectiveness of Right Ventricular Septal Pacing Versus Right Ventricular Apical

Pacing," *Am. J. Cardiol.*, vol. 105, no. 10, pp. 1426–1432, 2010, doi: 10.1016/j.amjcard.2010.01.004.

[195] C. Muto *et al.*, "Effect of pacing the right ventricular mid-septum tract in patients with permanent atrial fibrillation and low ejection fraction," *J. Cardiovasc. Electrophysiol.*, vol. 18, no. 10, pp. 1032–1036, 2007, doi: 10.1111/j.1540-8167.2007.00914.x.

[196] P. Flevari *et al.*, "Long-term nonoutflow septal versus apical right ventricular pacing: Relation to left ventricular dyssynchrony," *PACE - Pacing Clin. Electrophysiol.*, vol. 32, no. 3, pp. 354–362, 2009, doi: 10.1111/j.1540-8159.2008.02244.x.

[197] C. Leclercq *et al.*, "Comparison of right ventricular septal pacing and right ventricular apical pacing in patients receiving cardiac resynchronization therapy defibrillators: The SEPTAL CRT Study," *Eur. Heart J.*, vol. 37, no. 5, pp. 473–483, 2016, doi: 10.1093/eurheartj/ehv422.

[198] F. Victor *et al.*, "A randomized comparison of permanent septal versus apical right ventricular pacing: Short-term results," *J. Cardiovasc. Electrophysiol.*, 2006, doi: 10.1111/j.1540-8167.2006.00358.x.

[199] A. Sommer *et al.*, "Longer inter-lead electrical delay is associated with response to cardiac resynchronization therapy in patients with presumed optimal left ventricular lead position," *EP Eur.*, no. January, pp. 1–8, 2018, doi: 10.1093/europace/eux384.

[200] S. Cazeau *et al.*, "Effects of multisite biventricular pacing in patients with heart failure and intraventricular conduction delay.," *N. Engl. J. Med.*, vol. 344, no. 12, pp. 873–80, Mar. 2001, doi: 10.1056/NEJM200103223441202.

[201] F. W. Prinzen and M. Peschar, "Relation between the pacing induced sequence of activation and left ventricular pump function in animals," *PACE - Pacing and Clinical Electrophysiology*, vol. 25, no. 4 I. pp. 484–498, 2002, doi: 10.1046/j.1460-9592.2002.00484.x.

[202] W. Huang, L. Su, S. Wu, L. Xu, and F. Xiao, "Case Report A Novel Pacing Strategy With Low and Stable Output : Pacing the Left Bundle Branch Immediately Beyond the Conduction Block," *Can. J. Cardiol.*, vol. 33, no. 12, pp. 1736.e1-1736.e3, 2017, doi: 10.1016/j.cjca.2017.09.013.

[203] M. Strik *et al.*, "Transseptal conduction as an important determinant for cardiac resynchronization therapy, as revealed by extensive electrical mapping in the dyssynchronous canine heart," *Circ. Arrhythmia Electrophysiol.*, vol. 6, no. 4, pp. 682–689, 2013, doi: 10.1161/CIRCEP.111.000028.

[204] F. Barber, I. García-Fernández, M. Lozano, and R. Sebastian, "Automatic estimation of Purkinje-Myocardial junction hot-spots from noisy endocardial samples: A simulation study," *Int. j. numer. method. biomed. eng.*, vol. 34, no. 7, pp. 1–15, 2018, doi: 10.1002/cnm.2988.

[205] H. Lee, J. H. Park, I. Seo, S. H. Park, and S. Kim, "Improved application of the electrophoretic tissue clearing technology, CLARITY, to intact solid organs including brain, pancreas, liver, kidney, lung, and intestine," *BMC Dev. Biol.*, vol. 14, no. 1, pp. 1–7, 2014, doi: 10.1186/s12861-014-0048-3.

[206] S. S. Barold, A. Ilercil, and B. Herweg, "Echocardiographic optimization of the atrioventricular and interventricular intervals during cardiac resynchronization," *Europace*, 2008, doi: 10.1093/europace/eun220.

[207] T. Guo *et al.*, "Biventricular Pacing With Ventricular Fusion by Intrinsic Activation in Cardiac Resynchronization Therapy," *Int. Heart J.*, 2015, doi: 10.1536/ihj.14-260.

[208] B. M. Van Gelder, F. A. Bracke, A. Meijer, and N. H. J. Pijls, "The hemodynamic effect of intrinsic conduction during left ventricular pacing as compared to biventricular pacing," *J. Am. Coll. Cardiol.*, 2005, doi: 10.1016/j.jacc.2005.02.098.

[209] R. Vatasescu *et al.*, "Midterm 'super-response' to cardiac resynchronization therapy by biventricular pacing with fusion: Insights from electro-anatomical mapping," *Europace*, 2009,

doi: 10.1093/europace/eup333.

[210] R. Miri, M. Reumann, D. U. J. Keller, D. Farina, and O. Dossel, "Comparison of the electrophysiologically based optimization methods with different pacing parameters in patient undergoing resynchronization treatment," in *2008 30th Annual International Conference of the IEEE Engineering in Medicine and Biology Society*, 2008, pp. 1741–1744, doi: 10.1109/IEMBS.2008.4649513.

[211] F. Ruschitzka *et al.*, "Cardiac-Resynchronization Therapy in Heart Failure with a Narrow QRS Complex," *N. Engl. J. Med.*, vol. 369, no. 15, pp. 1395–1405, 2013, doi: 10.1056/NEJMoa1306687.

[212] B. M. Van Gelder, A. Meijer, and F. A. Bracke, "Timing of the left ventricular electrogram and acute hemodynamic changes during implant of cardiac resynchronization therapy devices," *PACE - Pacing Clin. Electrophysiol.*, vol. 32, no. SUPPL. 1, 2009, doi: 10.1111/j.1540-8159.2008.02262.x.

[213] J. De Pooter *et al.*, "Different Methods to Measure QRS Duration in CRT Patients: Impact on the Predictive Value of QRS Duration Parameters," *Ann. Noninvasive Electrocardiol.*, 2016, doi: 10.1111/anec.12313.

[214] M. V. Pitzalis *et al.*, "Cardiac resynchronization therapy tailored by echocardiographic evaluation of ventricular asynchrony," *J. Am. Coll. Cardiol.*, vol. 40, no. 9, pp. 1615–1622, 2002, doi: 10.1016/S0735-1097(02)02337-9.

[215] D. Romero *et al.*, "Effects of the purkinje system and cardiac geometry on biventricular pacing: A model study," *Ann. Biomed. Eng.*, 2010, doi: 10.1007/s10439-010-9926-4.

[216] G. Tomassoni, "How to Define Cardiac Resynchronization Therapy Response," *J. Innov. Card. Rhythm Manag.*, 2016, doi: 10.19102/icrm.2016.070003.

[217] E. S. Chung *et al.*, "Results of the predictors of response to crt (prospect) trial," *Circulation*, vol. 117, no. 20, pp. 2608–2616, 2008, doi: 10.1161/CIRCULATIONAHA.107.743120.

[218] V. Gurev, J. Constantino, J. J. Rice, and N. A. Trayanova, "Distribution of electromechanical delay in the heart: Insights from a three-dimensional electromechanical model," *Biophys. J.*, 2010, doi: 10.1016/j.bpj.2010.05.028.

[219] A. W. C. Lee, C. M. Costa, M. Strocchi, C. A. Rinaldi, and S. A. Niederer, "Computational Modeling for Cardiac Resynchronization Therapy," *Journal of Cardiovascular Translational Research*, pp. 1–17, 2018.

[220] J. M. Behar *et al.*, "Optimized Left Ventricular Endocardial Stimulation Is Superior to Optimized Epicardial Stimulation in Ischemic Patients With Poor Response to Cardiac Resynchronization Therapy: A Combined Magnetic Resonance Imaging, Electroanatomic Contact Mapping, and Hemodynamic Study to Target Endocardial Lead Placement," *JACC Clin. Electrophysiol.*, 2016, doi: 10.1016/j.jacep.2016.04.006.

[221] P. Bordachar *et al.*, "Left ventricular endocardial stimulation for severe heart failure," *Journal of the American College of Cardiology*. 2010, doi: 10.1016/j.jacc.2010.04.038.

[222] F. W. Prinzen *et al.*, "Left ventricular endocardial pacing improves resynchronization therapy in canine left bundle-branch hearts," *Circ. Arrhythmia Electrophysiol.*, vol. 2, no. 5, pp. 580–587, 2009, doi: 10.1161/CIRCEP.108.846022.

[223] J. Sperzel *et al.*, "State of the art of leadless pacing," *Europace*, vol. 17, no. 10, pp. 1508–1513, 2015, doi: 10.1093/europace/euv096.

[224] J. T. Vermeulen *et al.*, "Electrophysiologic and extracellular ionic changes during acute ischemia in failing and normal rabbit myocardium," *J. Mol. Cell. Cardiol.*, vol. 28, no. 1, pp. 123–131, 1996, doi: 10.1006/jmcc.1996.0012.

[225] D. P. Zipes and H. J. J. Wellens, "Sudden Cardiac Death," *Circulation*, vol. 98, no. 21, pp. 2334–2351, 1998, doi: 10.1161/01.CIR.98.21.2334.

[226] Y. Kagiyama, J. L. Hill, and L. S. Gettes, "Interaction of Acidosis and Increased Extracellular Potassium on Action

Potential Characteristics and Conduction in Guinea Pig Ventricular Muscle," *Circ. Res.*, vol. 51, no. 5, pp. 614–623, 1982, doi: 10.1161/01.res.51.5.614.

[227] J. Senges, J. Brachmann, D. Pelzer, T. Mizutani, and W. Kübler, "Effects of some components of ischemia on electrical activity and reentry in the canine ventricular conducting system.," *Circ. Res.*, vol. 44, no. 6, pp. 864–872, Jun. 1979, doi: 10.1161/01.RES.44.6.864.

[228] B. Trénor, L. Romero, J. M. Ferrero, J. Sáiz, G. Moltó, and J. M. Alonso, "Vulnerability to reentry in a regionally ischemic tissue: A simulation study," *Ann. Biomed. Eng.*, vol. 35, no. 10, pp. 1756–1770, Oct. 2007, doi: 10.1007/s10439-007-9353-3.

[229] J. M. Ferrero, B. Trénor, F. Montilla, J. Sáiz, J. M. Alonso, and G. Moltó, "Vulnerability to reentry during the acute phase of myocardial ischemia: A simulation study," in *Computers in Cardiology*, 2003, vol. 30, pp. 425–428, doi: 10.1109/cic.2003.1291183.

[230] R. Coronel, F. J. G. Wilms-Schopman, L. R. C. Dekker, and M. J. Janse, "Heterogeneities in $[K^+]_o$ and TQ Potential and the Inducibility of Ventricular Fibrillation During Acute Regional Ischemia in the Isolated Perfused Porcine Heart," *Circulation*, vol. 92, no. 1, pp. 120–129, Jul. 1995, doi: 10.1161/01.CIR.92.1.120.

[231] J. M. Ferrero, V. Torres, F. Montilla, and E. Colomar, "Simulation of reentry during acute myocardial ischemia: role of ATP-sensitive potassium current and acidosis," in *Computers in Cardiology*, 2000, pp. 239–242, doi: 10.1109/cic.2000.898501.

[232] P. B. Tabereaux *et al.*, "Activation patterns of Purkinje fibers during long-duration ventricular fibrillation in an isolated canine heart model," *Circulation*, vol. 116, no. 10, pp. 1113–1119, Sep. 2007, doi: 10.1161/CIRCULATIONAHA.107.699264.

[233] M. J. Janse, F. J. G. Wilms-Schopman, and R. Coronel, "Ventricular Fibrillation Is Not Always Due to Multiple Wavelet Reentry," *J. Cardiovasc. Electrophysiol.*, vol. 6, no. 7, pp. 512–

521, Jul. 1995, doi: 10.1111/j.1540-8167.1995.tb00424.x.

[234] D. J. Dosdall *et al.*, "Chemical ablation of the Purkinje system causes early termination and activation rate slowing of long-duration ventricular fibrillation in dogs," *Am J Physiol Hear. Circ Physiol*, vol. 295, no. 2, pp. H883–H889, 2008, doi: 10.1152/ajpheart.00466.2008.

[235] M. Deo, P. Boyle, G. Plank, and E. Vigmond, "Arrhythmogenic mechanisms of the Purkinje system during electric shocks: A modeling study," *Hear. Rhythm*, vol. 6, no. 12, pp. 1782–1789, Dec. 2009, doi: 10.1016/j.hrthm.2009.08.023.

[236] M. E. Martinez *et al.*, "Role of the Purkinje-Muscle Junction on the Ventricular Repolarization Heterogeneity in the Healthy and Ischemic Ovine Ventricular Myocardium," *Front. Physiol.*, vol. 9, p. 718, Jun. 2018, doi: 10.3389/fphys.2018.00718.

[237] T. Lassila *et al.*, "Electrophysiology Model for a Human Heart with Ischemic Scar and Realistic Purkinje Network," in *Statistical Atlases and Computational Models of the Heart. Imaging and Modelling Challenges*, 2016, pp. 90–97, doi: 10.1007/978-3-319-28712-6_10.

[238] A. Lopez-Perez, R. Sebastian, M. Izquierdo, R. Ruiz, M. Bishop, and J. M. Ferrero, "Personalized cardiac computational models: From clinical data to simulation of infarct-related ventricular tachycardia," *Front. Physiol.*, vol. 10, p. 580, May 2019, doi: 10.3389/fphys.2019.00580.

[239] J. T. Ortiz-Pérez, J. Rodríguez, S. N. Meyers, D. C. Lee, C. Davidson, and E. Wu, "Correspondence Between the 17-Segment Model and Coronary Arterial Anatomy Using Contrast-Enhanced Cardiac Magnetic Resonance Imaging," *JACC Cardiovasc. Imaging*, vol. 1, no. 3, pp. 282–293, May 2008, doi: 10.1016/j.jcmg.2008.01.014.

[240] R. J. Kim *et al.*, "Relationship of MRI Delayed Contrast Enhancement to Irreversible Injury, Infarct Age, and Contractile Function," *Circulation*, vol. 100, no. 19, pp. 1992–2002, Nov. 1999, doi: 10.1161/01.CIR.100.19.1992.

[241] E. F. Carpio *et al.*, “Optimization of lead placement in the right ventricle during cardiac resynchronization therapy. A simulation study,” *Front. Physiol.*, vol. 10, p. 74, Feb. 2019, doi: 10.3389/fphys.2019.00074.

[242] C. Mendez, W. J. Mueller, and X. Urguiaga, “Propagation of Impulses across the Purkinje Fiber-Muscle Junctions in the Dog Heart,” *Circ. Res.*, vol. 26, no. 2, pp. 135–150, Feb. 1970, doi: 10.1161/01.RES.26.2.135.

[243] M. Gironés-Sangüesa, C. Esteban, A. González-Ascaso, J. F. Rodríguez-Matas, and J. F. Ferrero, “A Novel Model of Acute Myocardial Ischemia in Human Ventricular Cardiomyocytes,” *presented at the 47th Int. Conf. Computers in Cardiology*. Rimini, Italy, Sep. 13, 2020.

[244] A. P. Babenko, G. Gonzalez, L. Aguilar-Bryan, and J. Bryan, “Reconstituted Human Cardiac K ATP Channels,” *Circ. Res.*, vol. 83, no. 11, pp. 1132–1143, Nov. 1998, doi: 10.1161/01.RES.83.11.1132.

[245] S. Cortassa *et al.*, “A computational model integrating electrophysiology, contraction, and mitochondrial bioenergetics in the ventricular myocyte,” *Biophys. J.*, vol. 91, no. 4, pp. 1564–1589, Aug. 2006, doi: 10.1529/biophysj.105.076174.

[246] L. Murphy, D. Renodin, C. Antzelevitch, J. M. Di Diego, and J. M. Cordeiro, “Extracellular proton depression of peak and late Na^{+} current in the canine left ventricle,” *Am. J. Physiol. Circ. Physiol.*, vol. 301, no. 3, pp. H936–H944, Sep. 2011, doi: 10.1152/ajpheart.00204.2011.

[247] A. E. Doering, D. A. Eisner, and W. J. Lederer, “Cardiac Na-Ca Exchange and pH,” *Ann. N. Y. Acad. Sci.*, vol. 779, no. 1, pp. 182–198, Apr. 1996, doi: 10.1111/j.1749-6632.1996.tb44786.x.

[248] M. Egger and E. Niggli, “Paradoxical block of the Na^{+}-Ca^{2+} exchanger by extracellular protons in guinea-pig ventricular myocytes,” *J. Physiol.*, vol. 523, no. 2, pp. 353–366, Mar. 2000, doi: 10.1111/j.1469-7793.2000.t01-1-00353.x.

[249] P. Daleau, “Lysophosphatidylcholine, a metabolite which

accumulates early in myocardium during ischemia, reduces gap junctional coupling in cardiac cells," *J. Mol. Cell. Cardiol.*, vol. 31, no. 7, pp. 1391–1401, Jul. 1999, doi: 10.1006/jmcc.1999.0973.

[250] M. Gautier, H. Zhang, and I. M. Fearon, "Peroxynitrite formation mediates LPC-induced augmentation of cardiac late sodium currents," *J. Mol. Cell. Cardiol.*, vol. 44, no. 2, pp. 241–251, Feb. 2008, doi: 10.1016/j.yjmcc.2007.09.007.

[251] A. I. Undrovinas, I. A. Fleidervish, and J. C. Makielski, "Inward sodium current at resting potentials in single cardiac myocytes induced by the ischemic metabolite lysophosphatidylcholine.," *Circ. Res.*, vol. 71, no. 5, pp. 1231–1241, Nov. 1992, doi: 10.1161/01.RES.71.5.1231.

[252] K. Sakamoto, M. Ishikawa, K. Koga, T. Urushidani, and T. Nagao, "Energy Preserving Effect of l-cis Diltiazem in Isolated Ischemic and Reperfused Guinea Pig Hearts. A 31P-NMR Study.," *Jpn. J. Pharmacol.*, vol. 83, no. 3, pp. 225–232, 2000, doi: 10.1254/jjp.83.225.

[253] H. Hirche, C. Franz, L. Bös, R. Bissig, R. Lang, and M. Schramm, "Myocardial extracellular K^+ and H^+ increase and noradrenaline release as possible cause of early arrhythmias following acute coronary artery occlusion in pigs," *J. Mol. Cell. Cardiol.*, vol. 12, no. 6, pp. 579–593, Jun. 1980, doi: 10.1016/0022-2828(80)90016-4.

[254] V. Wiegand, M. Güggi, W. Meesmann, M. Kessler, and F. Greitschus, "Extracellular potassium activity changes in the canine myocardium after acute coronary occlusion and the influence of beta-blockade," *Cardiovasc. Res.*, vol. 13, no. 5, pp. 297–302, 1979, doi: 10.1093/cvr/13.5.297.

[255] R. Coronel *et al.*, "Distribution of extracellular potassium and its relation to electrophysiologic changes during acute myocardial ischemia in the isolated perfused porcine heart.," *Circulation*, vol. 77, no. 5, pp. 1125–1138, May 1988, doi: 10.1161/01.CIR.77.5.1125.

[256] L. Dux-Santoy, R. Sebastian, J. F. Rodriguez, and J. M. Ferrero, "Modeling the different sections of the cardiac conduction system to obtain realistic electrocardiograms," in *Proceedings of the Annual International Conference of the IEEE Engineering in Medicine and Biology Society, EMBS*, 2013, pp. 6846–6849, doi: 10.1109/EMBC.2013.6611130.

[257] A. L. Goldberger *et al.*, "PhysioBank, PhysioToolkit, and PhysioNet: components of a new research resource for complex physiologic signals.," *Circulation*, vol. 101, no. 23, Jun. 2000, doi: 10.1161/01.cir.101.23.e215.

[258] J. Pettersson *et al.*, "Spatial, individual, and temporal variation of the high-frequency QRS amplitudes in the 12 standard electrocardiographic leads," *Am. Heart J.*, vol. 139, no. 2, pp. 352–358, Feb. 2000, doi: 10.1016/S0002-8703(00)90246-1.

[259] E. B. Sgarbossa *et al.*, "Electrocardiographic Diagnosis of Evolving Acute Myocardial Infarction in the Presence of Left Bundle-Branch Block," *N. Engl. J. Med.*, vol. 334, no. 8, pp. 481–487, Feb. 1996, doi: 10.1056/NEJM199602223340801.

[260] S. W. Smith, K. W. Dodd, T. D. Henry, D. M. Dvorak, and L. A. Pearce, "Diagnosis of ST-elevation myocardial infarction in the presence of left bundle branch block with the ST-elevation to S-wave ratio in a modified sgarbossa rule," *Ann. Emerg. Med.*, vol. 60, no. 6, pp. 766–776, Dec. 2012, doi: 10.1016/j.annemergmed.2012.07.119.

[261] R. D. Walton *et al.*, "Influence of the Purkinje-muscle junction on transmural repolarization heterogeneity," *Cardiovasc. Res.*, vol. 103, no. 4, pp. 629–640, 2014, doi: 10.1093/cvr/cvu165.

[262] R. D. Walton, A. P. Benson, M. E. L. Hardy, E. White, and O. Bernus, "Electrophysiological and structural determinants of electrotonic modulation of repolarization by the activation sequence," *Front. Physiol.*, vol. 4, p. 281, Oct. 2013, doi: 10.3389/fphys.2013.00281.

[263] F. L. Burton and S. M. Cobbe, "Dispersion of ventricular repolarization and refractory period," *Cardiovascular Research*,

vol. 50, no. 1. Oxford Academic, pp. 10–23, Apr. 01, 2001, doi: 10.1016/S0008-6363(01)00197-3.

[264] A. G. Kléber, M. J. Janse, F. J. van Capelle, and D. Durrer, "Mechanism and time course of S-T and T-Q segment changes during acute regional myocardial ischemia in the pig heart determined by extracellular and intracellular recordings.," *Circ. Res.*, vol. 42, no. 5, pp. 603–613, May 1978, doi: 10.1161/01.RES.42.5.603.

[265] C. Costeas, N. S. Peters, B. Waldecker, E. J. Ciaccio, A. L. Wit, and J. Coromilas, "Mechanisms Causing Sustained Ventricular Tachycardia With Multiple QRS Morphologies," *Circulation*, vol. 96, no. 10, pp. 3721–3731, Nov. 1997, doi: 10.1161/01.CIR.96.10.3721.

[266] M. J. Janse *et al.*, "The 'border zone' in myocardial ischemia. An electrophysiological, metabolic, and histochemical correlation in the pig heart.," *Circ. Res.*, vol. 44, no. 4, pp. 576–588, Apr. 1979, doi: 10.1161/01.RES.44.4.576.

[267] A. G. Kléber, "Extracellular potassium accumulation in acute myocardial ischemia," *Journal of Molecular and Cellular Cardiology*, vol. 16, no. 5. Elsevier, pp. 389–394, May 01, 1984, doi: 10.1016/S0022-2828(84)80610-0.

[268] B. A. J. Lawson, R. S. Oliveira, L. A. Berg, P. A. A. Silva, K. Burrage, and R. W. dos Santos, "Variability in electrophysiological properties and conducting obstacles controls re-entry risk in heterogeneous ischaemic tissue," *Philos. Trans. R. Soc. A Math. Phys. Eng. Sci.*, vol. 378, no. 2173, p. 20190341, 2020, doi: 10.1098/rsta.2019.0341.

[269] A. A. M. Wilde, "Role of ATP-sensitive K^+ channel current in ischemic arrhythmias," *Cardiovasc. Drugs Ther.*, vol. 7, no. 3 Supplement, pp. 521–526, 1993, doi: 10.1007/BF00877617.

[270] M. Said *et al.*, "Increased intracellular Ca^{2+} and SR Ca^{2+} load contribute to arrhythmias after acidosis in rat heart. Role of Ca^{2+}/calmodulin-dependent protein kinase II," *Am. J. Physiol. Circ. Physiol.*, vol. 295, no. 4, pp. H1669–H1683, 2008, doi:

10.1152/ajpheart.00010.2008.

[271] E. Behradfar, A. Nygren, and E. J. Vigmond, "The Role of Purkinje-Myocardial Coupling during Ventricular Arrhythmia: A Modeling Study," *PLoS One*, vol. 9, no. 2, p. e88000, Feb. 2014, doi: 10.1371/journal.pone.0088000.

[272] P. L. Friedman, J. R. Stewart, J. J. Fenoglio, and A. L. Wit, "Survival of Subendocardial Purkinje Fibers after Extensive Myocardial Infarction in Dogs," *Circ. Res.*, vol. 33, no. 5, pp. 597–611, Nov. 1973, doi: 10.1161/01.RES.33.5.597.

[273] P. F. Cranefield, H. O. Klein, and B. F. Hoffman, "Conduction of the cardiac impulse. 1. Delay, block, and one-way block in depressed Purkinje fibers," *Circ. Res.*, vol. 28, no. 2, pp. 199–219, Feb. 1971, doi: 10.1161/01.RES.28.2.199.

[274] A. L. Wit, B. F. Hoffman, and P. F. Cranefield, "Slow Conduction and Reentry in the Ventricular Conducting System," *Circ. Res.*, vol. 30, no. 1, pp. 1–10, Jan. 1972, doi: 10.1161/01.RES.30.1.1.

[275] W. J. Penny and D. J. Sheridan, "Arrhythmias and cellular electrophysiological changes during myocardial 'ischaemia' and reperfusion," *Cardiovascular Research*, vol. 17, no. 6. Oxford University Press, pp. 363–372, 1983, doi: 10.1093/cvr/17.6.363.

[276] K. D. Chadda, V. S. Banka, and R. H. Helfant, "Rate Dependent Ventricular Ectopia Following Acute Coronary Occlusion," *Circulation*, vol. 49, no. 4, pp. 654–658, Apr. 1974, doi: 10.1161/01.CIR.49.4.654.

[277] R. J. Sung, W. A. Shapiro, E. N. Shen, F. Morady, and J. Davis, "Effects of verapamil on ventricular tachycardias possibly caused by reentry, automaticity, and triggered activity," *J. Clin. Invest.*, vol. 72, no. 1, pp. 350–360, 1983, doi: 10.1172/JCI110975.

[278] K. I. Lie, J. J. Wellens, E. Downar, and D. Durrer, "Observations on Patients with Primary Ventricular Fibrillation Complicating Acute Myocardial Infarction," *Circulation*, vol. 52, no. 5, pp. 755–759, 1975, doi: 10.1161/01.cir.52.5.755.

[279] R. F. Gilmour and D. P. Zipes, “Different electrophysiological responses of canine endocardium and epicardium to combined hyperkalemia, hypoxia, and acidosis.,” *Circ. Res.*, vol. 46, no. 6, pp. 814–825, 1980, doi: 10.1161/01.RES.46.6.814.

[280] R. Lazzara, N. El-Sherif, and B. J. Scherlag, “Early and Late Effects of Coronary Artery Occlusion on Canine Purkinje Fibers,” *Circ. Res.*, vol. 35, no. 3, pp. 391–399, Sep. 1974, doi: 10.1161/01.RES.35.3.391.

[281] J. De Pooter *et al.*, “Biventricular Paced QRS Area Predicts Acute Hemodynamic CRT Response Better Than QRS Duration or QRS Amplitudes,” *J. Cardiovasc. Electrophysiol.*, 2017, doi: 10.1111/jce.13132.

[282] C. Daubert, N. Behar, R. P. Martins, P. Mabo, and C. Leclercq, “Avoiding non-responders to cardiac resynchronization therapy: A practical guide,” *European Heart Journal*, vol. 38, no. 19. Oxford University Press, pp. 1463–1472, May 14, 2017, doi: 10.1093/eurheartj/ehw270.

[283] O. R. Segal, A. W. C. Chow, N. S. Peters, and D. W. Davies, “Mechanisms that initiate ventricular tachycardia in the infarcted human heart,” *Hear. Rhythm*, vol. 7, no. 1, pp. 57–64, Jan. 2010, doi: 10.1016/j.hrthm.2009.09.025.

[284] H. Zhang, Z. xi Zhang, L. Yang, Y. bin Jin, and Y. zhuo Huang, “Mechanisms of the acute ischemia-induced arrhythmogenesis - A simulation study,” *Math. Biosci.*, vol. 203, no. 1, pp. 1–18, Sep. 2006, doi: 10.1016/j.mbs.2006.06.003.

[285] C. Trovato *et al.*, “Human Purkinje in silico model enables mechanistic investigations into automaticity and pro-arrhythmic abnormalities,” *J. Mol. Cell. Cardiol.*, vol. 142, pp. 24–38, May 2020, doi: 10.1016/j.yjmcc.2020.04.001.

[286] H. Si and K. Gärtner, “Meshing Piecewise Linear Complexes by Constrained Delaunay Tetrahedralizations,” in *Proceedings of the 14th International Meshing Roundtable*, 2005, pp. 147–163.

[287] C. P. Bradley, A. J. Pullan, and P. J. Hunter, “Effects of Material Properties and Geometry on Electrocardiographic Forward

Simulations," *Ann. Biomed. Eng.*, vol. 28, no. 7, pp. 721–741, Jul. 2000, doi: 10.1114/1.1289467.

[288] S. L. Bressler and M. Ding, "Event-Related Potentials," in *Wiley Encyclopedia of Biomedical Engineering*, American Cancer Society, 2006.

[289] S. Gabriel, R. W. Lau, and C. Gabriel, "The dielectric properties of biological tissues: II. Measurements in the frequency range 10 Hz to 20 GHz," *Phys. Med. Biol.*, vol. 41, no. 11, pp. 2251–2269, Nov. 1996, doi: 10.1088/0031-9155/41/11/002.

[290] R. N. Klepfer, C. R. Johnson, and R. S. Macleod, "The effects of inhomogeneities and anisotropies on electrocardiographic fields: a 3-D finite-element study," *IEEE Trans. Biomed. Eng.*, vol. 44, no. 8, pp. 706–719, 1997, doi: 10.1109/10.605427.

[291] P. A. Tun and M. E. Lachman, "The association between computer use and cognition across adulthood: Use it so you won't lose it?," *Psychol. Aging*, vol. 25, no. 3, pp. 560–568, 2010, doi: 10.1037/a0019543.

[292] B. J. Roth, "The electrical potential produced by a strand of cardiac muscle: A bidomain analysis," *Ann. Biomed. Eng.*, vol. 16, no. 6, pp. 609–637, Nov. 1988, doi: 10.1007/BF02368018.

[293] D. B. Geselowitz and W. T. Miller, "A bidomain model for anisotropic cardiac muscle," *Ann. Biomed. Eng.*, vol. 11, no. 3–4, pp. 191–206, May 1983, doi: 10.1007/BF02363286.